

Chiral variant and invariant components
of the nucleon mass
with quark-hadron crossover in neutron stars

(中性子星におけるクォーク・ハドロン・クロスオーバーと、
核子質量のカイラル依存・非依存成分)

Takuya Minamikawa

February 25, 2023

Abstract

Recently, several researches indicate that the nucleon mass consists of two components: the chiral “variant” condensate and the chiral “invariant” mass. We build an equation of state (EOS) for neutron stars by interpolating hadronic EOS at low density and quark EOS at high density, and research the two components using the observational data of neutron stars.

Crossover from hadronic matter to quark matter in the color-flavor locked phase is assumed. The parity doublet model (PDM) is used for hadronic matter, and Nambu–Jona-Lasinio (NJL) type model as a quark effective model is used for quark matter. The mass of nucleons based on the parity doublet structure has two components: the one associated with the spontaneous breaking for the chiral symmetry, and a chiral invariant component m_0 . The behavior of the nuclear EOSs at low density is affected by the value of the chiral invariant mass m_0 , and the neutron star radius has strong correlations with them. Using the radius constraint by LIGO-Virgo and NICER, we obtain that the large value of the chiral invariant mass m_0 is favored, as $600 \text{ MeV} \lesssim m_0 \lesssim 900 \text{ MeV}$. This is based on our paper [1].

The chiral condensates in crossover domain is also investigated. Using the condensates at the boundaries, the corresponding condensates in the interpolated domain can be calculated numerically. Using the causality and the constraints obtained from the observational data of neutron stars, the chiral condensates in the crossover domain connects smoothly the ones calculated from the PDM and NJL. We emphasize that our method can be applied to other various quantities: strange quark condensate, diquark condensates, and the particle number fractions. This is based on our paper [2].

Contents

1	Introduction	3
1.1	Mass and chiral symmetry in QCD	5
1.2	Effective models for nucleon mass	8
1.2.1	Nambu–Jona-Lasinio (NJL) model	8
1.2.2	Linear sigma model (LSM)	9
1.3	Chiral invariant component of nucleon mass	11
1.4	Nuclear matter and the saturation properties	15
1.5	M - R relation for neutron stars	18
1.6	Quark-hadron crossover in neutron star	20
2	Chiral Invariant Mass and Neutron Stars	22
2.1	Nuclear matter	22
2.1.1	Parity doublet model	22
2.1.2	Model parameters	27
2.2	Unified EOS with CFL phase	28
2.2.1	NJL-type model for quark matter	28
2.2.2	Interpolating EOSs	31
2.3	Numerical results	34
2.4	Summary and discussions of Ch.2	38
3	Chiral Condensate in Crossover	41
3.1	Nuclear matter	41
3.1.1	Chiral condensate in the PDM	41
3.1.2	Chiral scalar density in a nucleon	42
3.1.3	Dilute regime	44
3.1.4	Strange quark condensate	45
3.2	Quark matter (CFL phase)	47
3.2.1	Overall picture	47

3.2.2	Chiral condensates in the CFL quark matter	48
3.3	Condensates in a unified EOS	49
3.3.1	Unified generating functional	50
3.3.2	A practical method to compute condensates	51
3.3.3	Numerical results	51
3.4	Discussions	59
3.4.1	Casher's argument and the chiral scalar density in nucleons	59
3.4.2	Topology of pion clouds and spatial modulations of the chiral scalar density	60
3.4.3	Diquarks	63
3.5	Summary of Ch.3	64
4	Conclusion	66
A	Chiral condensate and pion-nucleon sigma-term in hadron effective models	68
A.1	Some definitions	68
A.2	Linear density approximation (LDA) for chiral condensate . .	69
A.3	Chiral condensate in the PDM	70
A.4	Tilte of the chiral condensate in the PDM	71
A.5	Relation between a scalar meson and a scalar density and es- timation of the value of sigma-term in vacuum	73
A.6	Sigma-term from the nucleon mass	75
A.7	Sigma-term from the energy density per nucleon	76
A.8	Comparison	77
B	Calculation of $\partial a_n/\partial J$ in Eq.(3.20)	79
C	Hellmann–Feynman Theorem	82
C.1	Perturbation of Hamiltonian	82
C.2	Pseudoinverse	83

Chapter 1

Introduction

Understanding of the origin of the nucleon mass is one of the main purposes in this thesis. Especially, we focus on the chiral “variant” and “invariant” components of the nucleon mass, as explained below.

The nucleon consists of three valence quarks, and the quarks are described by quantum chromodynamics (QCD). Unfortunately, QCD is essentially difficult to be solved, due to its non-perturbative properties in low energy region. Intuitively, hadrons can be said to have a very complicated internal structure, in which quark-antiquark annihilations and creations occur many times, and many gluons propagate among quarks, antiquarks, and gluons themselves.

One of the traditional ways to study the nucleon mass is based on the chiral symmetry. The chiral symmetry is an approximate symmetry in QCD that appears when quark masses are neglected. It is well known that the chiral symmetry is broken spontaneously in vacuum, or also in the typical energy scale around our lives. In 1961, the Nambu–Jona-Lasinio model (NJL model) for baryons was originally introduced to study the origin of hadron masses with the spontaneous symmetry breaking of chiral symmetry [3, 4]. In the original NJL model, the order parameter of the spontaneous chiral symmetry breaking is the chiral condensate $\langle \bar{\psi}\psi \rangle$, which is the expectation value of the scalar quantity of a baryon field ψ . The chiral condensate has a nonzero value in vacuum, while vanishes in the chiral restored phase. As explained later (Sec.1.2), the nucleon mass term breaks the chiral symmetry, and the chiral condensate becomes the nucleon mass in this model. Intuitively, NJL model provides the picture that a baryon obtains its mass to dress the energy from pairs of fermion-antifermion, which is inspired by the Bardeen–Cooper–Schrieffer (BCS) theory for superconductivity.

The sigma model is also broadly used to study the spontaneous symmetry breaking. Especially, the linear sigma model (LSM) is used as an effective model for scalar and pseudoscalar mesons. In the LSM, the order parameter of the spontaneous chiral symmetry breaking is the expectation value of the scalar field, $\langle\sigma\rangle$, which are also called chiral condensate. As also explained later (Sec.1.2), in the traditional hadronic model with the LSM, the nucleon mass m_N is considered to be made of mainly chiral condensate, as well as the NJL model. Therefore, the mass also vanishes in the restored phase, $m_N \propto \langle\sigma\rangle \rightarrow 0$.

However, there may exist not only such a chiral “variant” component of the nucleon mass, but also chiral “invariant” component. If so, the nucleon mass may keep a finite value, $m_N \rightarrow m_0 \neq 0$, even if the quark masses are neglected. Briefly, the effective contribution of the chiral invariant component appears as a mixing coupling with “parity doubling” structure, and nucleon and its parity doubling partner are degenerate in the chiral restored phase. In 1989, the main idea of the parity doubling structure was proposed [5], and from then, there are some lattice QCD simulations which support the parity doubling structures and the existence of chiral invariant masses [6–10]. In around 2000–2010, the vacuum properties of the parity doubling structure for nucleons was studied [11–16].

Since the chiral symmetry is expected to be restored at high temperature and/or high density, the hadron properties will change in such extreme environment. Therefore, the structure of the hadron mass, which includes the chiral condensate and the chiral invariant mass, can affect the physics at high temperature and/or high density. We focus on neutron stars as the extreme compact object, where the observational technology has advanced in the last decade, 2010s.

In 2010, a heavier neutron star with around two times of the solar mass, $\sim 2M_\odot$, was observed [17], and this observational data excluded a lot of hadronic models. Moreover, in the late 2010s, the observational technology for gravitational wave was developed and the first gravitational wave data for neutron stars (GW170817) was observed in 2017 [18–20]. The observation through gravitational wave teaches us not only the mass of a compact star but also its radius. These progress of technology rather encourages the interactions between nuclear physics and astrophysics. Because, if the mass and the radius of a neutron star are around the solar mass $M_\odot \sim 2 \times 10^{30}$ kg and 10 km, its average density is around $\sim 10^{17}$ kg/m³, which is comparable to the normal nuclear density. Moreover, it is known that a relation between the

masses and the radii of neutron stars has one-to-one correspondence with an equation of state (EOS) of matter, which means that the observational data teaches us the EOS, which includes the microscopic physics. Recently, some millisecond pulsars were detected by NASA [21–24]. The more observational data of neutron stars can be obtained in the future.

Today, there are a lot of works to study the nuclear matter or the neutron star matter using hadronic models based on the parity doubling structure (e.g. Refs. [25–57]). Some works extrapolate the hadronic EOS to higher density $n_B \gtrsim 3n_0$, but it is questionable whether the pure hadronic picture is valid at $n_B \gtrsim 2n_0$ [58–61]. While, according to QCD, the color-superconducting matter is expected to appear with high density limit. Moreover, it is known that the crossover from the hadronic phase to the quark phase is favored by the neutron star observational data. In Refs. [50, 52], they construct an effective model combining a PDM and an NJL-type model with two flavors assuming no color-superconductivity.

Lastly, we summarize the introduction. One of the main targets is quark condensate, which can be said that the chiral “variant” component of the nucleon mass. Another one is the chiral invariant component of the nucleon mass. The rest of the sections 1.1-1.6 in this chapter, we will explain in more detail the physics treated in this thesis. In Ch. 2, we construct an unified EOS assuming crossover from the hadronic phase, which is described by a PDM, to the color-superconducted quark phase. Comparing the masses and the radii of neutron stars, which are calculated from the unified EOS, and the observational data of neutron stars, we obtain the possible values of the chiral invariant mass. In Ch. 3, we develop how to calculate the chiral condensate from the unified EOS, and we discuss the inhomogeneous picture of the chiral condensate.

1.1 Mass and chiral symmetry in QCD

QCD is the theory for quarks and gluons. Quarks $q_{f,c}$ have two types of quantum numbers: N_f flavors with $SU(N_f)_f$, and $N_c = 3$ colors with $SU(3)_c$. Gluons are represented as the gauge fields A_a^μ of $SU(3)_c$. In this thesis, $N_f = 2$ or 3 is mainly used.

The QCD Lagrangian is

$$\begin{aligned}\mathcal{L}_{\text{QCD}} &= \sum_{f=1}^{N_f} \sum_{c=1}^3 \bar{q}_{f,c} (i\gamma^\mu D_\mu - m_f) q_{f,c} - \sum_{a=1}^8 \frac{1}{4} G_a^{\mu\nu} G_{\mu\nu}^a \\ &= \bar{q} (i\gamma^\mu D_\mu - \hat{m}) q - \frac{1}{2} \text{tr} G^{\mu\nu} G_{\mu\nu},\end{aligned}\tag{1.1}$$

where $q = (q_{f,c})$ is a quark field, $D_\mu = \partial_\mu - igA_\mu$ is the covariant derivative for quarks, $A_\mu = T_a A_\mu^a$ is a gluon field, $G_{\mu\nu} = T_a G_{\mu\nu}^a$ is the field strength of gluons, and $\hat{m} = \text{diag}(m_f)$ is the diagonal matrix of the current quark masses. When $\hat{m} = 0$, QCD possesses the chiral $\text{SU}(N_f)_L \times \text{SU}(N_f)_R$ symmetry, which is a combination of the flavor symmetry for the left-handed quarks q_L and that for the right-handed quarks q_R ,

$$q_L = P_L q = \frac{1 - \gamma_5}{2} q, \quad q_R = P_R q = \frac{1 + \gamma_5}{2} q.\tag{1.2}$$

This symmetry structure is easily seen by decomposing the Lagrangian with respect to the left- and right-handed quark fields as

$$\bar{q}_L i\gamma^\mu D_\mu q_L + \bar{q}_R i\gamma^\mu D_\mu q_R - (\bar{q}_L \hat{m} q_R + \bar{q}_R \hat{m} q_L).\tag{1.3}$$

We can easily see that the kinetic term for left- and right-handed quarks are separated, while the mass term mixes left- and right-handed quarks. Although the chiral symmetry is not exact due to the current quark masses, it can be said that QCD has an approximate chiral symmetry when $m_f/\Lambda_{\text{QCD}} \ll 1$. Because the characteristic energy scale of QCD, called the QCD scale Λ_{QCD} , is around 300 MeV, and the current quark masses have the values of $m_u \approx m_d \lesssim 5$ MeV and $m_s \lesssim 100$ MeV, the approximate chiral symmetry is valid for the up, down, and strange quarks.

The spontaneously breaking of the chiral symmetry is one of well known features in low-energy QCD. As explained below, the chiral symmetry is broken spontaneously to the flavor symmetry as

$$\text{SU}(N_f)_L \times \text{SU}(N_f)_R \xrightarrow{\text{SSB}} \text{SU}(N_f)_f\tag{1.4}$$

at low temperature and low density (See also Fig.1.1). Here, let the vacuum $|0\rangle$ be in trivial phase with the chiral limit $m_f = 0$. The trivial vacuum is defined as $Q_L^a |0\rangle = Q_R^a |0\rangle = 0$ with the generators for chiral symmetry Q_L

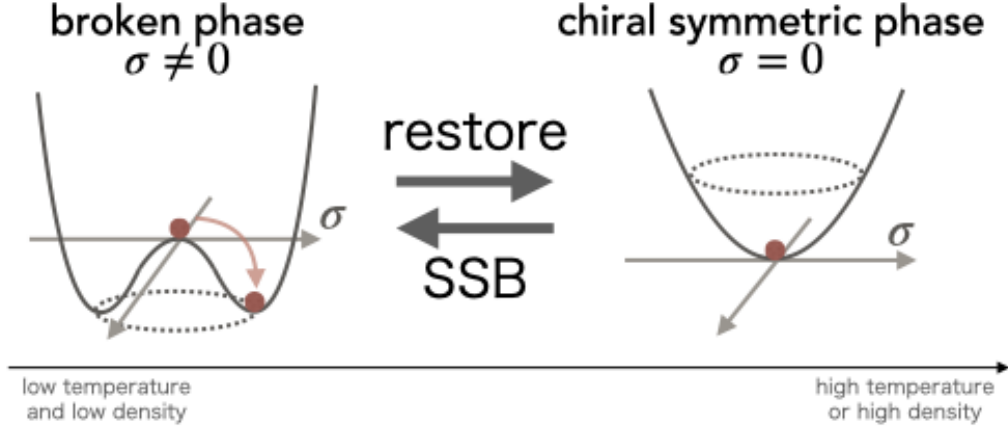


Figure 1.1: Schematic picture of the spontaneous symmetry breaking of the chiral symmetry, with a wine-bottle potential.

and Q_R (also called chiral charges). In other words, the trivial vacuum is not changed by the chiral transformation

$$e^{iQ_{L,R}} |0\rangle = |0\rangle . \quad (1.5)$$

This implies that, as well as the Lagrangian, the trivial vacuum is invariant under the chiral transformation. These generators obey the following commutation relation

$$[Q_L^a, Q_L^b] = i\varepsilon_{abc}Q_L^c, \quad [Q_R^a, Q_R^b] = i\varepsilon_{abc}Q_R^c, \quad [Q_L^a, Q_R^b] = 0 \quad (1.6)$$

or

$$[Q_V^a, Q_V^b] = i\varepsilon_{abc}Q_V^c, \quad [Q_A^a, Q_A^b] = i\varepsilon_{abc}Q_V^c, \quad [Q_V^a, Q_A^b] = i\varepsilon_{abc}Q_A^c \quad (1.7)$$

where $Q_V := Q_R + Q_L$, $Q_A := Q_R - Q_L$. Therefore, there is a subgroup of chiral symmetry with the generator Q_V , which is just the flavor $SU(N_f)_f$ symmetry. In the symmetry broken phase with the vacuum $|\Omega\rangle$, the chiral charges are not well-defined, due to the existence of the singularity associated with the massless Nambu–Goldstone (NG) boson. Still, we conventionally write

$$“Q_{L,R} |\Omega\rangle” \neq 0 \quad \text{or}, \quad “e^{iQ_{L,R}} |\Omega\rangle” \neq |\Omega\rangle , \quad (1.8)$$

where the quotation mark means that Eq.(1.8) has no meaning literally, but it can be said that the vacuum may be changed to a different vacuum by chiral transformation. This is corresponding to the picture of the wine bottle potential for chiral symmetry.

According to the Nambu–Goldstone theorem, when symmetry breaks spontaneously, massless modes appear, which is called Nambu–Goldstone bosons (NG bosons). In the case of the chiral symmetry, the spontaneous chiral symmetry breaking is triggered by the chiral condensate, $\langle \bar{q}q \rangle$, and the NG bosons are called pions (in two-flavor case). Traditionally, the nucleon mass were considered to be composed of mainly the chiral condensate, such as the traditional effective models which are explained in Sec.1.2. While, another contribution to the masses is implied as explained in Sec.1.3.

1.2 Effective models for nucleon mass

In this section, we explain some effective models to be used to study the spontaneous symmetry breaking.

1.2.1 Nambu–Jona-Lasinio (NJL) model

In the original paper by Nambu and Jona-Lasinio [3,4], a model was proposed to produce the mass of nucleon by dynamically generating the spontaneous chiral symmetry breaking. The model is modified to a model for effective quarks which obtain masses by the spontaneous chiral symmetry breaking (see e.g. Ref. [62] for a review). Here we briefly review a simplest model among several extended models.

Lagrangian of the NJL is

$$\mathcal{L}_{\text{NJL}} = \bar{\psi}i\gamma^\mu\partial_\mu\psi + g[(\bar{\psi}\psi)^2 + (\bar{\psi}i\gamma_5\psi)^2], \quad (1.9)$$

where ψ is a fermion field, which was originally assigned a baryon [3,4]. The NJL Lagrangian \mathcal{L}_{NJL} is invariant under the chiral transformation,

$$\psi \rightarrow e^{-i\theta\gamma_5}\psi = (\cos\theta - i\gamma_5\sin\theta)\psi, \quad (1.10)$$

and then,

$$\begin{aligned} \bar{\psi}\psi &\rightarrow \bar{\psi}\psi \cos 2\theta - \bar{\psi}i\gamma_5\psi \sin 2\theta, \\ \bar{\psi}i\gamma_5\psi &\rightarrow \bar{\psi}\psi \sin 2\theta + \bar{\psi}i\gamma_5\psi \cos 2\theta. \end{aligned} \quad (1.11)$$

The expectation value of the scalar quantity $\langle \bar{\psi}\psi \rangle$ is the chiral condensate, and in the NJL model, the spontaneous chiral symmetry breaking is triggered by the chiral condensate. Note that, because the coupling constant g is mass dimension of -2 , the NJL model is not renormalizable. Therefore, for a cutoff parameter, Λ , the NJL model can be adopted only up to momentum $p < \Lambda$.

In these days, NJL model is broadly used as the effective model for effective quarks, denoted q instead of ψ . Taking mean field approximation as

$$(\bar{q}q)^2 \xrightarrow{\text{MFA}} 2g \langle \bar{q}q \rangle \bar{q}q - g \langle \bar{q}q \rangle^2, \quad (1.12)$$

$$(\bar{q}i\gamma_5 q)^2 \xrightarrow{\text{MFA}} 2g \langle \bar{q}i\gamma_5 q \rangle \bar{q}i\gamma_5 q - g \langle \bar{q}i\gamma_5 q \rangle^2, \quad (1.13)$$

the Lagrangian \mathcal{L}_{NJL} is rewritten as

$$\mathcal{L}_{\text{NJL}}^{\text{MFA}} = \bar{q}[i\gamma^\mu \partial_\mu - G(\sigma + i\gamma_5\pi)]q - \frac{\mu^2}{2}(\sigma^2 + \pi^2), \quad (1.14)$$

where $-G\sigma = 2g \langle \bar{q}q \rangle$, $-G\pi = 2g \langle \bar{q}i\gamma_5 q \rangle$, and $\mu^2 = G^2/2g$. $\langle \bar{q}q \rangle$ is the chiral condensate, which is also called the quark condensate, and σ and π are corresponding to the vacuum expectation values of a scalar meson and a pseudoscalar meson (pion). Assuming the vacuum is parity symmetric, $\pi = 0$, the gap equation for σ is given as

$$M = \frac{3gM}{\pi^2} \left(-M^2 \ln \frac{\sqrt{\Lambda^2 + M^2} + \Lambda}{M} + \Lambda \sqrt{\Lambda^2 + M^2} \right) \quad (1.15)$$

where $M = G\sigma = -2g \langle \bar{q}q \rangle$ is the effective quark mass. This has only a trivial solution $M = 0$ for $g \leq g_c = \pi^2/3\Lambda^2$. For a large coupling $g > g_c$, on the other hand, there exists a nontrivial solution, $M \neq 0$, which implies the spontaneous chiral symmetry breaking.

1.2.2 Linear sigma model (LSM)

Next, we explain the LSM. The Lagrangian is given by

$$\mathcal{L}_{\text{LSM}} = \frac{1}{2}(\partial_\mu \sigma)^2 + \frac{1}{2}(\partial_\mu \pi)^2 - V_{\text{tot}}(\sigma, \pi), \quad (1.16)$$

$$V_{\text{tot}}(\sigma, \pi) = V(\sigma^2 + \pi^2) - \epsilon m_q \sigma, \quad (1.17)$$

where σ is a scalar meson, π is a pseudoscalar meson (pion), and $V(x)$ is an arbitrary function. We note that we added a term proportional to the current quark mass m_q , which explicitly breaks the chiral symmetry, to reproduce the pion mass. The meson fields σ and π are transformed as the same way of $\bar{\psi}\psi$ and $\bar{\psi}i\gamma_5\psi$ respectively, as

$$\begin{aligned}\sigma &\rightarrow \sigma \cos 2\theta - \pi \sin 2\theta, \\ \pi &\rightarrow \sigma \sin 2\theta + \pi \cos 2\theta.\end{aligned}\tag{1.18}$$

Because the transformation Eq.(1.18) is linear with respect to σ and π , the model is called “linear” sigma model. When the potential is the shape of a wine bottle, such as $V(x^2) = -ax^2 + bx^4$ with positive couplings a and b , the values of $\langle\sigma\rangle$ and $\langle\pi\rangle$ have arbitrary values satisfying $\langle\sigma\rangle^2 + \langle\pi\rangle^2 = \text{const.}$ Because of the explicit symmetry breaking term $\epsilon m_q \sigma$, the expectation values are determined as $\langle\sigma\rangle > 0$ and $\langle\pi\rangle = 0$. Here, the value of $\langle\sigma\rangle$ is equal to f_π , which is the pion decay constant.

Taking mean field approximation, the kinetic terms are dropped and the equation of motion for σ in vacuum is

$$0 = \frac{\partial V_{\text{tot}}}{\partial \sigma}(f_\pi, 0) = 2f_\pi V'(f_\pi^2) - \epsilon m_q.\tag{1.19}$$

The pion mass is determined as the curvature of the potential, and then the pion mass in vacuum is related to the current quark mass through the explicit symmetry breaking term,

$$m_\pi^2 = \frac{\partial^2 V_{\text{tot}}}{\partial \pi^2}(f_\pi, 0) = \epsilon m_q / f_\pi.\tag{1.20}$$

While, the quark condensate can be calculated assuming the partition functions for quarks and for hadrons are equivalent $Z_{\text{QCD}} = Z_{\text{LSM}} = \exp V_{\text{tot}}$,

$$\langle\bar{q}q\rangle = \frac{\partial}{\partial m_q} \ln Z_{\text{QCD}} = \frac{\partial}{\partial m_q} V_{\text{tot}} = -\epsilon \langle\sigma\rangle\tag{1.21}$$

Using Eqs.(1.20) and (1.21), one obtain the following relation,

$$m_\pi^2 f_\pi \langle\sigma\rangle = -m_q \langle\bar{q}q\rangle,\tag{1.22}$$

which is closely related to Gell-Mann–Oakes–Renner relation.

To study interactions between baryons and mesons, LSM with Yukawa couplings is also broadly used, such as

$$\mathcal{L}'_{\text{LSM}} = \bar{\psi}[i\gamma^\mu\partial_\mu - G(\sigma + i\gamma_5\pi)]\psi + \frac{1}{2}(\partial_\mu\sigma)^2 + \frac{1}{2}(\partial_\mu\pi)^2 - V_{\text{tot}}(\sigma, \pi). \quad (1.23)$$

The LSM Lagrangian with baryon fields $\mathcal{L}'_{\text{LSM}}$ is corresponding to the NJL model with mean field approximation Eq.(1.14). If $\epsilon = 0$ and $V(x^2) = -ax^2 + bx^4$, the Lagrangian Eq.(1.23) is renormalizable, because the couplings G and b are dimensionless and a is dimension 2.

The mass term of the baryon is forbidden by the chiral symmetry. In the LSM, the baryon mass consists of only the chiral condensate $\langle\sigma\rangle$. Therefore, the baryon mass should vanish in the chiral restored phase. The LSM can explain the low-energy nuclear physics, but it is not established that the LSM can be extrapolated to high-energy region.

1.3 Chiral invariant component of nucleon mass

Chiral condensate $\langle\bar{q}q\rangle$ is one of important ingredients to explain the origin of hadron masses in the low energy hadron physics. Chiral condensate can be said as a chiral variant component of the masses. Besides, the existence of the chiral invariant component of the masses is implied. One of the candidates of the origin of such component is gluon or its bound state, glueball, because gluon is independent of chiral symmetry for quarks. However, the origin of the chiral invariant components of hadron masses is not yet clarified.

In 1989, a parity doubling structure for nucleons was proposed in a framework of an effective hadronic model, and the effective contribution of the chiral invariant mass was introduced as the mixing term between the parity doubling partners [5]. The models including the parity doubling structure are generally called parity doublet models (PDM). Some lattice QCD simulations support the parity doubling structures and the existence of chiral invariant masses [6–10].

Let us briefly see a typical example of parity doubling structure. In a PDM, two fields ψ and ψ^{mir} are introduced for the ground-state nucleon $N(939)$ and the negative-parity excited-state nucleon $N^*(1535)$. The parity partner field ψ^{mir} has negative parity, and the opposite chiral representation

for ψ , which means that the following transformations are satisfied:

$$\begin{aligned} \psi_{L,R} &\xrightarrow{\text{parity}} +\psi_{R,L}, & \psi_L &\xrightarrow{\text{chiral}} g_L \psi_L, & \psi_R &\xrightarrow{\text{chiral}} g_R \psi_R, \\ \psi_{L,R}^{\text{mir}} &\xrightarrow{\text{parity}} -\psi_{R,L}^{\text{mir}}, & \psi_L^{\text{mir}} &\xrightarrow{\text{chiral}} g_R \psi_L^{\text{mir}}, & \psi_R^{\text{mir}} &\xrightarrow{\text{chiral}} g_L \psi_R^{\text{mir}}, \end{aligned} \quad (1.24)$$

where $g_L \in \text{SU}(2)_L$ and $g_R \in \text{SU}(2)_R$. Such representation like ψ^{mir} is called the ‘‘mirror representation’’. Although the fermion mass term of $\bar{\psi}_L \psi_R + \bar{\psi}_R \psi_L$ is not chiral invariant, there is the chiral invariant mixing term

$$m_0(\bar{\psi}_L \psi_R^{\text{mir}} + \bar{\psi}_R^{\text{mir}} \psi_L - \bar{\psi}_R \psi_L^{\text{mir}} - \bar{\psi}_L^{\text{mir}} \psi_R) \quad (1.25)$$

with the coupling constant m_0 having the mass dimension of one. m_0 is just an effective contribution of the chiral invariant component of masses. Diagonalizing the mass matrix obtained by combining the chiral invariant mass term in Eq.(1.25) together with the Yukawa terms $g_1 \bar{\psi} \sigma \psi + g_2 \bar{\psi}^{\text{mir}} \sigma \psi^{\text{mir}}$, the mass eigenvalues can be written as

$$m_{\pm} = \sqrt{m_0^2 + G_{\pm}^2 \langle \sigma \rangle^2} \mp G_{\pm} \langle \sigma \rangle, \quad (1.26)$$

where $G_{\pm} = (g_2 \pm g_1)/2$. The expectation value of the scalar meson $\langle \sigma \rangle$ has a finite value in vacuum, while it will eventually vanish when the chiral symmetry is restored. A schematic view of the density dependence of the mass eigenvalues are shown in Fig.1.2. In the high-density limit, the masses of the two nucleons are degenerate to the value of m_0 . With a not small m_0 , the mass of the ground-state nucleon keeps its value around 939 MeV even in the chiral restored phase. This behavior is consistent with the lattice simulations [7].

The mixing between a naive state ψ and a mirror state ψ^{mir} plays an important role. It comes a non-negligible contribution to a transition from the naive state to the mirror state as shown in the left panel (hadronic picture) of Fig.1.3. We emphasize that the chiral invariant mass term can exist only when there are both of the naive state and the mirror state.

Next, let us discuss the mirror representation based on the quark picture. One choice of the interpolating field of proton is

$$\psi_R \sim u_R(u^T C d) = P_R \cdot u S, \quad (1.27)$$

where u, d are up, down quark, and $S \equiv u^T C d = u_R^T C d_R + u_L^T C d_L$ is a scalar diquark field. For this interpolating field, one choice of the excited state is

$$(\gamma^\mu \partial_\mu u_R)(u^T C d) = P_L \cdot (\gamma^\mu \partial_\mu u) S \sim \psi_L^{\text{mir}}. \quad (1.28)$$

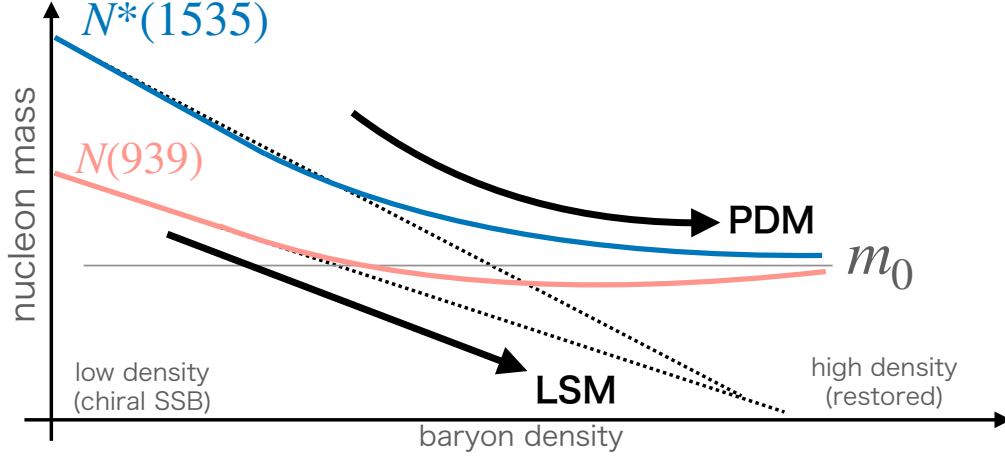


Figure 1.2: Comparison between the density dependences of nucleon masses in the linear sigma model and in a parity doublet model with the chiral invariant mass m_0 .

In Eqs.(1.27)-(1.28), two expressions u_R and $\gamma_\mu \partial^\mu u_R$ obey the same chiral transformation, $u_R \rightarrow g_R u_R$ and $\gamma_\mu \partial^\mu u_R \rightarrow g_R \gamma_\mu \partial^\mu u_R$, while they have the opposite chiralities. In other words, the baryon fields in the two expressions have the same chiral representations but the opposite chirality, which are just the naive and the mirror fields, as shown in the right panel (quark picture) of Fig.1.3.

Let us consider again the dependence of the ground-state nucleon mass on the environment (temperature and/or density). Chiral invariant mass may play more important role in hot and/or dense matter, because the nucleon mass is dominated by the chiral invariant mass m_0 at high temperature and/or high density, where the chiral symmetry is expected to be restored as seen in Fig.1.2.

In this thesis, we apply a chiral model with chiral invariant masses to the physics of neutron stars. Neutron star, which is explained later in Sec.1.5, is a ‘‘cosmic laboratory’’ of the nuclear physics at low temperature and high density. For the high density nuclear physics, it is very difficult to conduct experiments in the Earth, and it is also difficult to perform lattice simulations due to the sign problem. We apply the PDM to neutron star physics, and discuss the relation between the chiral invariant mass and the neutron star observations.

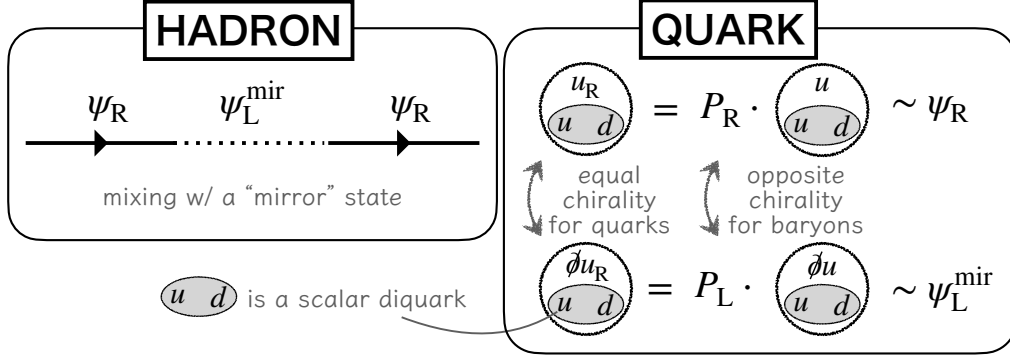


Figure 1.3: Parity doubling structure of baryons based on hadronic picture vs. quark picture. The left panel (hadronic picture) indicates the mixing between the baryon field in the “naive” representation, ψ_R , and the one in the “mirror” representation, ψ_L^{mir} . In the right panel (quark picture), $P_{L,R}$ is the chiral projection operators, u and d are up and down quarks, and the gray-shaded pair of u and d indicates a scalar diquark. The baryon field ψ_L^{mir} in the bottom of the panel, which has a $\gamma^\mu \partial_\mu$ in front, has the opposite chirality while it belongs to the same chiral representation as ψ_R .

Here, we mention some other works for the chiral invariant mass of nucleons. As is said, the lattice simulations [6–10] imply that the ground-state nucleon mass is almost maintained even at sufficiently high temperature, which implies that the nucleon mass may not be sensitive to the environments. While, there are the results [63–65] in which the EOS calculated from the hadron resonance gas (HRG) model with constant hadron masses is well matched with the one from the lattice QCD analysis up to around the critical temperature. This implies that the hadronic effective model with constant hadron masses provides a good approximation even near the chiral restored phase. There are also some relations to the hyperon puzzle. The hyperon puzzle is the long-term problem that the introduction of the hyperons makes the EOS of a neutron star too soft to support the heaviest observed neutron star. This puzzle is due to the large number of fermions, because there is no Pauli blocking between different fermions. One of the ways for relaxing the hyperon puzzle is setting a lower bound of the nucleon mass [66]. The notion of the lower bound of the nucleon mass is very similar with the chiral invariant mass. Furthermore, the work in Refs. [56, 57] studied the parity doubling model for nucleons and Δ baryons, and showed that the chi-

ral invariant mass relaxes the softening by Δ matter at higher density. This implies that the chiral invariant component of hadron masses may stiffen the EOS at higher density.

Because the core of a neutron star is constructed from the homogeneous “nuclear matter” we will introduce nuclear matter in Sec.1.4.

1.4 Nuclear matter and the saturation properties

“Nuclear matter” describes the homogeneous environment made of nucleon many-body system bounded by only nuclear force. Nuclear matter is characterized by the baryon number density $n_B = n_p + n_n$ and the isospin density $n_I = (n_p - n_n)/2$, where n_p is the proton number density and n_n is the neutron number density. It is well known that the baryon number density saturates for the size of matter at the value of $n_0 \approx 0.16 \text{ fm}^{-3}$ called the nuclear saturation density.

According to the Bethe–Weizsäcker mass formula, the binding energy of an atomic nucleus is

$$E_{\text{BW}} = c_V A - c_S A^{2/3} - c_C \frac{Z(Z-1)}{A^{1/3}} - c_A \frac{(N-Z)^2}{4A} + c_P \frac{1}{A^{1/2}}, \quad (1.29)$$

where $A(= Z+N)$ is the number of nucleons, Z is the proton number, and N is the neutron number. This semi-empirical formula shows that there are five contributions: a volume term with a coefficient c_V , a surface term with c_S , a Coulomb term with c_C , an asymmetry term with c_A , and a pairing term with c_P . In the nuclear matter, we neglect the contribution of electromagnetic forces. Taking infinite size limit, $A \rightarrow \infty$, the binding energy per nucleon for the symmetric matter ($N = Z$) is

$$E_{\text{BW}}/A \xrightarrow[N=Z]{A \rightarrow \infty} c_V (\approx 16 \text{ MeV}). \quad (1.30)$$

In thermodynamics, nuclear matter is treated by the grand canonical ensemble, with the grand potential density Ω as a function of the chemical potential μ_p for protons and μ_n for neutrons. The number densities are calculated by differentiating the pressure $P = -\Omega$ as

$$n_p \equiv \frac{\partial P}{\partial \mu_p} = \frac{Z}{V}, \quad n_n \equiv \frac{\partial P}{\partial \mu_n} = \frac{N}{V}, \quad (1.31)$$

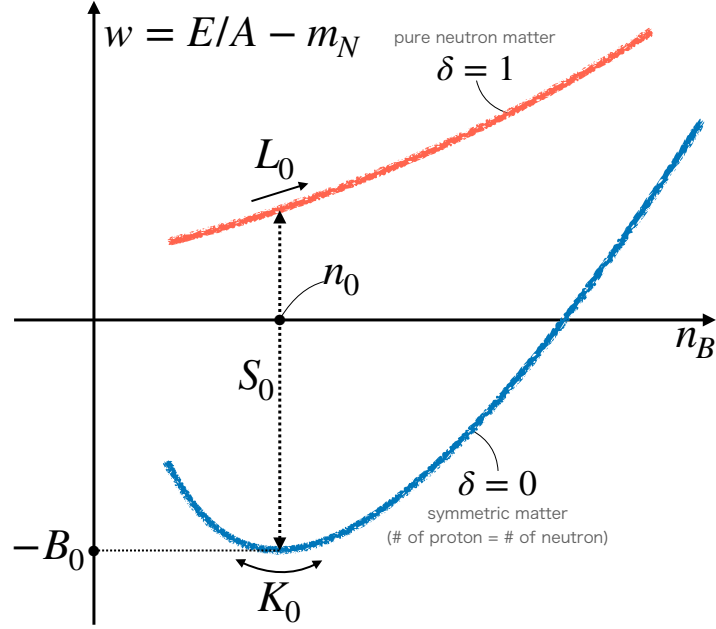


Figure 1.4: Illustration of the energy per nucleon $w = E/A - m_N$ for the symmetric matter and the pure neutron matter (totally asymmetric matter). n_B , B_0 , K_0 , S_0 , and δ denote the baryon number density, the binding energy, the incompressibility, the symmetry energy, and the asymmetry, respectively.

and

$$n_B \equiv \frac{\partial P}{\partial \mu_B} = n_p + n_n, \quad n_I \equiv \frac{\partial P}{\partial \mu_I} = \frac{n_p - n_n}{2}, \quad (1.32)$$

where $\mu_B = (\mu_p + \mu_n)/2$ is the baryon number chemical potential and $\mu_I = \mu_p - \mu_n$ is the isospin chemical potential. The energy density ϵ is calculated by performing Legendre transformation as

$$\epsilon \equiv \mu_p n_p + \mu_n n_n - P = \mu_B n_B + \mu_I n_I - P. \quad (1.33)$$

Let us define the energy density per nucleon (shifted the origin by the nucleon mass m_N) as

$$w \equiv \frac{E}{A} - m_N = \frac{\epsilon}{n_B} - m_N. \quad (1.34)$$

Figure 1.4 shows a schematic graph of w for the symmetric nuclear matter $n_I = 0$ (lower blue curve), and that for the pure neutron matter $n_p = 0$ (upper red curve). As said, nuclear matter is saturated at the saturation density n_0 with the binding energy $B_0 = 16$ MeV, which is indicated by the minimum point of the blue curve in Fig.1.4. Expanding the energy in terms of ¹ $x = (n_B - n_0)/(3n_0)$ and the asymmetry $\delta = (n_p - n_n)/(n_p + n_n) = 2n_I/n_B$ at the saturation point, we obtain

$$w(x, \delta) = -B_0 + 0 \cdot x + \frac{1}{2}K_0x^2 + E_{\text{sym}}(x)\delta^2 + \dots \quad (1.36)$$

$E_{\text{sym}}(x)$ is the symmetry energy which is expanded as

$$E_{\text{sym}}(x) = S_0 + L_0x + \frac{1}{2}K_{\text{sym}}x^2 + \dots \quad (1.37)$$

The symmetry energy is approximately equal to the difference between the energy of the symmetric matter and that of the pure neutron matter,

$$E_{\text{sym}}(x) \approx w(x, 1) - w(x, 0). \quad (1.38)$$

Other quantities shown in Fig.1.4 are expressed as follows: the incompressibility (or the compression modulus) K_0 is given by

$$K_0 \equiv \frac{\partial^2 w}{\partial x^2}(0, 0) = 9n_0 \left(\frac{\partial \mu_B}{\partial n_B} \right)_0, \quad (1.39)$$

where the lower subscript 0 means $x = \delta = 0$. Since K_0 is the curvature of the energy per nucleon at the saturation point, it is interpreted as literary incompressibility for the saturated nuclear matter. The symmetry energy at the saturation density S_0 is expressed as

$$S_0 \equiv \frac{1}{2} \frac{\partial^2 w}{\partial \delta^2}(0, 0) = E_{\text{sym}}(0) = \frac{n_0}{8} \left(\frac{\partial \mu_I}{\partial n_I} \right)_0. \quad (1.40)$$

¹The factor 3 of x is just convention. The thermodynamic quantities for symmetric nuclear matter are often expanded by the fermi momentum k_F which is proportional to $n_B^{1/3}$. Therefore, for example, the incompressibility in Eq.(1.39) can be also defined in terms of the Fermi momentum as

$$K_0 = \left(k_F^2 \frac{\partial^2 w}{\partial k_F^2} \right)_0 = 9n_0^2 \left(\frac{\partial^2 w}{\partial n_B^2} \right)_0, \quad (1.35)$$

where the lower subscript 0 means $x = \delta = 0$.

Table 1.1: Empirical values of the saturation parameters for nuclear matter used as physical inputs in this thesis. The listed range of the slope parameter is referred in Ref. [67–69].

n_0 [fm $^{-3}$]	B_0 [MeV]	K_0 [MeV]	S_0 [MeV]	L_0 [MeV]
0.16	16	240	31	30–90

The slope parameter at the saturation density L_0 is expressed as

$$L_0 \equiv \frac{1}{2} \frac{\partial^2 w}{\partial x \partial \delta^2}(0, 0) = \frac{\partial E_{\text{sym}}}{\partial x}(0) = 3S_0 + 3n_0 \frac{\partial E_{\text{sym}}}{\partial n_B}(0). \quad (1.41)$$

We summarize some empirical values of the saturation parameters in Table 1.1.

1.5 M - R relation for neutron stars

Neutron star is one of the densest objects next to the black holes, whose density can reach several times of the normal nuclear density. The internal structure of a neutron star consists of roughly two parts, the crust and the core. Especially, the core of a neutron star, which is the dominant part of a neutron star, is basically considered to be composed of homogeneous nuclear matter.

Mass and radius of a neutron star can be calculated using an EOS through the Tolman–Oppenheimer–Volkoff (TOV) equation. The TOV equation is the differential equation derived from the Einstein equation with the static spherical metric, which means hydrostatic balance. If the EOS of neutron stars is determined uniquely, static spherical neutron stars are parametrized by central density (or equivalently, central pressure). Then, the set of mass and radius profiles of the neutron stars with various values of central density is called an M - R relation, or an M - R curve. Actually, under some physical assumption, it is known that there is one-to-one correspondence between EOSs and M - R relations, as shown in Fig.1.5. Since EOSs are calculated from microscopic theory, the TOV equation can be said to connect the microscopic physics and the macroscopic physics. If we have observational data of neutron stars, we can know some properties of the microscopic quantities, such as the chiral condensate and the chiral invariant mass.

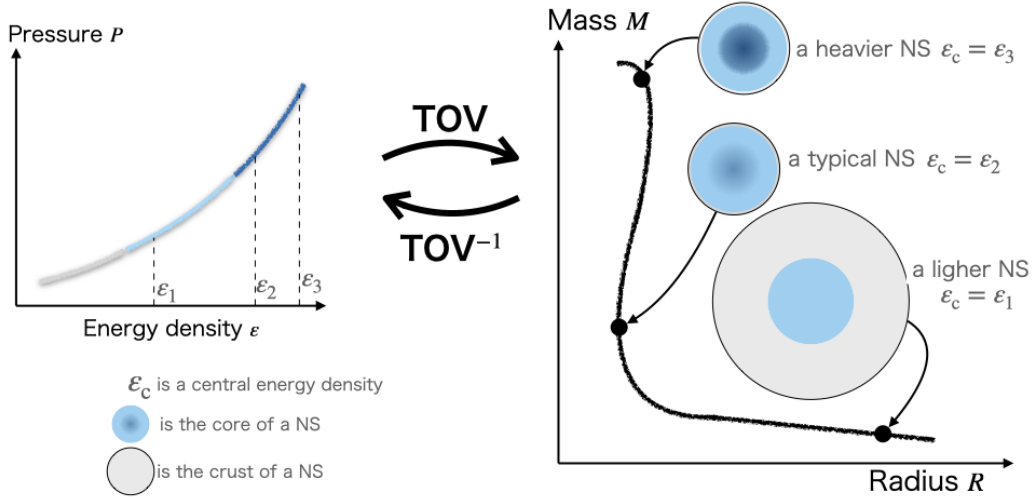


Figure 1.5: Schematic picture of the correspondence between an EOS and an M - R relation of neutron stars (NSs).

Today, there are several observational data of neutron stars. In 2017, the LIGO-Virgo observed the gravitational data of a binary neutron star inspiral, which is called GW170817 [18–20]. While, NASA launched a telescope called The Neutron Star Interior Composition ExploreR (NICER) in 2016, and observed the isolated millisecond pulsar called PSR J0030+0451 in 2019 [21, 22]. Moreover, in 2021, NICER observed the millisecond pulsar PSR J0740+6620 and provided us the radius estimations [23, 24], The pulsar J0740+6620 was one of well known neutron stars which is heaviest [70].

The useful tools to access the properties of dense matter are the recent observations for neutron star, which tightly constrain the EOS of matter (see, e.g., Ref. [60, 71]). The existence of the heavy neutron stars with $1.91M_{\odot}$ [72–74], $2.01M_{\odot}$ [75], and $M = 2.08 \pm 0.07M_{\odot}$ [76], the radius constraint $R_{1.4} \lesssim 13$ km for the typical neutron star with $1.4M_{\odot}$ deduced from the gravitational event GW170817 [18], and recent NICER constraints on $R_{1.4} \simeq R_{2.08} \simeq 12$ – 13 km [23, 24, 77], disfavor the strong first order phase transitions for the domain between the nuclear saturation density ($n_0 \simeq 0.16 \text{ fm}^{-3}$) and the core density achieved in neutron stars with $\sim 2M_{\odot}$. The core baryon density of the neutron star with $\sim 2M_{\odot}$ is considered to be around $\gtrsim 4$ – $5n_0$, presumably high enough to apply quark matter descriptions, so we infer that nuclear matter smoothly transforms into quark matter (modulo weak first

order phase transitions).

1.6 Quark-hadron crossover in neutron star

In this last section of the Ch.1, we show the recent trend that the extrapolation of the hadronic picture to higher density is questionable, and the EOS based on crossover from the hadronic phase to the quark phase is well matched with the observational data.

A lot of works researched the parity doublet structure by constructing nuclear matter and neutron star EOS (see, e.g., Refs. [25–35, 37–46, 48–52]). In the PDM, the masses of positive-parity and negative-parity nucleons are split by the chiral condensate and get degenerated to the chiral invariant mass in chiral restored phase. Some lattice simulations support the idea of the chiral invariant mass, which indicated the parity degeneracy of nucleons at finite mass [7]. By increasing m_0 , the nucleon mass can attain the experimental value through weak coupling between nucleons and chiral condensates. Consequently, the chiral condensates become less responsive to variations in the nuclear medium, resulting in a mild chiral restoration that is driven by the density increase. The influence of m_0 is more prominent in high temperature and/or high density environments such as neutron stars. In models like σ - ω - ρ [78–80], a decrease in the σN coupling causes a reduction in the attractive σ exchange. Thus, weaker repulsion by the ω exchange is sufficient to replicate the physics near the saturation density. This trend intensifies at higher baryon density where σ fields diminish while ω fields amplify.

The PDM has undergone multiple modifications to incorporate the properties of nucleon and nuclear matter. Recent studies [37, 81] have revisited the decay width estimate and found that the inclusion of derivative interactions, which were previously neglected [13], permits larger values of m_0 . The authors argue that relatively higher values of m_0 , ranging from 500, MeV to 900, MeV, are more reasonable for explaining the saturation properties of nuclear matter. Specifically, [37] demonstrated that the inclusion of a σ^6 term yields an incompressibility value of the empirical value $K \approx 240$, MeV, which was substantially higher in earlier analyses. Furthermore, [48] extended the analyses to neutron star matter and constrained the chiral invariant mass to $m_0 \gtrsim 600$, MeV based on the tidal deformability inferred from the neutron star merger GW170817 [18–20].

In a previous study [48] using the PDM, the hadronic EOSs were extrap-

olated to a baryon density of $n_B \approx 3n_0$ ($n_0 \simeq 0.16, \text{fm}^{-3}$: nuclear saturation density). However, it has been pointed out in [58–61] that pure hadronic descriptions become questionable at $n_B \gtrsim 2n_0$ due to the significance of nuclear many-body forces. This implies that quark descriptions are required even before the formation of quark matter. To address this, it has been proposed to construct an EOS by interpolating between the hadronic matter EOS at $n_B \lesssim 2n_0$ and the quark matter EOS at high densities ($n_B \gtrsim 5n_0$). In the present work, the authors adopted a three-flavor Nambu–Jona-Lasinio (NJL)-type model, leading to color-flavor-locked (CFL) color-superconducting matter, to describe the quark matter, and investigated effective interactions that satisfy the two-solar-mass ($2M_\odot$) constraint. For the hadronic EOSs, non-relativistic nuclear many-body calculations were employed. In [50, 52], an effective model that combines the PDM with a two-flavor NJL-type model, assuming no color-superconductivity, was constructed.

The standard Nambu–Jona-Lasinio (NJL) model [62] with additional effective interactions, such as vector repulsion and diquark attraction [82], is used to describe quark matter. The vector repulsion plays a crucial role in chiral restoration by limiting the density growth and thereby smoothing out the chiral restoration [83, 84]. The inclusion of diquark terms leads to the color-flavor-locked (CFL) phase in which ud -, ds -, and su -diquark pairs condense, favoring a larger quark Fermi sea [85]. After considering these competing effects, we found that a significant amount of the chiral condensates remains in quark matter, and the effective masses for up- and down-quarks are around 50 MeV, while those for strange quarks are around 300 MeV at $n_B \sim 5n_0$ [60].

We have developed a three-window approach, as presented in Refs. [58, 59, 86], which involves constructing a series of unified EOSs that cover a range from nuclear to quark matter. These EOSs are then constrained using observations of neutron stars [61, 82, 87]. To construct the EOS, we employ a nuclear model for densities $n_B \lesssim 2n_0$, a quark model for $n_B \gtrsim 5n_0$, and interpolate between them for densities $n_B \simeq 2\text{--}5n_0$. By adjusting the parameters of the model, we can ensure that the resulting EOS is consistent with observations of neutron stars. Furthermore, our approach enables us to predict physical quantities beyond the EOS and gain insight into the underlying microphysics, as the microscopic degrees of freedom are explicitly accounted for [60].

Chapter 2

Chiral Invariant Mass and Neutron Stars

The content of this chapter is based on our paper [1].

Here we explain two models for hadronic matter in the low-density region and quark matter in the high-density region, and how to construct a unified EOS for crossover in neutron stars.

For the hadronic matter, the parity doublet model is used. To introduce massive vector mesons with chiral symmetry, we use the hidden local symmetry (HLS) [88, 89]. Some equivalent method to the HLS is shown in Ref. [89].

For quark matter, assuming the CFL phase as following Refs. [60, 61], we use an NJL-type model with additional diquark pairing and vector interactions.

Assuming a smooth transition between hadronic and quark matter, we construct the unified EOS to interpolate the resultant EOSs.

In this chapter, we write the integrals over space as, $\int_x = \int d^4x$, $\int_{\mathbf{x}} = \int d^3\mathbf{x}$, and over momentum as, $\int_{\mathbf{p}} = \int \frac{d^3\mathbf{p}}{(2\pi)^3}$.

2.1 Nuclear matter

2.1.1 Parity doublet model

First, we explain briefly an chiral hadronic effective model based on the parity doublet structure for nucleons [5, 13, 37].

For the ground-state nucleon $N(939)$, the parity doublet partner is regarded as the negative-parity excited nucleon $N^*(1535)$ in our model. We introduce the following two baryon fields ψ and ψ^{mir} for expressing these nucleons. The fields ψ and ψ^{mir} transform under the chiral symmetry as

$$\psi_L \rightarrow g_L \psi_L, \quad \psi_R \rightarrow g_R \psi_R, \quad (2.1)$$

$$\psi_L^{\text{mir}} \rightarrow g_R \psi_L^{\text{mir}}, \quad \psi_R^{\text{mir}} \rightarrow g_L \psi_R^{\text{mir}}, \quad (2.2)$$

where g_L and g_R are the elements of $SU(2)_L$ and $SU(2)_R$ groups, respectively. The left- and right-handed baryon fields for ψ and ψ^{mir} are defined as

$$\psi_{L,R} = P_{L,R} \psi, \quad \psi_{L,R}^{\text{mir}} = P_{L,R} \psi^{\text{mir}}, \quad (2.3)$$

where $P_{L,R} = (1 \pm \gamma_5)/2$ are the chiral projection operators. We assign positive parity for ψ and negative parity for ψ^{mir} :

$$\psi \xrightarrow{P} \gamma_0 \psi, \quad \psi^{\text{mir}} \xrightarrow{P} -\gamma_0 \psi^{\text{mir}}. \quad (2.4)$$

We introduce a 2×2 matrix field M for the scalar meson σ (iso-singlet) and the pions π (iso-triplet). M transforms as

$$M \rightarrow g_L M g_R^\dagger. \quad (2.5)$$

The vector mesons are introduced based on the HLS [37], by decomposing the scalar meson field as

$$M = \xi_L^\dagger \sigma \xi_R, \quad (2.6)$$

where $\xi_{L,R}$ are matrix fields including pions, and σ is not a matrix but a scalar field. Under the chiral symmetry and the HLS, the fields $\xi_{L,R}$ transform as

$$\xi_L \rightarrow h \xi_L g_L^\dagger, \quad \xi_R \rightarrow h \xi_R g_R^\dagger, \quad (2.7)$$

where $h \in U(2)_{\text{HLS}}$. We can parametrize the fields $\xi_{L,R}$ in the unitary gauge of the HLS as

$$\xi_L = e^{-i\pi/f_\pi}, \quad \xi_R = e^{i\pi/f_\pi}, \quad (2.8)$$

where $\pi = \sum_{a=1,2,3} \pi^a \tau_a / 2$ is the field for pions, and τ_a being the Pauli matrices. The following 1-forms are the basic quantities to construct the Lagrangian

$$\begin{aligned} \hat{\alpha}_\mu^\parallel &= \frac{1}{2i} \left[(D_\mu \xi_R) \xi_R^\dagger + (D_\mu \xi_L) \xi_L^\dagger \right], \\ \hat{\alpha}_\mu^\perp &= \frac{1}{2i} \left[(D_\mu \xi_R) \xi_R^\dagger - (D_\mu \xi_L) \xi_L^\dagger \right]. \end{aligned} \quad (2.9)$$

For the fields ξ_L and ξ_R , the covariant derivatives are defined as the following

$$D_\mu \xi_L = (\partial_\mu - ig_\omega \omega_\mu T_0 - ig_\rho \rho_\mu^a T_a) \xi_L - i \xi_L \tilde{V}_\mu \quad (2.10)$$

$$D_\mu \xi_R = (\partial_\mu - ig_\omega \omega_\mu T_0 - ig_\rho \rho_\mu^a T_a) \xi_R - i \xi_R \tilde{V}_\mu, \quad (2.11)$$

where ω_μ is the gauge field for $U(1)_{\text{HLS}}$ with the gauge coupling g_ω , ρ_μ^a is the one for $SU(2)_{\text{HLS}}$ with g_ρ , and $T_0 = 1/2$ and $T_a = \tau_a/2$ are the $U(2)$ generators. As usual, external gauge fields for the chiral symmetry, \tilde{V}_μ , is introduced to keep track the correspondence between the generating functional of QCD and its effective Lagrangian of hadronic fields. After using the correspondence to constrain the form of the effective Lagrangian, we set the values of the external fields as

$$\tilde{V}_\mu = \frac{1}{2} \begin{pmatrix} \mu_Q & 0 \\ 0 & -\mu_Q \end{pmatrix} \delta_\mu^0. \quad (2.12)$$

There are a nucleon part and a meson part in our effective Lagrangian for hadrons as

$$\mathcal{L}_{\text{PDM}} = \mathcal{L}_N + \mathcal{L}_M. \quad (2.13)$$

The nucleon part is

$$\begin{aligned} \mathcal{L}_N &= \bar{\psi} i \gamma^\mu D_\mu \psi + \bar{\psi}^{\text{mir}} i \gamma^\mu D_\mu \psi^{\text{mir}} \\ &\quad - g_1 (\bar{\psi}_L M \psi_R + \bar{\psi}_R M^\dagger \psi_L) \\ &\quad - g_2 (\bar{\psi}_L^{\text{mir}} M^\dagger \psi_R^{\text{mir}} + \bar{\psi}_R^{\text{mir}} M \psi_L^{\text{mir}}) \\ &\quad - m_0 (\bar{\psi}_L \psi_R^{\text{mir}} - \bar{\psi}_R \psi_L^{\text{mir}} - \bar{\psi}_L^{\text{mir}} \psi_R + \bar{\psi}_R^{\text{mir}} \psi_L) \\ &\quad + a_{VNN} \left[\bar{\psi}_L \xi_L^\dagger \gamma^\mu \hat{\alpha}_\mu^\parallel \xi_L \psi_L + \bar{\psi}_R \xi_R^\dagger \gamma^\mu \hat{\alpha}_\mu^\parallel \xi_R \psi_R \right] \\ &\quad + a_{VNN} \left[\bar{\psi}_L^{\text{mir}} \xi_R^\dagger \gamma^\mu \hat{\alpha}_\mu^\parallel \xi_R \psi_L^{\text{mir}} + \bar{\psi}_R^{\text{mir}} \xi_L^\dagger \gamma^\mu \hat{\alpha}_\mu^\parallel \xi_L \psi_R^{\text{mir}} \right] \\ &\quad + a_{0NN} \left[\bar{\psi}_L \gamma^\mu \text{tr}(\hat{\alpha}_\mu^\parallel) \psi_L + \bar{\psi}_R \gamma^\mu \text{tr}(\hat{\alpha}_\mu^\parallel) \psi_R \right] \\ &\quad + a_{0NN} \left[\bar{\psi}_L^{\text{mir}} \gamma^\mu \text{tr}(\hat{\alpha}_\mu^\parallel) \psi_L^{\text{mir}} + \bar{\psi}_R^{\text{mir}} \gamma^\mu \text{tr}(\hat{\alpha}_\mu^\parallel) \psi_R^{\text{mir}} \right], \end{aligned} \quad (2.14)$$

where the covariant derivatives on the nucleon fields are defined as

$$D_\mu \psi_{L,R} = (\partial_\mu - iV_\mu) \psi_{L,R}, \quad D_\mu \psi_{L,R}^{\text{mir}} = (\partial_\mu - iV_\mu) \psi_{L,R}^{\text{mir}}, \quad (2.15)$$

with

$$V_\mu = \begin{pmatrix} \mu_B + \mu_Q & 0 \\ 0 & \mu_B \end{pmatrix} \delta_\mu^0. \quad (2.16)$$

The meson part is

$$\mathcal{L}_M = \mathcal{L}_M^{\text{kin}} - V_M - V_{\text{SB}} + \mathcal{L}_M^{\text{vector}} , \quad (2.17)$$

where $\mathcal{L}_M^{\text{vector}}$ includes the kinetic and mass terms for vector mesons, V_{SB} is the potential including the explicit chiral symmetry breaking for the scalar and pseudo-scalar mesons, V_M is the chiral symmetric potential, and $\mathcal{L}_M^{\text{kin}}$ is the kinetic term. The scalar and pseudo-scalar mesons terms are given as [37]

$$\mathcal{L}_M^{\text{kin}} = \frac{1}{4} \text{tr} [D_\mu M D^\mu M^\dagger] = \frac{1}{2} \partial_\mu \sigma \partial^\mu \sigma + \sigma^2 \text{tr} [\hat{\alpha}_\mu^\perp \hat{\alpha}_\perp^\mu] , \quad (2.18)$$

$$\begin{aligned} V_M &= -\frac{1}{4} \bar{\mu}^2 \text{tr} [M M^\dagger] + \frac{1}{16} \lambda_4 (\text{tr} [M M^\dagger])^2 \\ &\quad - \lambda_6 \frac{1}{48} (\text{tr} [M M^\dagger])^3 , \end{aligned} \quad (2.19)$$

$$V_{\text{SB}} = -\frac{1}{4} m_\pi^2 f_\pi \text{tr} [M + M^\dagger] . \quad (2.20)$$

The vector mesons part $\mathcal{L}_M^{\text{vector}}$ is given by

$$\begin{aligned} \mathcal{L}_M^{\text{vector}} &= -\frac{1}{4} \omega_{\mu\nu} \omega^{\mu\nu} + \frac{m_\omega^2}{2g_\omega^2} \text{tr} [\hat{\alpha}_\mu^\parallel] \text{tr} [\hat{\alpha}_\parallel^\mu] \\ &\quad - \frac{1}{2} \text{tr} [\rho_{\mu\nu} \rho^{\mu\nu}] \\ &\quad + \frac{m_\rho^2}{g_\rho^2} \left(\text{tr} [\hat{\alpha}_\mu^\parallel \hat{\alpha}_\parallel^\mu] - \frac{1}{2} \text{tr} [\hat{\alpha}_\mu^\parallel] \text{tr} [\hat{\alpha}_\parallel^\mu] \right) , \end{aligned} \quad (2.21)$$

where ω^μ is the vector field for ω meson with the mass m_ω , and ρ^μ is the one for ρ meson with the mass m_ρ . $\omega^{\mu\nu}$ and $\rho^{\mu\nu}$ are the field strengths for these mesons. The second and forth terms include the mass terms for ω^μ and ρ^μ as

$$\begin{aligned} \text{tr} [\hat{\alpha}_\mu^\parallel] \text{tr} [\hat{\alpha}_\parallel^\mu] &= g_\omega^2 \omega^\mu \omega_\mu , \\ \text{tr} [\hat{\alpha}_\mu^\parallel \hat{\alpha}_\parallel^\mu] - \frac{1}{2} \text{tr} [\hat{\alpha}_\mu^\parallel] \text{tr} [\hat{\alpha}_\parallel^\mu] &= \frac{1}{2} g_\rho^2 \rho_\mu^a \rho_a^\mu + \dots , \end{aligned} \quad (2.22)$$

where “...” stands for interaction terms.

In the present analysis, we calculate the thermodynamic potential in the mean field approximation as

$$\langle \sigma \rangle = \sigma , \quad \langle \omega^\mu \rangle = \omega \delta_0^\mu , \quad \langle \rho^\mu \rangle = \left(\rho - \frac{\mu Q}{g_\rho} \right) T_3 \delta_0^\mu . \quad (2.23)$$

We assume that the mean fields are independent of the spatial coordinates. Mean field ρ is defined in such a way that \mathcal{L}_M does not explicitly include μ_Q .

The effective chemical potentials of protons and neutrons are introduced for simplicity as

$$\begin{aligned}\mu_p^* &= \mu_Q + \mu_B - g_{\omega NN} \omega - \frac{1}{2} g_{\rho NN} \rho , \\ \mu_n^* &= \mu_B - g_{\omega NN} \omega + \frac{1}{2} g_{\rho NN} \rho ,\end{aligned}\tag{2.24}$$

where

$$\begin{aligned}g_{\omega NN} &= (a_{VNN} + a_{0NN})g_\omega , \\ g_{\rho NN} &= a_{VNN}g_\rho .\end{aligned}\tag{2.25}$$

For the hadronic matter based on the PDM, The thermodynamic potential is given as [37]

$$\begin{aligned}\Omega_{\text{PDM}} &= -2 \sum_{i=1,2} \sum_{\alpha=p,n} \int_{\mathbf{p}}^{k_F} (\mu_\alpha^* - E_{\mathbf{p}}^i) \\ &\quad + V(\sigma) - V(f_\pi) - \frac{1}{2} m_\omega^2 \omega^2 - \frac{1}{2} m_\rho^2 \rho^2 .\end{aligned}\tag{2.26}$$

The energy $E_{\mathbf{p}}^i = \sqrt{(m_i)^2 + (\mathbf{p})^2}$ is for a relevant particle with mass m_i and momentum \mathbf{p} , and the label $i = 1, 2$ are corresponding to the grand-state nucleon $N(939)$ and the negative-parity excited nucleon $N^*(1535)$, respectively. $k_F = \sqrt{(\mu_\alpha^*)^2 - (m_i)^2}$ is the fermi momentum for the relevant particle, and the above integral region is restricted as $|\mathbf{p}| < k_F$. We emphasize that the no-sea approximation is used in the thermodynamic potential for hadronic matter, assuming that the structure of the Dirac sea remains the same for the vacuum and low-density medium.

The scalar field potential $V(\sigma)$ is

$$V(\sigma) = -\frac{1}{2} \bar{\mu}^2 \sigma^2 + \frac{1}{4} \lambda_4 \sigma^4 - \frac{1}{6} \lambda_6 \sigma^6 - m_\pi^2 f_\pi \sigma ,\tag{2.27}$$

and the vacuum value $V(f_\pi)$ is subtracted in Eq.(2.26) to set the value of the total potential zero in vacuum.

In neutron stars, the leptonic parts should be included in the thermodynamic potential, and we rewrite the label for the total thermodynamic

potential Ω_{H} as

$$\Omega_{\text{H}} = \Omega_{\text{PDM}} + \sum_{l=e,\mu} \Omega_l, \quad (2.28)$$

where the thermodynamic potentials for leptons Ω_l is given by

$$\Omega_l = -2 \int_{\mathbf{p}}^{k_F} (\mu_l - E_{\mathbf{p}}^l), \quad (2.29)$$

with spin degree of freedom 2. The following stationary conditions, which correspond to the equation of motion, determine the values of the mean fields

$$0 = \frac{\partial \Omega_{\text{H}}}{\partial \sigma} = \frac{\partial \Omega_{\text{H}}}{\partial \omega} = \frac{\partial \Omega_{\text{H}}}{\partial \rho}. \quad (2.30)$$

In neutron stars, we impose the beta equilibrium and the charge neutrality condition represented as

$$\mu_e = \mu_{\mu} = -\mu_Q, \quad \frac{\partial \Omega_{\text{H}}}{\partial \mu_Q} = n_p - n_l = 0. \quad (2.31)$$

The hadronic matter pressure is finally obtained as

$$P_{\text{H}} = -\Omega_{\text{H}}. \quad (2.32)$$

2.1.2 Model parameters

For determining the model parameters, as following Ref. [37], we use the physical inputs (Table 2.1). Table 2.2 shows the determined parameters for several typical choices of m_0 .

We also list the values of the slope parameter L_0 in our model in Table 2.2. For a smaller chiral invariant mass, the slope parameter L_0 becomes larger. In the high density region, the higher order contributions in the expansion around the nuclear saturation density become important, and hence, the differences due to the values of m_0 appear in the high density. As we will show in the next section, the EOS is stiffer for a smaller m_0 . This can be understood as follows. For reproducing the nucleon mass in vacuum, the Yukawa coupling of σ becomes larger for a smaller m_0 . It implies that the attractive force between nucleons becomes stronger, which corresponds to

Table 2.1: Physical inputs in vacuum in unit of MeV.

m_π	f_π	m_ω	m_ρ	$m_+(=m_N)$	m_-
140	92.4	783	776	939	1535

Table 2.2: Values of model parameters determined for several choices of m_0 . The values of the slope parameter L_0 is also shown as output.

m_0 [MeV]	500	600	700	800	900
g_1	9.02	8.48	7.81	6.99	5.96
g_2	15.5	14.9	14.3	13.4	12.4
$\bar{\mu}^2/f_\pi^2$	22.7	22.4	19.3	11.9	1.50
λ_4	41.9	40.4	35.5	23.1	4.43
$\lambda_6 f_\pi^2$	16.9	15.8	13.9	8.89	0.636
$g_{\omega NN}$	11.3	9.13	7.30	5.66	3.52
$g_{\rho NN}$	7.31	7.86	8.13	8.30	8.43
L_0 [MeV]	93.76	86.24	83.04	81.33	80.08

the larger values of $g_{1,2}$. Meanwhile, the repulsive force between nucleons, which corresponds to $g_{\omega NN}$, becomes stronger for a smaller m_0 , because of the balance between the attractive and repulsive forces for constructing nuclear matter. In the high density region, the contribution for σ becomes smaller while the contribution for ω becomes larger, and therefore the EOS for a smaller m_0 becomes stiffer in the high density region.

2.2 Unified EOS with CFL phase

2.2.1 NJL-type model for quark matter

Based on Ref. [61], we use the following NJL-type model as an quark effective model, including the 4-Fermi interactions which cause the spontaneous chiral symmetry breaking and the color-superconductivity. The Lagrangian is given by

$$\mathcal{L}_{\text{CSC}} = \mathcal{L}_0 + \mathcal{L}_\sigma + \mathcal{L}_d + \mathcal{L}_{\text{KMT}} + \mathcal{L}_{\text{vec}} , \quad (2.33)$$

where

$$\mathcal{L}_0 = \bar{q}(i\gamma^\mu\partial_\mu - \hat{m}_q + \gamma_\mu\hat{A}^\mu)q , \quad (2.34)$$

$$\mathcal{L}_\sigma = G \sum_{A=0}^8 [(\bar{q}\tau_A q)^2 + (\bar{q}i\gamma_5\tau_A q)^2] , \quad (2.35)$$

$$\begin{aligned} \mathcal{L}_d = H \sum_{A,B=2,5,7} & [(\bar{q}\tau_A\lambda_B C\bar{q}^t)(q^t C\tau_A\lambda_B q) \\ & + (\bar{q}i\gamma_5\tau_A\lambda_B C\bar{q}^t)(q^t C i\gamma_5\tau_A\lambda_B q)] , \end{aligned} \quad (2.36)$$

$$\mathcal{L}_{\text{KMT}} = -K \left[\det_f \bar{q}(1 + \gamma_5)q + \det_f \bar{q}(1 - \gamma_5)q \right] , \quad (2.37)$$

$$\mathcal{L}_{\text{vec}} = -g_V (\bar{q}\gamma^\mu q)(\bar{q}\gamma_\mu q) , \quad (2.38)$$

We use the external field \hat{A}^μ to introduce the chemical potentials by

$$\hat{A}^\mu = \delta_0^\mu (\mu_q + \mu_Q Q + \mu_3 \lambda_3 + \mu_8 \lambda_8) , \quad (2.39)$$

where $Q = \text{diag}(2/3, -1/3, -1/3)$ is a charge matrix in flavor space and λ_a are Gell-Mann matrices in color space. We chose the values of Hatsuda-Kunihiro parameters for coupling constants G and K , which successfully reproduce the hadron phenomenology at low energy [60, 62]: $G\Lambda^2 = 1.835$ and $K\Lambda^5 = 9.29$ with $\Lambda = 631.4$ MeV. The mean fields are introduced as

$$\sigma_f = \langle \bar{q}_f q_f \rangle , \quad (f = u, d, s) , \quad (2.40)$$

$$d_j = \langle q^t C \gamma_5 R_j q \rangle , \quad (j = 1, 2, 3) , \quad (2.41)$$

$$n_q = \sum_{f=u,d,s} \langle q_f^\dagger q_f \rangle , \quad (2.42)$$

where $(R_1, R_2, R_3) = (\tau_7\lambda_7, \tau_5\lambda_5, \tau_2\lambda_2)$. The thermodynamic potential for the quark matter with color-superconductivity is calculated as

$$\begin{aligned} \Omega_{\text{CSC}} = \Omega_s - \Omega_s[\sigma_f = \sigma_f^0, d_j = 0, \mu_q = 0] \\ + \Omega_c - \Omega_c[\sigma_f = \sigma_f^0, d_j = 0] , \end{aligned} \quad (2.43)$$

where

$$\Omega_s = -2 \sum_{i=1}^{18} \int_{\mathbf{p}} \frac{\varepsilon_i}{2} , \quad (2.44)$$

$$\Omega_c = \sum_i (2G\sigma_i^2 + H d_i^2) - 4K\sigma_u\sigma_d\sigma_s - g_V n_q^2 . \quad (2.45)$$

Using the following inverse propagator in Nambu-Gorkov basis, the energy eigenvalues ε_i in Eq. (2.44) can be obtained,

$$S^{-1}(k) = \begin{pmatrix} \gamma_\mu k^\mu - \hat{M} + \gamma^0 \hat{\mu} & \gamma_5 \sum_i \Delta_i R_i \\ -\gamma_5 \sum_i \Delta_i^* R_i & \gamma_\mu k^\mu - \hat{M} - \gamma^0 \hat{\mu} \end{pmatrix}, \quad (2.46)$$

where the effective masses (constituent quark mass)

$$M_i = m_i - 4G\sigma_i + K|\epsilon_{ijk}|\sigma_j\sigma_k \quad (i = u, d, s), \quad (2.47)$$

the pairing gap energies

$$\Delta_i = -2Hd_i \quad (i = 1, 2, 3), \quad (2.48)$$

and the effective chemical potential

$$\hat{\mu} = \mu_q - 2g_V n_q + \mu_Q Q + \mu_3 \lambda_3 + \mu_8 \lambda_8. \quad (2.49)$$

In the present parameter choice, at $n_B \gtrsim 5n_0$ they vary in the range of $M_{u,d} \approx 50\text{--}100$ MeV, $M_s \approx 250\text{--}300$ MeV and $\Delta_{1,2,3} \approx 200\text{--}250$ MeV [60]. The inverse propagator in Eq. (2.46) $S^{-1}(k)$ is 72×72 matrix in terms of the color, flavor, spin and Nambu-Gorkov basis, and therefore it has 72 eigenvalues. The matrix does not depend on the spin, and that the charge conjugation invariance relates two eigenvalues. Then, there are 18 independent eigenvalues at most.

The total thermodynamic potential is

$$\Omega_Q = \Omega_{\text{CSC}} + \sum_{l=e,\mu} \Omega_l, \quad (2.50)$$

where Ω_l is the thermodynamic potential for leptons given in Eq. (2.29). The chiral condensates σ_j and the diquark condensates d_i are determined from the gap equations,

$$0 = \frac{\partial \Omega_Q}{\partial \sigma_i} = \frac{\partial \Omega_Q}{\partial d_i}. \quad (2.51)$$

The chemical potentials μ_j ($j = Q, 3, 8$) are determined by imposing the beta equilibrium condition given in Eq. (2.31) and the charge neutrality conditions for electromagnetic and color charges as

$$0 = n_j = -\frac{\partial \Omega_Q}{\partial \mu_j}. \quad (2.52)$$

The baryon number density n_B is three times of Quark number density is determined as

$$n_q = -\frac{\partial\Omega_Q}{\partial\mu_q} , \quad (2.53)$$

and the baryon number density is $n_B = n_q/3$, which means that one baryon has three constituent quarks. On the other hand, the chemical potentials for baryon number and quark number have a relation: $\mu_B = 3\mu_q$. Finally, the pressure in the quark matter is obtained as

$$P_Q = -\Omega_Q . \quad (2.54)$$

2.2.2 Interpolating EOSs

We construct the unified EOS by interpolating two EOSs for quark matter and hadronic matter, which are introduced in the previous sections. The effective region for each models are determined based on Ref. [60]. In the low density region $n_B < 2n_0$, the hadronic matter is realized and we use the pressure P_H in Eq. (2.32). While the quark matter is valid in the high density region $n_B > 5n_0$, and we use the pressure P_Q in Eq. (2.54). In the intermediate region from $2n_0$ to $5n_0$, we use the pressure P_1 , which is the following polynomial in terms of baryon chemical potential with six coefficients a_n to interpolate above two EOSs,

$$P_1(\mu_B) = \sum_{n=0}^5 a_n \mu_B^n . \quad (2.55)$$

The following boundary conditions determine the six free parameters a_n ,

$$\begin{aligned} \left. \frac{d^n P_1}{(d\mu_B)^n} \right|_{\mu_{BL}} &= \left. \frac{d^n P_H}{(d\mu_B)^n} \right|_{\mu_{BL}} , \\ \left. \frac{d^n P_1}{(d\mu_B)^n} \right|_{\mu_{BU}} &= \left. \frac{d^n P_Q}{(d\mu_B)^n} \right|_{\mu_{BU}} , \quad (n = 0, 1, 2) \end{aligned} \quad (2.56)$$

where μ_{BL} is the chemical potential corresponding to $n_B = 2n_0$ and μ_{BU} to $n_B = 5n_0$.

Fig. 2.1 shows the typical examples of the interpolated EOS and Fig. 2.2 shows corresponding sound velocity calculated by

$$c_s^2 = \frac{dP}{d\varepsilon} = \frac{n_B}{\mu_B \chi_B} , \quad (2.57)$$

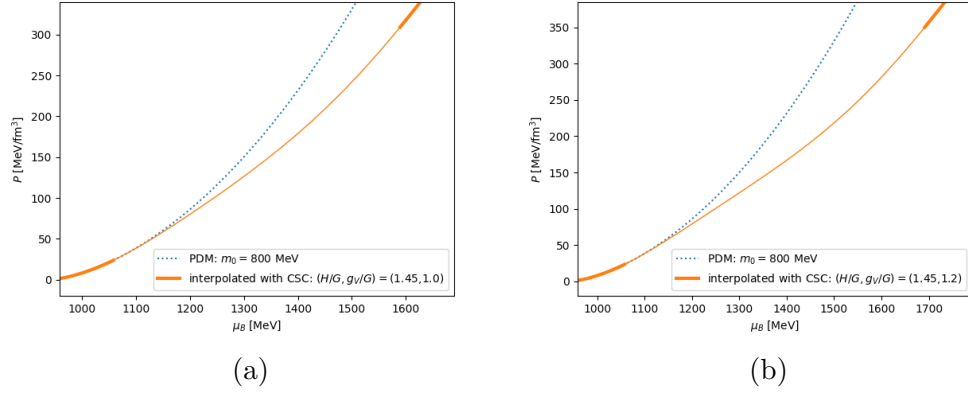


Figure 2.1: Pressure vs. baryon chemical potential, for the PDM and for one interpolating to the CSC. The solid thin curve corresponds to the interpolation from the hadronic matter to the quark matter.

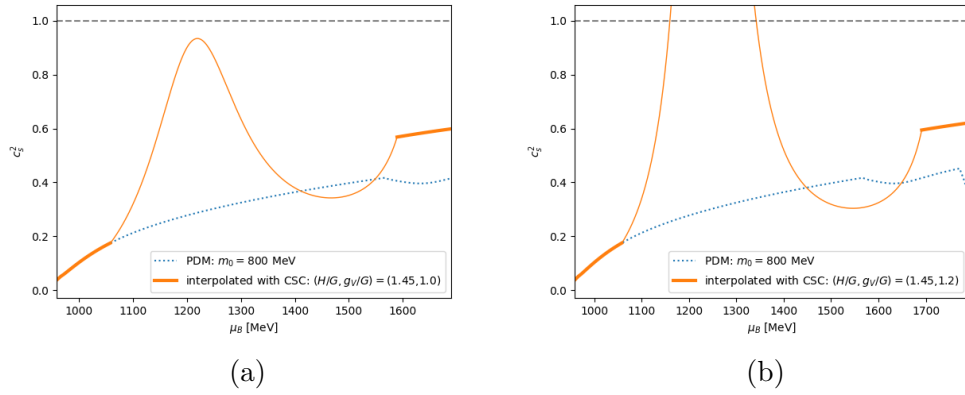


Figure 2.2: Squared speed of sound c_s^2 .

where the baryon number density $n_B = \frac{dP}{d\mu_B}$ and the baryon number susceptibility $\chi_B = \frac{d^2P}{d\mu_B^2}$. We see that, although both plots 2.1(a) and 2.1(b) in Fig. 2.1 are smooth, Fig. 2.2 shows that the parameter set (b) violates causality. Therefore, when $m_0 = 800$ MeV, the parameter choice $(H/G, g_V/G) = (1.45, 1.2)$ is excluded.

Figure 2.3 shows the parameter regions (H, g_V) satisfying the causality condition for several choices of m_0 . To see this, there are a positive correlation for the values of H and g_V in all cases. This means that we need to increase the value of H for a larger g_V [61]. The details of this positive correlation depend on the low density constraint and the choice of m_0 . As we can see from Table.2.2, the low density EOS softens for a large m_0 , and correspondingly

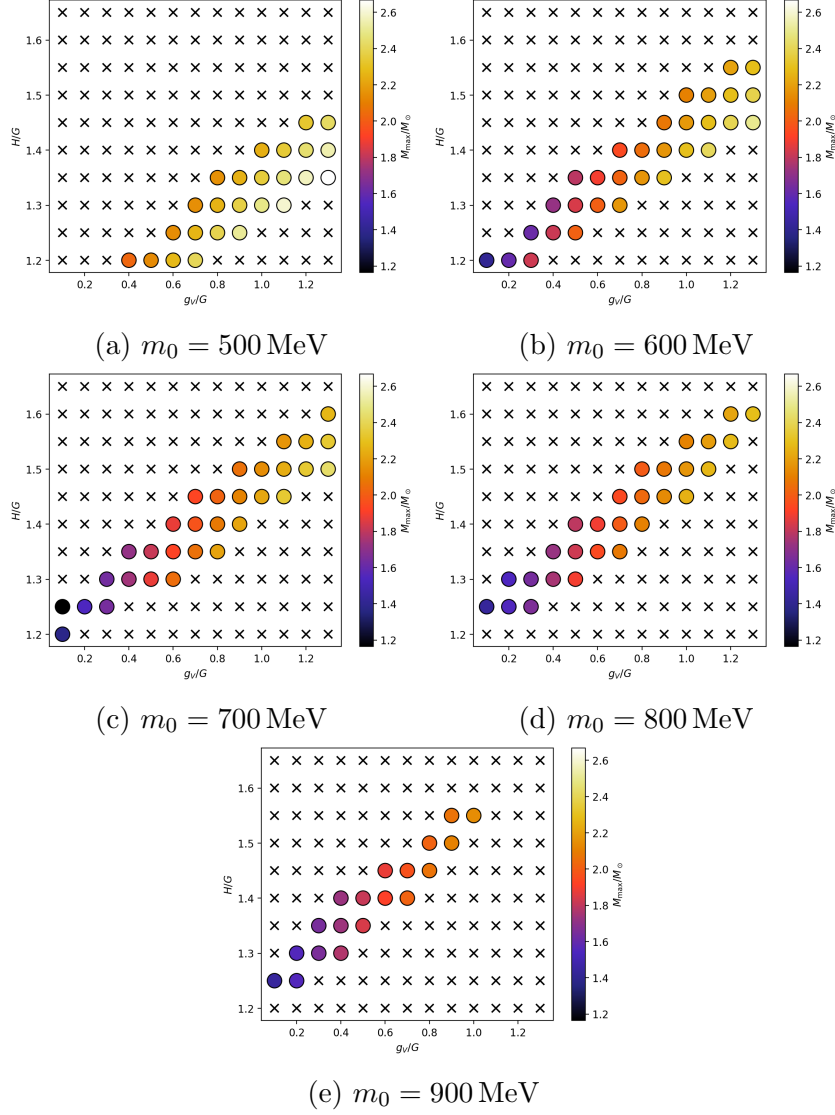


Figure 2.3: Allowed combinations of (H, g_V) for $m_0 = 500$ – 900 MeV. Cross marks \times are not causal, while the colored circles are causal. The color of the circle shows the corresponding maximum mass of neutron stars.

smaller values of g_V are favored for causal interpolations. We note that the range of (H, g_V) is larger than the previously used estimates, $(H/G, g_V/G) = (0.5, 0.5)$, based on the Fierz transformation (see e.g. Ref. [90]). Such choices were used in the hybrid quark-hadron matter EOS with first order phase transitions, and tend to lead to the neutron star mass smaller than $2M_\odot$.

2.3 Numerical results

In this section, we calculate mass-radius relations of neutron stars using the Tolman-Oppenheimer-Volkoff (TOV) equation [91, 92]. The TOV equation for hydrostatic equilibrium in general relativity is given by

$$\begin{aligned}\frac{dP}{dr} &= -G \frac{(\varepsilon + P)(m + 4\pi r^3 P)}{r^2 - 2Gmr}, \\ \frac{dm}{dr} &= 4\pi r^2 \varepsilon,\end{aligned}\tag{2.58}$$

where r is the radial coordinate of a neutron star and G is the constant of gravitation. $P(r)$ is pressure on the shell with radius r , m is the total mass of the shell. The energy density ε is determined by EOS.

For the core of neutron stars, we use the EOS which is build in the previous sections. For the crust of neutron stars, we include the BPS EOS [93]¹ at $n_B \leq 0.1 \text{ fm}^{-3}$, and at $n_B \geq 0.1 \text{ fm}^{-3}$ we use our unified EOS from nuclear liquid to quark matter.

A static-spherical neutron star is determined by the central density n_c , or equivalently the central pressure P_c , as the initial values of the TOV equation: $P(0) = P_c$ and $m(0) = 0$. Imposing the condition that pressure will vanish at the boundary of the neutron star $P(R)=0$, the neutron star radius R is determined. The neutron star mass is also determined as $M = m(R)$. Since the mass M and radius R are uniquely determined by the central density n_c , the mass-radius curve is the graph which is parametrized by the central density $(M(n_c), R(n_c))$.

Figures 2.4 and 2.5 show the mass-radius and mass-central density curves, which are calculated from our EOSs. In each panel of Figs. 2.4 and 2.5, the different combinations of (H, g_V) are corresponding to the different curves, which parameters are corresponding to the allowed parameters indicated by circles in Fig. 2.3. The thin curves are corresponding to the central densities are in crossover domain: $2n_0 < n_c < 5n_0$. Therefore, the neutron stars in the thick curves in the low-mass region consist of only hadronic matter, while the ones in the thick lines in the high-mass region contain quark matter.

The maximum mass of a neutron star is determined for each combination of (H, g_V) , and the resulting values are represented by the color in Fig. 2.3.

¹The BPS EOS is usually referred as EOS for the outer crust, but it also contains the BPP EOS [93] for the inner crust.

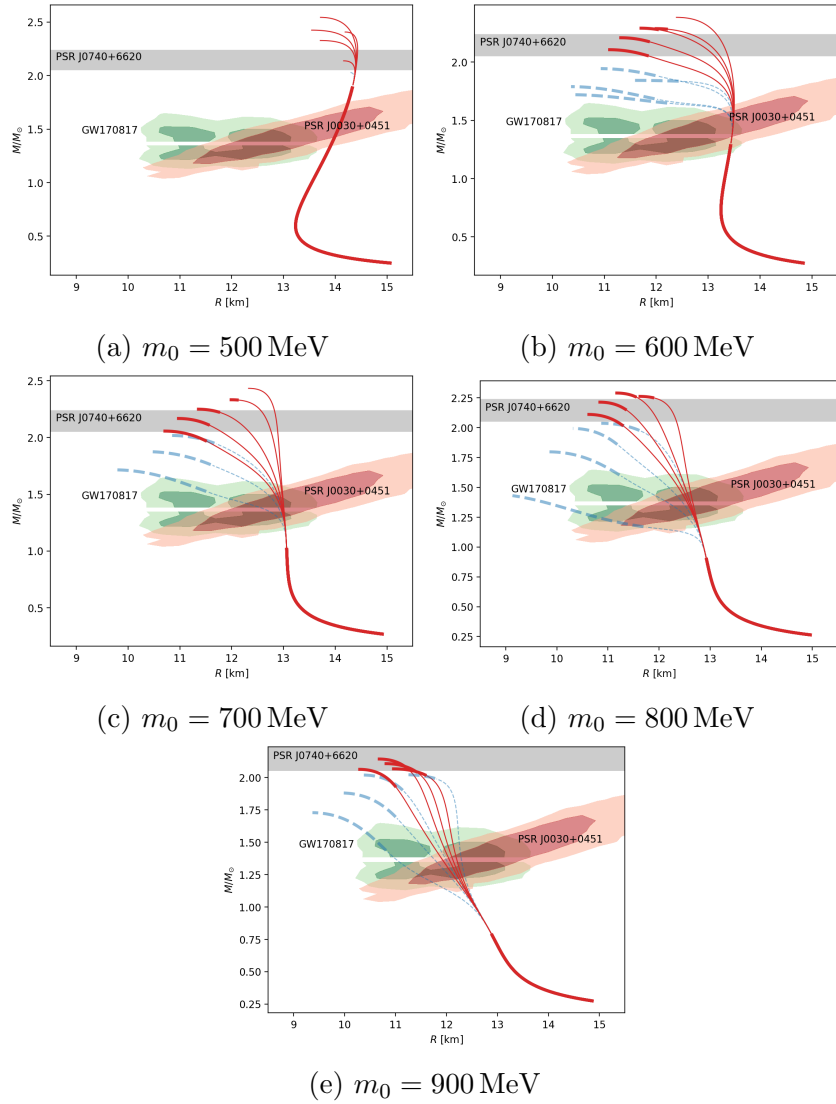


Figure 2.4: Several choices of mass-radius relations for each m_0 . (See main texts for detail.)

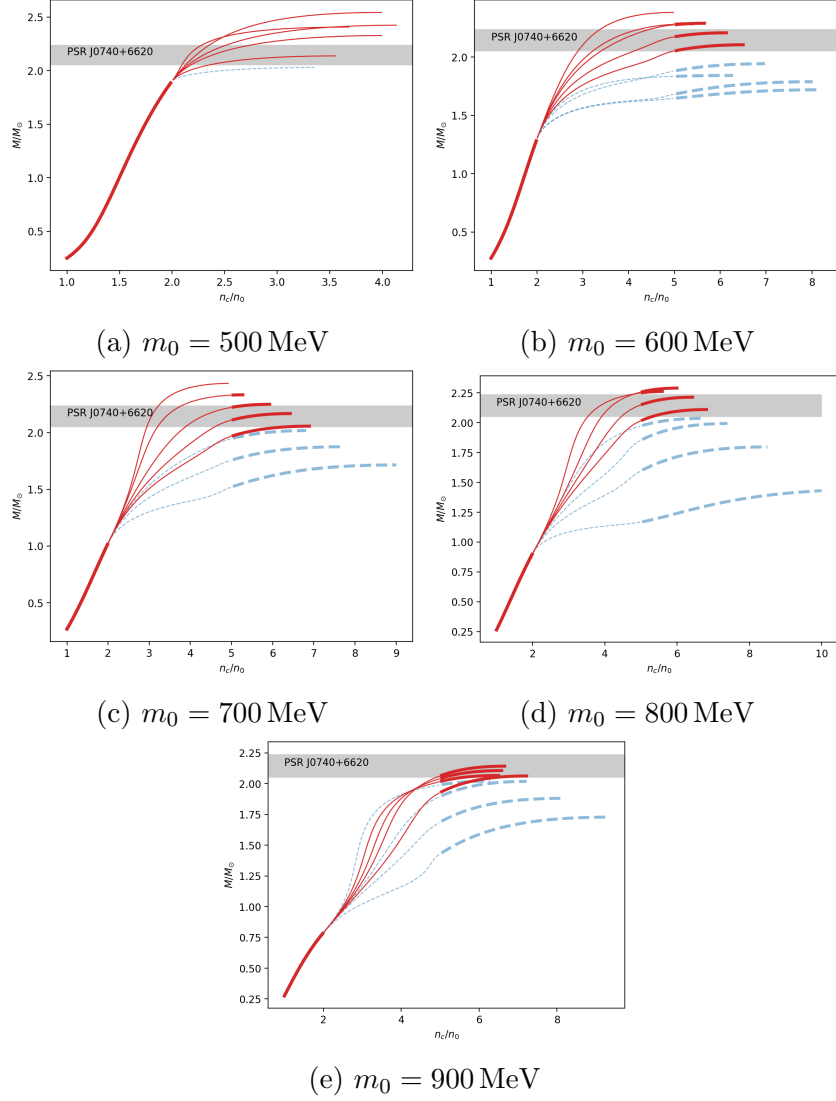


Figure 2.5: Several choices of relations between mass and central density for each m_0 . (See main texts for detail.)

Table 2.3: Radius constraints for neutron stars.

	radius [km]	mass [M_\odot]
GW170817 (primary)	$11.9^{+1.4}_{-1.4}$	$1.46^{+0.12}_{-0.10}$
GW170817 (secondary)	$11.9^{+1.4}_{-1.4}$	$1.27^{+0.09}_{-0.09}$
J0030+0451 (NICER [21])	$13.02^{+1.24}_{-1.06}$	$1.44^{+0.15}_{-0.14}$
J0030+0451 (NICER [22])	$12.71^{+1.14}_{-1.19}$	$1.34^{+0.15}_{-0.16}$

The figure clearly demonstrates that a decrease in H or an increase in g_V corresponds to an increase in the maximum mass.

In this thesis, we adopt the mass of PSR J0740+6620, a millisecond pulsar, as the lowest maximum mass. The mass value is $2.14^{+0.10}_{-0.09} M_\odot$, and it is represented by a gray-shaded area in Figs. 2.4 and 2.5. The red solid curves in these figures correspond to the mass-radius relations for which the maximum mass is greater than the lowest maximum mass, while the blue dashed curves indicate the maximum masses that do not exceed the lowest maximum mass. We also depict the constraint on the radius obtained from LIGO-Virgo and NICER observations ². The green shaded areas on the middle left and the red shaded areas on the middle right represent the constraints from LIGO-Virgo and NICER (Miller et al. [21]), respectively. The inner contour of each shaded area contains 68% of the posterior probability (1σ), and the outer contour contains 95% (2σ). The summary of these values, including another NICER result of Riley et al. [22], is provided in Table 2.3.

LIGO-Virgo has estimated the radius of a neutron star with $\simeq 1.4M_\odot$ to be 11.9 ± 1.4 km³. If we only require our M - R curves to fall within the 2σ band, we obtain the constraint $m_0 \gtrsim 600$ MeV, regardless of the quark EOS. If we further demand that the M - R curves fall within the 1σ band, we find that only a few curves with $m_0 \geq 700$ MeV satisfy this requirement, but they

²More precisely, the LIGO-Virgo constrains the tidal deformability $\tilde{\Lambda}$ which is the function of the tidal deformability of each neutron star (Λ_1 and Λ_2) and the mass ratio $q = M_2/M_1$. But for EOS which do not lead to large variation of radii for $M \gtrsim 1M_\odot$, $\tilde{\Lambda}$ is insensitive to q . In fact the radii of neutron stars and $\tilde{\Lambda}$ can be strongly correlated (for more details, see Ref. [94, 95]), and for our purposes it is sufficient to directly use the estimates on the radii given in Ref. [19], rather than $\tilde{\Lambda}$.

³LIGO-Virgo also provides another estimation with the range of 9–13 km. For our model, we can obtain the same result for the m_0 constraint from both estimations.

do not satisfy the $2M_\odot$ constraint and must be rejected. On the other hand, it is easier to reconcile our modeling with the NICER constraints, which suggest larger radii. The range $500 \text{ MeV} \leq m_0 \leq 900 \text{ MeV}$ falls within the 1σ band and hence does not impose additional constraints beyond those of LIGO-Virgo. Using all of the above observational data, the 2σ range of the LIGO-Virgo data provides the following constraints on the chiral invariant mass:

$$600 \text{ MeV} \lesssim m_0 \lesssim 900 \text{ MeV}. \quad (2.59)$$

Note that if the chiral invariant mass m_0 is larger, the corresponding slope parameter is smaller, $80.08 \text{ MeV} \lesssim L_0 \lesssim 86.24 \text{ MeV}$, as can be seen from Table 2.2, which is in agreement with experimental data.

2.4 Summary and discussions of Ch.2

Our approach to constructing the EOS for neutron star matter involves interpolating between the EOS obtained in the PDM and the one in the NJL-type model. To ensure that the resulting EOS is physically meaningful, we impose constraints on the model parameters based on thermodynamic stability and causality, as well as the constraints imposed by the M - R curves.

Our main objective was to investigate how observations of neutron stars constrain the microphysics and hadronic EOS. While our hadronic EOS accurately represents the physics at the saturation density, its extrapolation towards higher densities is influenced by the chiral invariant mass m_0 . The radii of $1.4 M_\odot$ neutron stars are highly correlated with the stiffness of the low-density EOS beyond the saturation density ($n_B = 1-2n_0$), and we have established a significant constraint, $600 \lesssim m_0, [\text{MeV}] \lesssim 900$. At low densities, the density dependence of the stiffness is determined by the balance between σ - and ω -exchanges, with the former's strength being highly dependent on the fraction of the chiral variant component in the nucleon mass.

The maximum mass of neutron stars is highly correlated with the high density EOS, and it puts constraints on the parameters of the quark model, such as (H, g_V) . However, these parameters are not independent of the hadronic sector, as the high and low density EOS must have a causal and thermodynamically stable connection. The range of allowed values for (H, g_V) is sensitive to our choice of m_0 or the stiffness of the hadronic EOS. Soft hadronic EOS that are associated with large m_0 exhibit greater tensions with

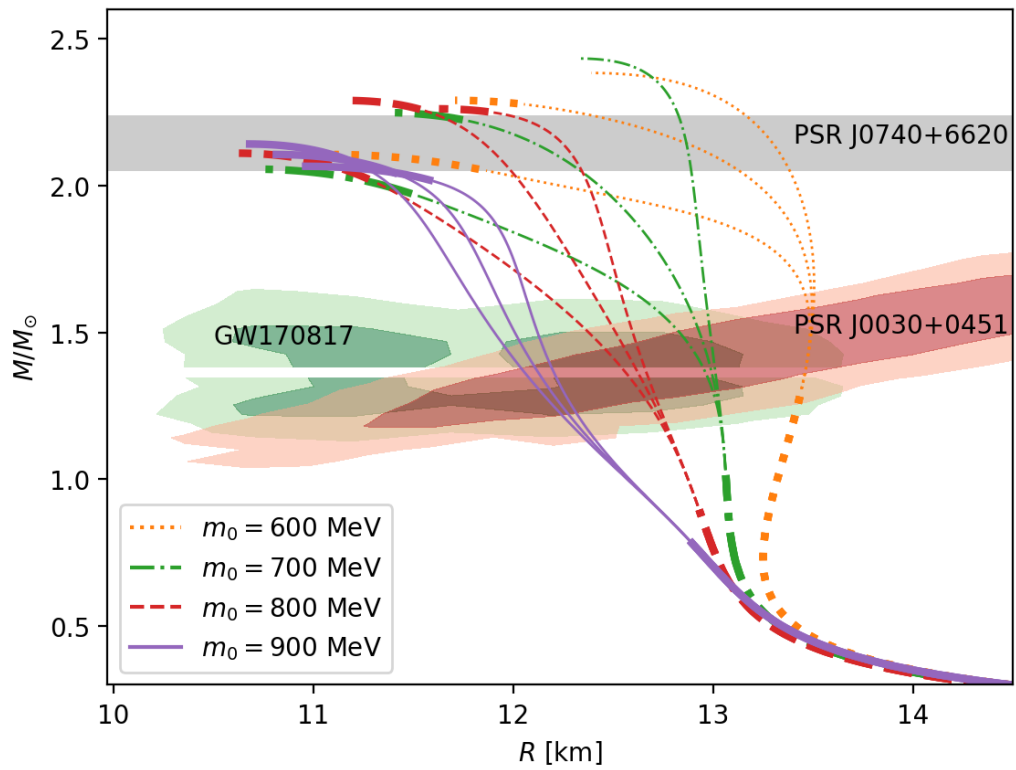


Figure 2.6: Several choices of mass-radius relations which satisfy both the maximum mass and the radius constraints.

sufficiently stiff quark EOS, thereby setting an upper bound of $m_0 \lesssim 900$ MeV. This upper bound is in close proximity to the total nucleon mass of $m_N \approx 939$ MeV, and therefore, it is not as noteworthy as the radius constraint.

We would like to draw attention to the fact that the cores of heavy neutron stars with masses around $2M_\odot$ include quark matter, as illustrated by the thick curves in the heavy-mass region of Fig. 2.6. Conversely, the core of the neutron star with a mass of $1.4M_\odot$ falls within the crossover domain of quark and hadronic matter. Therefore, in our crossover construction of a unified EOS, variations in the radii of the $1.4M_\odot$ neutron star are relatively small, with $\Delta R \lesssim 0.5$ km.

For this analysis, we have assumed a crossover between hadronic matter and quark matter. Our findings, as illustrated in Fig 2.3, suggest that the coupling parameter H must be sufficiently large to ensure a smooth connection and satisfy causality, as noted in Ref. [60]. In particular, H values greater than or equal to $1.4G$ are necessary, which is consistent with the N - Δ splitting [96] and leads to the CFL phase for densities n_B greater than or equal to $5n_0$.

It is worth noting that previous studies, such as Ref. [60], primarily relied on the constraint $R \lesssim 13$ km from GW170817. However, new NICER results have emerged that suggest radii of approximately 13 km, allowing for a relaxation of the condition on low density EOS and the inclusion of stiffer EOS. This broadens the possibility of first order phase transitions. In this context, it would be interesting to explicitly incorporate the first order transition in the interpolated domain, as in Refs. [50, 52], while utilizing quark and hadronic EOS as boundary conditions.

The slope parameter L_0 predicted values, ranging from 80 to 94 MeV, which are presented in Table 2.2, exceed the typical estimates of L_0 , which typically fall between 30 and 90 MeV. References such as [67–69] support these typical estimates. However, recent analyses of PREXII for the neutron skin thickness suggest that L_0 is around (109.56 ± 36.41) MeV, and it is not clear which estimates are more accurate. While the current study primarily focuses on the variation of m_0 , it is also possible to adjust the value of L_0 by including a term proportional to $\omega^2 \rho^2$ in the hadronic part. This adjustment could slightly alter the lower and/or upper bounds of m_0 in Eq. (2.59). Future studies will explore these extensions of the PDM model.

Chapter 3

Chiral Condensate in Crossover

The content of this chapter is based on our paper [2].

In this chapter, we also write the integrals over space as, $\int_x = \int d^4x$, $\int_{\mathbf{x}} = \int d^3\mathbf{x}$, and over momentum as, $\int_{\mathbf{p}} = \int \frac{d^3\mathbf{p}}{(2\pi)^3}$.

3.1 Nuclear matter

3.1.1 Chiral condensate in the PDM

One can compute the chiral condensate in effective models by taking the derivative of the thermodynamic potential with respect to the current quark mass. In our model, the term $-m_\pi^2 f_\pi \sigma$ represents explicit chiral symmetry breaking, while we have ignored higher order terms of current quark mass perturbations. These couplings are expected to take the form of $\sim (\varphi/M_q)^n$, with the effective quark mass $M_q \simeq 300$ MeV obtained from quark integration. As a result, we anticipate that these couplings will mainly depend on length scales shorter than those associated with pions, and thus, the current quark mass should be a small perturbation in powers of $\sim (m_q/M_q)^n$. The Gell-Mann–Oakes–Renner relation rewrites the explicit symmetry breaking term as

$$\Omega_{\text{ESB}} = -m_\pi^2 f_\pi \sigma = m_q \langle \bar{u}u + \bar{d}d \rangle_0 \frac{\sigma}{f_\pi}. \quad (3.1)$$

$m_q = (m_u + m_d)/2$ is the mean value of up- and down- quark current masses. The chiral condensate in vacuum is written as $\langle \bar{u}u + \bar{d}d \rangle_0$. Using this equation, the chiral condensate in medium can be defined by differentiating the

thermodynamic potential as

$$\langle \bar{u}u + \bar{d}d \rangle \equiv \frac{\partial \Omega_{\text{ESB}}}{\partial m_q} = \langle \bar{u}u + \bar{d}d \rangle_0 \frac{\sigma}{f_\pi}, \quad (3.2)$$

Here m_q dependence of $\langle (\bar{u}u + \bar{d}d) \rangle_0$ which is higher orders in m_q/M_q is neglected. We focus on σ instead of $\langle \bar{q}q \rangle$, below.

3.1.2 Chiral scalar density in a nucleon

The scalar charge in a nucleon, N_σ , is useful to estimate the in-medium chiral condensates. The nucleon mass in vacuum is related to the nucleon's scalar charge as

$$\begin{aligned} N_\sigma &= \int_{\mathbf{x}} \langle N | \bar{u}u + \bar{d}d | N \rangle \\ &= \langle N | \frac{\partial H_{\text{QCD}}}{\partial m_q} | N \rangle = \frac{\partial m_N^{\text{vac}}}{\partial m_q}, \end{aligned} \quad (3.3)$$

where H_{QCD} is the QCD Hamiltonian, and the Hellmann–Feynman theorem [97] is used in the last step.

The current quark mass dependence of the nucleon mass in the PDM is only through of σ , so we calculate the scalar charge at vacuum as

$$N_\sigma = \frac{\partial m_N^{\text{vac}}}{\partial m_q} = \frac{\partial \sigma^{\text{vac}}}{\partial m_q} \left(\frac{\partial m_N}{\partial \sigma} \right)_{\sigma=\sigma^{\text{vac}}}. \quad (3.4)$$

When we calculate the variation of σ^{vac} , we prepare the thermodynamic potentials at various m_q , calculate σ^{vac} for each potential, and evaluate the impact of the mass variation on σ^{vac} . The mass derivative of σ^{vac} is proportional to the static correlator¹ $\sim \langle (\sigma - \langle \sigma \rangle)^2 \rangle \sim m_\sigma^{-2}$, so is bigger for a smaller scalar meson mass.

¹The mass derivative of the quark condensate is related to the (connected) scalar correlator at zero momentum,

$$\begin{aligned} \frac{\partial \langle \bar{q}q \rangle}{\partial m_q} &\sim \int \mathcal{D}q \mathcal{D}\bar{q} [\bar{q}q(x)] \frac{\partial}{\partial m_q} \left(e^{-\int_{x'} m_q \bar{q}q(x') + \dots} / Z \right) \\ &\sim \int_{x'} \langle [\bar{q}q(x)] [\bar{q}q(x')] \rangle_{\text{conn.}} \sim \lim_{q \rightarrow 0} \frac{1}{q^2 + m_\sigma^2}. \end{aligned} \quad (3.5)$$

Table 3.1: Some values of the PDM in vacuum.

m_0 [MeV]	500	600	700	800	900
$(\partial m_N / \partial \sigma)_{\text{vac.}}$	7.97	7.01	5.87	4.56	3.07
m_σ [MeV]	396	414	388	332	271
Σ_N [MeV]	91.9	74.0	70.5	74.6	75.7

The so-called nucleon sigma term Σ_N can be defined as

$$\Sigma_N = m_q N_\sigma = \int_{\mathbf{x}} \langle N | m_q (\bar{u}u + \bar{d}d) | N \rangle. \quad (3.6)$$

The quantity $m_q(\bar{u}u + \bar{d}d)$ is known as a renormalization group invariant one. As the scalar density is more directly related to the experimental quantities, it is often discussed in this form. The traditional estimate [98] is $\Sigma_N \simeq 45$ MeV (which includes up- plus down-quark contributions), but currently the estimates based on lattice QCD or combined analyses of the lattice QCD and the chiral perturbation theory range over 40–70 MeV [97]. Using the values $N_\sigma \simeq 8$ –14 and $m_q \simeq 5$ MeV, the scalar density can be evaluated as

$$\frac{N_\sigma}{\frac{4}{3}\pi R_N^3} = \left(0.24\text{--}0.30 \text{ GeV} \times \frac{1 \text{ fm}}{R_N} \right)^3, \quad (3.7)$$

where the size of nucleon is written as $R_N (\sim 1 \text{ fm})$. The vacuum scalar density is roughly equal order of magnitude as the mean value of the nucleon scalar charge, but the opposite sign. In Table 3.1, the values in the PDM for various m_0 are listed for comparison.

We observe that our calculated value of m_σ lies in the range of 270–410 MeV, which is smaller than the mass of the scalar meson $f_0(500)$ ², which has a width of approximately 500 MeV. Additionally, the value of Σ_N in our model is larger than the conventional value of around 45 MeV. It is worth noting that Σ_N is proportional to $\partial\sigma^{\text{vac}}/m_q$, which in turn is proportional to m_σ^{-2} . To achieve better agreement with empirical values, it may be necessary to increase m_σ . This could be accomplished, for instance, by introducing higher-order polynomials of σ fields to alter the curvature of the effective potential. Such fine-tuning, however, is beyond the scope of this thesis, and

²Whether σ in mean field models should be interpreted as the physical scalar meson is not a simple matter.

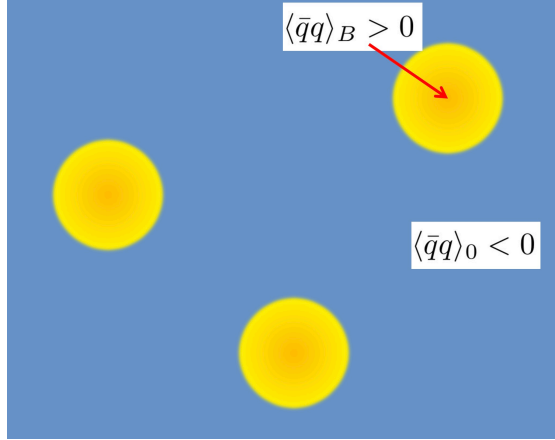


Figure 3.1: Chiral condensates in dilute regime. The region dominated by the vacuum chiral condensate has the negative scalar charge while in nucleons the scalar charges are positive.

we continue to use the parameter set employed in Chapter 2. Nonetheless, we believe that the present model can still be used to investigate the overall qualitative trends of chiral restoration.

The relationship $N_\sigma = \partial m_N^{\text{vac}} / \partial m_q$ implies that the scalar charge of the nucleon should be positive, as an increase in the current quark masses is expected to cause an increase in the nucleon mass. Given that the chiral condensate in vacuum is negative, the scalar charges of the nucleon tend to counterbalance the vacuum chiral condensate.

3.1.3 Dilute regime

In the dilute regime (see Fig.3.1) we can make a solid statement; here nucleons are widely separated, so the scalar density in medium is estimated by simply adding the scalar charges of nucleons to the vacuum condensate, and then taking the spatial average, i.e.,

$$\langle \bar{u}u + \bar{d}d \rangle \simeq \langle \bar{u}u + \bar{d}d \rangle_0 + n_B N_\sigma, \quad (3.8)$$

or equivalently one can write

$$\sigma \simeq f_\pi \left(1 + \frac{n_B N_\sigma}{\langle \bar{u}u + \bar{d}d \rangle_0} \right). \quad (3.9)$$

This is the famous linear density approximation, which implies that the value of σ decreases as n_B increases.

The violation of this approximation signals the end of the dilute regime. Figure 3.2 shows the ratio of the quark condensate, $\langle \bar{u}u \rangle / \langle \bar{u}u \rangle_0 = \sigma / f_\pi$, versus the neutron number density n_n in pure neutron matter and compare it with the linear density approximation. Our mean field results have milder chiral restoration than in the linear density approximation. Similar trends have been found in the analyses based on the chiral effective theories including the fluctuations of pions [99–101]

We want to emphasize that the chiral restoration described in this paper does not necessarily have an immediate effect on the properties of baryons or the Dirac sea, in light of the PDM. Our no sea approximation for the thermodynamic potential for nucleons (see Eq. (2.26)) and the modest changes in nucleon mass in the PDM support this. Additionally, we note that during a high-temperature transition from a hadron resonance gas (HRG) to a quark gluon plasma (QGP), chiral condensates decrease significantly just below the transition temperature. However, at this temperature, the HRG model with *vacuum* hadron masses still accurately describes the lattice data, as reported in [102, 103]. We will revisit this point when discussing chiral restoration in quark matter, where changes in the Dirac sea are more likely to occur.

3.1.4 Strange quark condensate

The density increase in the nucleus has an impact on the strange quark condensate, given that nucleons contain sea strange quarks. The strangeness sigma-term can be utilized to approximate the prevalence of sea strange quarks within a nucleon,

$$\Sigma_{sN} = m_s \frac{\partial m_N}{\partial m_s} = \int_{\mathbf{x}} \langle N | m_s \bar{s}s | N \rangle = m_s N_s. \quad (3.10)$$

Our PDM does not manifestly include the strangeness so that we simply substitute the vacuum value for the linear density approximation,

$$\langle \bar{s}s \rangle \simeq \langle \bar{s}s \rangle_0 + n_B N_s. \quad (3.11)$$

This estimate will be used when we consider the interpolation between nuclear and quark matter.

There are several errors in our estimation of the strange quark condensate, even in the dilute regime. This is because determining the strangeness

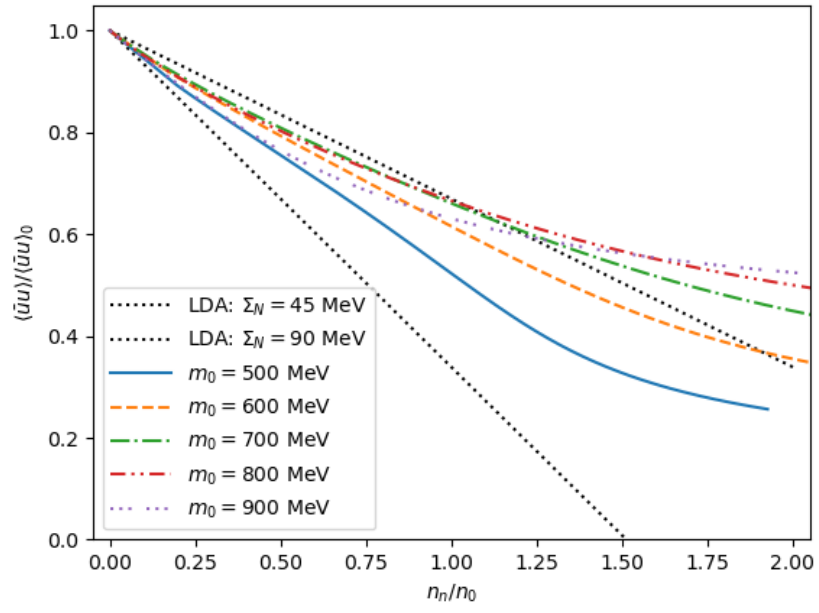


Figure 3.2: Ratio of the quark condensate in the PDM $\langle \bar{u}u \rangle / \langle \bar{u}u \rangle_0 = \sigma / f_\pi$ versus the neutron number density n_n .

content in a nucleon is challenging due to its small effect that is unrelated to the valence quarks. Estimates from lattice QCD suggest a range of values for the strangeness sigma-term, from approximately 17 MeV to 42 MeV. Assuming $m_s \simeq 100$ MeV, we estimate $N_s \simeq 0.2$ – 0.4 , which corresponds to approximately 0.01–0.05 times N_σ .

The positivity of strangeness sigma-term found on the lattice implies that $\partial m_N / \partial m_s$ is positive. This is by no means trivial, as strange quarks are not valence quarks in a nucleon, and increasing strange quark does not readily increase the valence quark mass nor the nucleon mass. One possible way to express $\partial m_N / \partial m_s > 0$ is to assume the validity of the expression as in Eq.(3.4),

$$N_s = \frac{\partial m_N^{\text{vac}}}{\partial m_s} \simeq \frac{\partial \sigma^{\text{vac}}}{\partial m_s} \left(\frac{\partial m_N}{\partial \sigma} \right)_{\sigma=\sigma_{\text{vac}}}, \quad (3.12)$$

and to consider the Kobayashi–Maskawa–’tHooft term for the $U(1)_A$ anomaly,

$$\mathcal{L}_{\text{KMT}} \sim C(\bar{u}u)(\bar{d}d)(\bar{s}s) + \dots, \quad (3.13)$$

where we wrote only the product of scalar densities. A larger strange quark more explicitly breaks the chiral symmetry and hence enhances the size of strange quark condensate in vacuum. Within mean field treatments (as in the NJL model), a larger strange condensate contributes to the term like

$$\mathcal{L}_{\text{KMT}} \sim C\langle\bar{s}s\rangle_0[\langle\bar{d}d\rangle_0 \times \bar{u}u + \langle\bar{u}u\rangle_0 \times \bar{d}d] + \dots, \quad (3.14)$$

which, for $C < 0$, assists the chiral symmetry breaking and increases the effective quark masses for up- and down-quarks. These relations suggest that a larger m_s firstly enhances $\langle\bar{s}s\rangle_0$, and then the effective masses of up- and down-quarks through the anomaly term. Within this description, m_N or σ_{vac} increases for a larger m_s , and hence $N_s > 0$ follows.

3.2 Quark matter (CFL phase)

3.2.1 Overall picture

We utilize the NJL model to describe quark matter. Although the model does not account for confinement, it can explain hadron phenomenology with low sensitivity to confining effects [62], such as the low energy constants for

a hadronic effective Lagrangian for energies $\lesssim 1$ GeV. The NJL model is designed to capture physics at semi-hard scales, $0.2 \text{ GeV} \lesssim p \lesssim 1 \text{ GeV}$, which is the scale between confinement and chiral symmetry breaking [104, 105]. These quark models can describe the physics within a hadron, about ~ 1 fm in terms of distance scale, but do not resolve the partonic structure of constituent quarks [106]. We anticipate that NJL-type constituent quark models will provide reasonable descriptions of bulk quantities at densities where baryons begin to overlap.

Our NJL model incorporates the vector repulsion and diquark attraction, in addition to the standard NJL model [62]. These additional interactions are necessary to explain the successful hadron description, which requires proper constituent quark masses and color interactions at semi-hard scale. For instance, the color magnetic interactions are essential to account for the level splitting seen in N - Δ or π - ρ [107]. In our diquark terms, we attempt to include the attractive part of such interactions, which lead to diquark condensation at high densities and, in the three-flavor model, color-flavor-locked (CFL) pairing. The magnetic interactions in repulsive channels can also be used to explain the channel dependence in baryon-baryon interactions at short distances [108, 109], such as hard-core repulsion between nucleons. Our vector repulsion can be viewed as a parameterization of such short-distance repulsion.

Even though the vector and diquark interactions have opposite signs, their effects do not cancel out because they have different density dependences. The vector repulsion affects the entire bulk of the quark Fermi sea, contributing to an energy density of $\varepsilon_{\text{vector}} \sim +n_B^2$, whereas the diquark attraction mainly affects quarks near the Fermi surface, contributing to an energy density of $\varepsilon_{\text{diquark}} \sim -\Delta^2 n_B^{2/3}$. Both contributions can lead to stiffer equations of state [82].

3.2.2 Chiral condensates in the CFL quark matter

In the context of quark matter, the formation of chiral condensates is impeded by the quark Fermi sea. This is because the presence of an antiquark requires energy on the order of the quark Fermi energy, and its creation involves moving a particle in the Dirac sea beyond the Fermi surface to avoid Pauli blocking. As a result, at higher densities, chiral condensates are naturally broken apart. In contrast, particle-particle or particle-hole pairings are preferred since they only involve degrees of freedom near the Fermi surface.

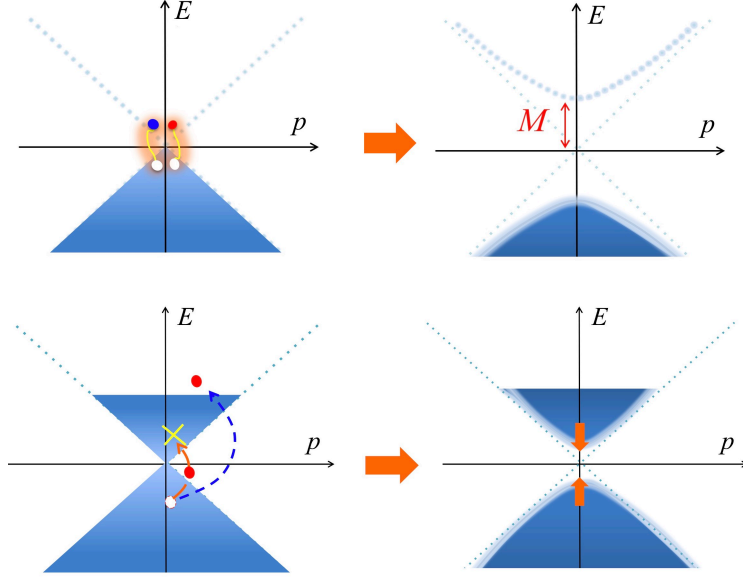


Figure 3.3: Chiral symmetry breaking by condensation of quark-antiquark pairs; (upper) in vacuum; (lower) in medium. In the latter the pairing is blocked by the quark Fermi sea.

It is worth noting that the chiral restoration discussed in quark matter is different from what we have observed in dilute nuclear matter. In the latter case, chiral restoration occurs due to the balance between positive and negative charges. However, in quark matter, both the positive and negative scalar charges decrease as density increases, leading to changes in both the Dirac sea and the constituent quark masses. This is in contrast to dilute nuclear matter, where the sum of the scalar charges changes but not the individual charges. In the PDM context, the modification of the Dirac sea is likely responsible for the reduction of the chiral invariant mass m_0 .

3.3 Condensates in a unified EOS

In the previous sections, we calculated the condensates for the nuclear and quark models. In this section, by interpolating them, unified condensates are constructed. Especially, the chiral condensates, the diquark condensates, and the particle number fractions for (u, d, s) -quarks and leptons (electrons and muons) are computed.

3.3.1 Unified generating functional

First, we extend the interpolating polynomial $P(\mu_B)$ to a generating functional $P(\mu_B; J)$, where J is the external field coupled to the condensate ϕ . One can obtain the condensate ϕ by partial differentiating the functional with respect to J with fixed μ_B as

$$\phi = - \left. \frac{\partial P}{\partial J} \right|_{J=0}. \quad (3.15)$$

In low density region, $n_B \leq 2n_0$, the generating functional is given by the PDM, and in high density region, $n_B \geq 5n_0$, given by the NJL model. In intermediate region, imposing the continuity conditions up to the second derivatives at the boundaries, $n_B = 2n_0$ and $5n_0$, these functionals are interpolated. The following polynomial function is used for an interpolating function,

$$P_I(\mu_B; J) = \sum_{n=0}^5 a_n(J) \mu_B^n, \quad (3.16)$$

where $a_n(J)$ ($n = 0, \dots, 5$) are six coefficients which depend on J . We write the chemical potentials at the boundaries as μ_B^L and μ_B^U which satisfy

$$n_B(\mu_B^L; J) = 2n_0 \quad n_B(\mu_B^U; J) = 5n_0. \quad (3.17)$$

It is important to remember that, μ_B^L and μ_B^U depend on J , since we use the fixed densities for the boundaries. The six parameters a_n are determined from the six boundary conditions,

$$\left. \frac{\partial^k P_I}{(\partial \mu_B)^k} \right|_{\mu_B^L(\mu_B^U)} = \left. \frac{\partial^k P_{\text{PDM(NJL)}}}{(\partial \mu_B)^k} \right|_{\mu_B^L(\mu_B^U)}, \quad (3.18)$$

where $k = 0, 1, 2$. Determination of a_n at $J = 0$ gives us the unified EOS.

We emphasize that, because of the causality condition, which means that the sound velocity must be physical as

$$c_s^2 = \frac{dP}{d\varepsilon} = \frac{n_B}{\mu_B \chi_B} \leq 1, \quad (3.19)$$

the model parameters of the generating functional are restricted.

3.3.2 A practical method to compute condensates

Here, let us explain a practical method to compute condensates in our description of the unified generating functional. In this method, it is not necessary to manifestly compute $P(\mu_B, J)$ for various J , but we utilize only the μ_B -dependence of the condensate at $J = 0$ for each interpolating boundary. The detail of the calculations are shown in Appendix. B. This method is useful especially when we need to compute many condensates.

Since we use the polynomial function with J -dependent coefficients in the interpolating domain, the expression of condensate ϕ in the interpolated domain is given by

$$\phi_{\text{I}} = -\frac{\partial P_{\text{I}}}{\partial J} \Big|_{J=0} = -\sum_{n=0}^5 \frac{\partial a_n}{\partial J} \Big|_{J=0} \mu_B^n. \quad (3.20)$$

Therefore, we just calculate the six coefficients $\partial a_n/\partial J$ ($n = 0, \dots, 5$) at $J = 0$ to obtain the condensate in interpolation ϕ_{I} . Using the interpolating condition in Eq.(3.18), the $\partial a_n/\partial J$ can be obtained by differentiating Eq.(3.18) with respect to J ,

$$\frac{\partial}{\partial J} \left(\frac{\partial^k P_{\text{I}}}{(\partial \mu_B)^k} \Big|_{\mu_B^L(\mu_B^U)} \right) = \frac{\partial}{\partial J} \left(\frac{\partial^k P_{\text{PDM(NJL)}}}{(\partial \mu_B)^k} \Big|_{\mu_B^L(\mu_B^U)} \right), \quad (3.21)$$

and setting $J = 0$ in the end. We note that the boundary values $\mu_B^L(\mu_B^U)$ are depending on J , see Appendix. B for the details.

It is noteworthy that all the derivatives at $J = 0$ can be computed using quantities at a specific μ_B and $J = 0$ only, without the need to consider quantities for different J or μ_B . As a result, our calculations are considered "local" and greatly reduce computational efforts.

3.3.3 Numerical results

We calculate the following quantities from nuclear to quark matter domain using the method presented in the above: the light quark chiral condensate $\langle \bar{u}u + \bar{d}d \rangle$, the strange quark condensate $\langle \bar{s}s \rangle$, the diquark gaps Δ_i , and the quark number densities n_f . Unless otherwise stated we pick up three sample

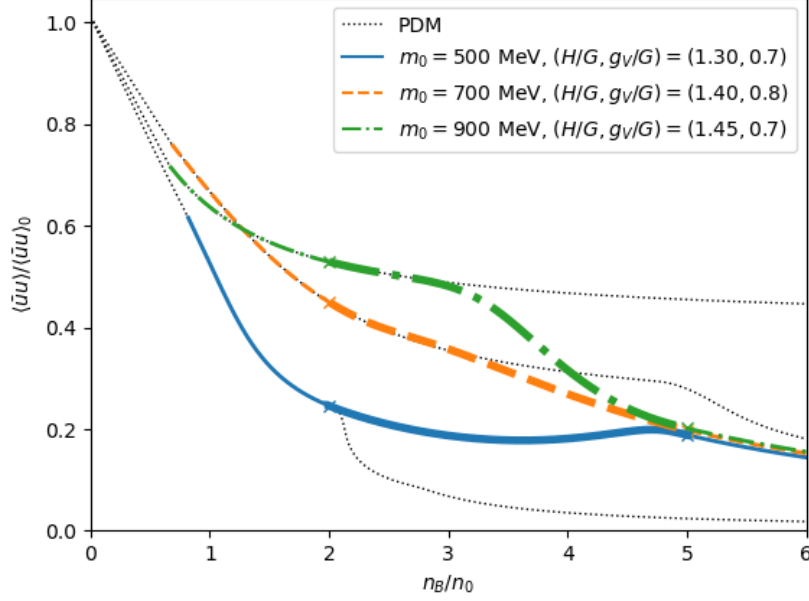


Figure 3.4: Ratio of the light quark chiral condensates compared with the vacuum value. In this model, $\langle \bar{u}u \rangle / \langle \bar{u}u \rangle_0 = \langle \bar{d}d \rangle / \langle \bar{d}d \rangle_0 = \langle \bar{u}u + \bar{d}d \rangle / \langle \bar{u}u + \bar{d}d \rangle_0$.

parameter sets for $(m_0 [\text{MeV}], H/G, g_V/G)$ as

$$\begin{aligned}
 (500, 1.30, 0.7), & \quad [\text{blue solid}] \\
 (700, 1.40, 0.8), & \quad [\text{orange dashed}] \\
 (900, 1.45, 0.7), & \quad [\text{green dash dotted}]
 \end{aligned} \tag{3.22}$$

all of which lead to EOS with the causal speed of sound. Here [...] indicates the types of lines used in figures for these parameters. As a guide, we will also show the extrapolation of the PDM results by black dotted lines.

Light quark chiral condensates

The ratio of the chiral condensate in medium to the vacuum counterpart, $\langle \bar{u}u + \bar{d}d \rangle / \langle \bar{u}u + \bar{d}d \rangle_0$, is displayed in Figure 3.4. It can be observed that the condensate at the boundaries strongly influences the condensate in the interpolated domain.

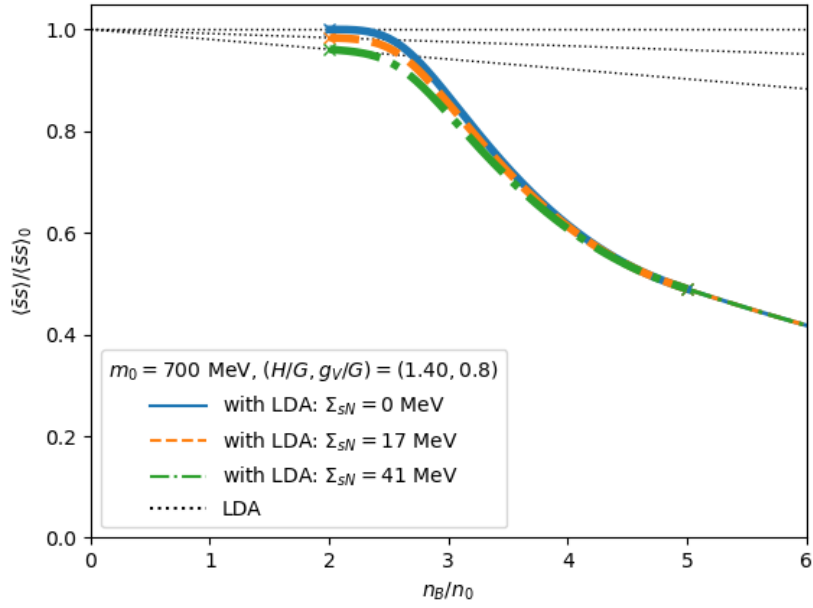
The choice of m_0 has a significant impact on the PDM results. When m_0 is set to 500 MeV, the chiral condensate experiences a drastic reduction because a strong N - σ coupling is needed to reproduce $m_N = 939$ MeV, resulting in significant changes to the behavior of σ in nuclear medium. However, for larger m_0 , the medium effects on σ become less pronounced. On the other hand, in the NJL model, the chiral condensates are typically around 20–30% of their vacuum values.

As discussed in Section 3.1.3, the chiral restoration within the PDM may not fully capture the chiral restoration at the quark level, and interactions among nucleons become stronger at higher densities, making it necessary to consider structural changes of nucleons and modifications of m_0 and the couplings. To infer the trends of these effects, we use the bias from the quark matter side. While our interpolating method is phenomenological, we believe it provides a reasonably balanced description.

Strange chiral condensates

Fig.3.5 illustrates the strange quark condensate, which is another quantity of interest. Let us first focus on the trend observed for $n_B \leq 2n_0$. In this work, the strange quark contributions are not defined in the PDM. However, we estimated them using the linear density approximation given in Eq.(3.11) with the strangeness sigma-term. The sigma-term values we used are $\Sigma_{sN} = 0, 17, 41$ MeV, with $\Sigma_{sN} = 0$ corresponding to a density-independent strange quark condensate, while the other two values were chosen from Ref. [97]. We fixed the parameters $m_0 = 700$ MeV and $(H, g_V)/G = (1.4, 0.8)$, and varied the values of Σ_{sN} . As anticipated, Fig.3.5 demonstrates that the chiral restoration in the strange quark sector is negligible in the nuclear regime.

As we move beyond $2n_0$, the strange quark condensate exhibits a reduction of approximately 20% at $n_B \simeq 3n_0$. This reduction is a result of the boundary condition bias in the quark matter side as per the construction. At $n_B \simeq 5n_0$, in the quark matter, the reduction is about 50%. Two main effects contribute to this chiral restoration. Firstly, the suppression of the anomaly term, $\sim \langle \bar{u}u \rangle \langle \bar{d}d \rangle \langle \bar{s}s \rangle$, associated with the reduction of light quark condensates. Secondly, the appearance of the strange quark Fermi sea. In our model, the strangeness density begins to account for around 10% of the quark density at $n_B \simeq 3n_0$, indicating that the strange quark sector is altered at the quark level.



Diquark gaps and number density

The upper and lower panels of Figure 3.6 depict the numerical results of diquark gaps interpolation in the ud -pairing channel and ds -pairing channel, respectively, using the same parameters as in Fig. 3.4. It is assumed that the diquark condensates are zero when the baryon density is less than or equal to $2n_0$. In CFL quark matter, the isospin symmetry is almost perfectly maintained, whereas in nuclear matter, the pairing is zero, which results in $\Delta_{ds} \simeq \Delta_{us}$ being reasonably accurate throughout the density range.

Let us now turn our attention to the relationship between the diquark condensates and quark number density, which is depicted in Fig. 3.7. In the nuclear regime, the quark densities for each flavor are derived from the proton and neutron densities (n_p and n_n) as $n_u = 2n_p + n_n$, $n_d = n_p + 2n_n$, and $n_s = 0$. We observe a strong correlation between the growth of the diquark condensates and the increase in quark number density, which is evident from the comparison between Figs. 3.6 and 3.7. This is intuitively reasonable since a larger Fermi surface allows for more diquark pairs, and the associated energy reduction of the system further promotes the growth of density.

Another crucial effect is the flavor asymmetry. Notably, the number density of strange quarks in nuclear matter is zero, while strong pairing between strange quarks and other light quarks favors equal population of u , d , and s -quarks in quark matter. Consequently, the number density of strange quarks increases rapidly in the interpolated region, and the onset of strangeness occurs at lower densities than it would without pairings. The interplay between the mass asymmetry and pairing effects determines the fraction of each quark.

Compositions

Lastly, we investigate the matter composition including leptons. The fraction of quark density for each flavor and lepton fraction per baryon density, denoted by n_f/n_B and n_l/n_B respectively, are presented in Figure 3.8. Here, f stands for u , d , or s , and the subscript l indicates the electron or muon densities. The lepton fraction is determined by the charge neutrality and β -equilibrium condition, which are controlled by the charge chemical potential μ_Q .

One of the distinct characteristics of our unified model is the evolution of the strangeness fraction. It becomes prominent at around $n_B \simeq 2.5n_0$,

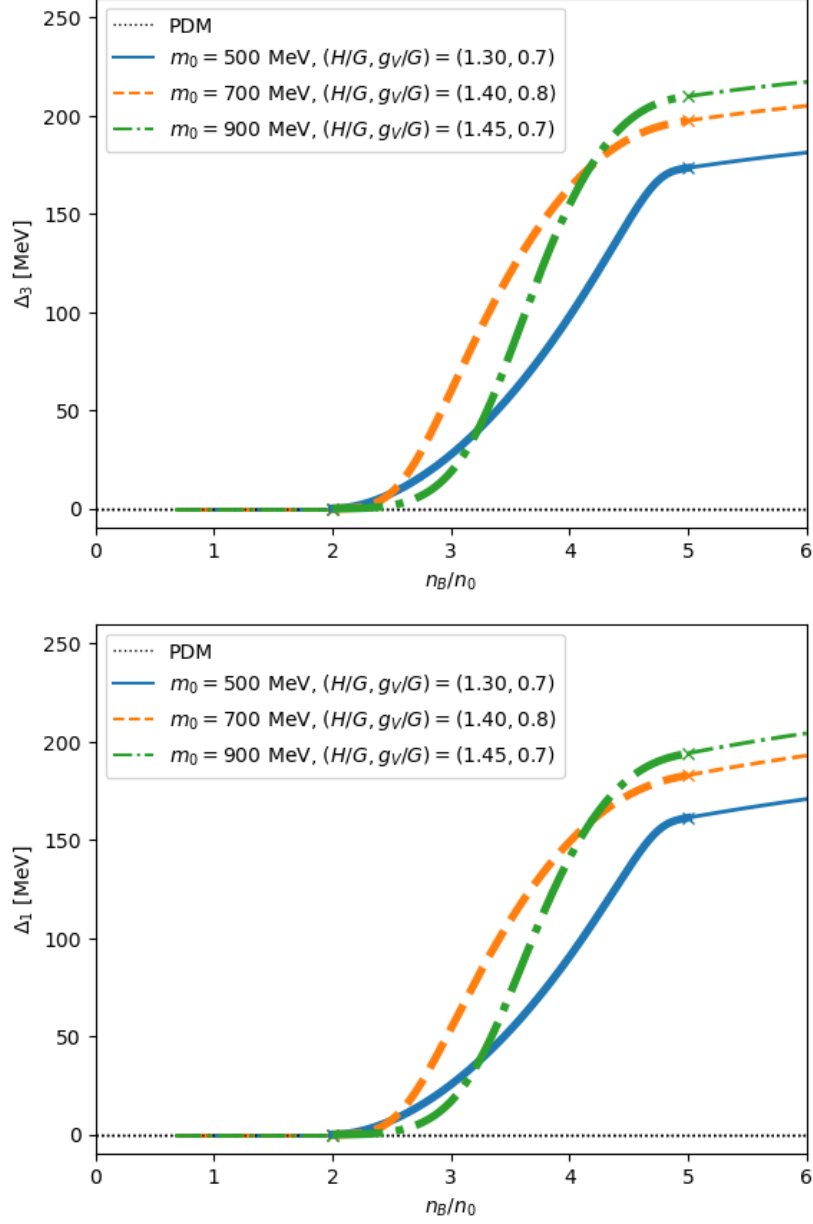


Figure 3.6: Diquark condensates. The upper panel is $\Delta_3(= \Delta_{ud})$, and the lower panel is $\Delta_1(= \Delta_{ds})$. $\Delta_2(= \Delta_{su})$ is the same as Δ_1 in this model. In hadronic matter, we assume the diquark condensates equal zero.

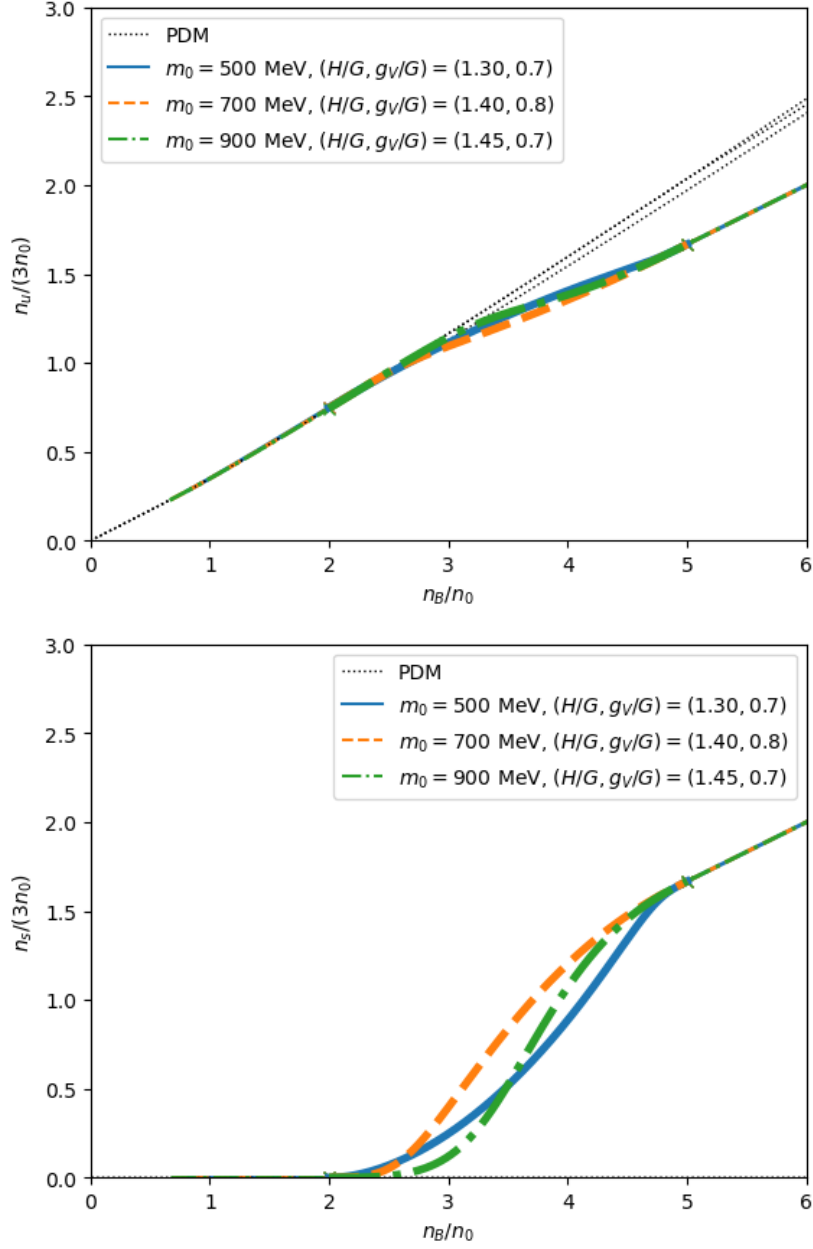


Figure 3.7: Number density for up-quarks n_u (upper), and strange-quarks n_s (lower), normalized by $3n_0$. In hadronic matter, we defined as $n_u = 2n_p + n_n$, ($n_d = n_p + 2n_n$,) and $n_s = 0$

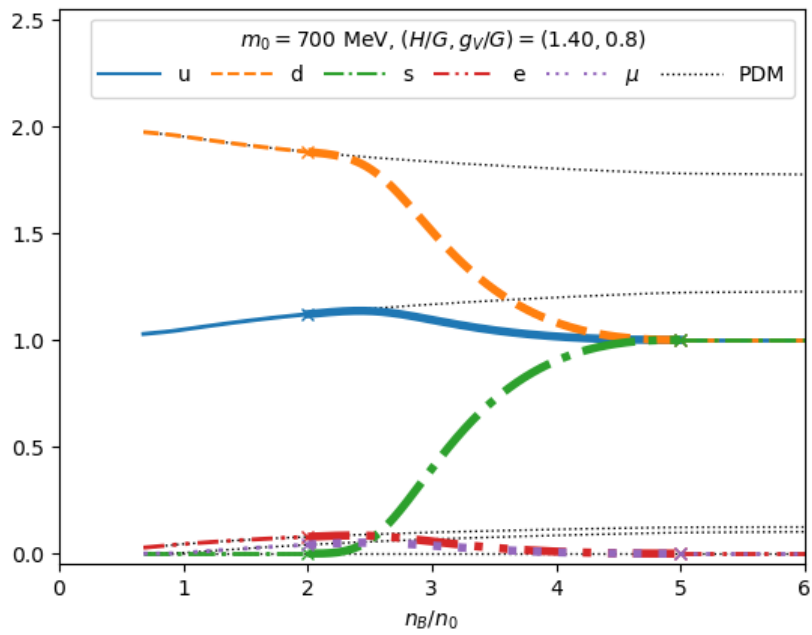


Figure 3.8: Matter composition n_f/n_B ($f = u, d, s$) and n_l/n_B as functions of baryon density.

and strange quarks are as abundant as up- and down-quarks at $n_B \gtrsim 4.5n_0$. When $n_B = 5n_0$, the matter transforms into CFL quark matter, where the sum of quark densities satisfies the charge neutrality condition and no leptons are required. This deviation from pure nuclear models, in which the lepton fraction increases with increasing baryon density, highlights the uniqueness of our approach.

3.4 Discussions

In this study, the chiral condensates in the crossover region are derived by interpolating those in nuclear and quark matter domains, which makes our observations of chiral restoration somewhat indirect. The impact of confinement on this process remains uncertain. In this section, we propose several scenarios to speculate about the microphysics in the interpolated domain.

3.4.1 Casher's argument and the chiral scalar density in nucleons

Regarding the relationship between confinement and chiral symmetry breaking, Casher suggested that quark confinement cannot be described in the absence of chiral symmetry breaking effects (Casher, 1979). In this work, we relax Casher's arguments slightly by assuming the presence of chiral variant fields, namely $(\sigma, \vec{\pi})$. The overall size of these fields is characterized by $\phi^2 \equiv (\sigma^2 + \vec{\pi}^2)$, which is chiral invariant, while the direction of the four vector $(\sigma, \vec{\pi})$ is chiral variant.

Casher's argument centers around the helicity of a massless quark. Confinement requires the quark to change directions without changing its spin, which violates either the conservation of helicity or angular momentum. To avoid this violation, the confining boundaries must generate fields³ that can carry the quanta of quarks just before reflection, as shown in Figure 3.9. The σ and $\vec{\pi}$ fields are candidates for such fields, as they transform a left-handed (right-handed) quark into a right-handed (left-handed) one, while the four-vector $(\sigma, \vec{\pi})$ rotates to conserve helicity. This intuitive picture will be further developed in the next section.

³One can also think of the instantons as the sources of the chirality flipping; in this picture σ appears due to quarks bound to instantons [110].

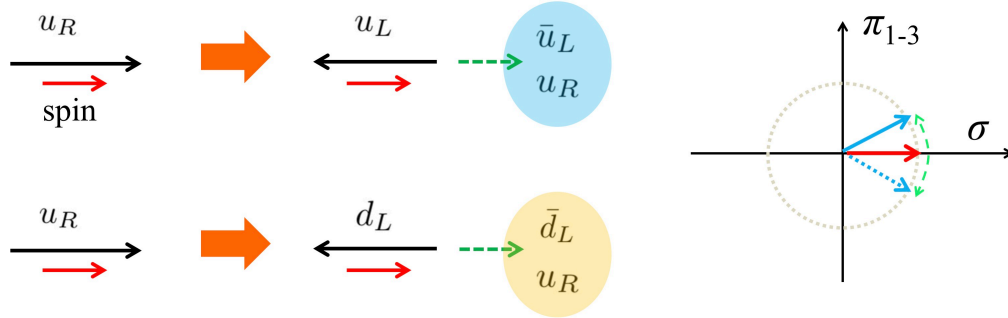


Figure 3.9: Helicity and spin conservation due to the emergence of the $(\sigma, \vec{\pi})$ fields. The confinement turns a right-moving quark, u_R , into a left-moving quark, u_L (d_L), but without changing the spin. The helicity is conserved by fields made of $\bar{u}_L u_R$ ($\bar{d}_L u_R$). The $(\sigma, \vec{\pi})$ fields fluctuate whenever the chirality of quarks flip.

Using the above-described picture, we can examine the consequences that may arise. The first implication is that Casher's argument naturally implies the existence of the chiral scalar density in hadrons. This may be linked to the in-hadron condensate concept. On the other hand, when discussing the vacuum condensates within this framework, we need to consider the σ meson as a confined particle and then discuss the condensation of σ mesons. Once the σ mesons fill the space, quarks can change their chirality anywhere.

3.4.2 Topology of pion clouds and spatial modulations of the chiral scalar density

The scalar density of nucleons has a magnitude similar to that of the vacuum chiral condensate, but with an opposite sign. Extrapolating this idea would suggest that as nucleons overlap, they form a large region dominated by positive chiral scalar density (negative σ), which is larger than the negative chiral scalar density (positive σ) from the vacuum, as shown in Fig.3.10. However, this expectation does not match smoothly with the high-density quark model descriptions, where the chiral scalar density approaches zero instead of a positive value. To understand this discrepancy, we first examine the chiral scalar density in a two-baryon system.

To better understand how the σ field changes sign from the vacuum to the inside of a nucleon, we will examine this process in more detail. Since the

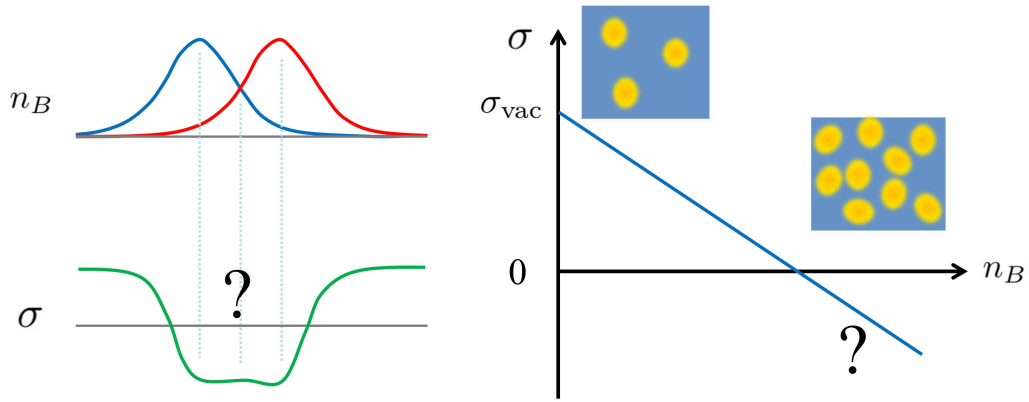


Figure 3.10: Naive extrapolation of the linear density approximation for the chiral condensate. As baryons overlap, the positive chiral scalar density (negative σ) from baryons dominates over the negative scalar density from vacuum one ($\sigma > 0$).

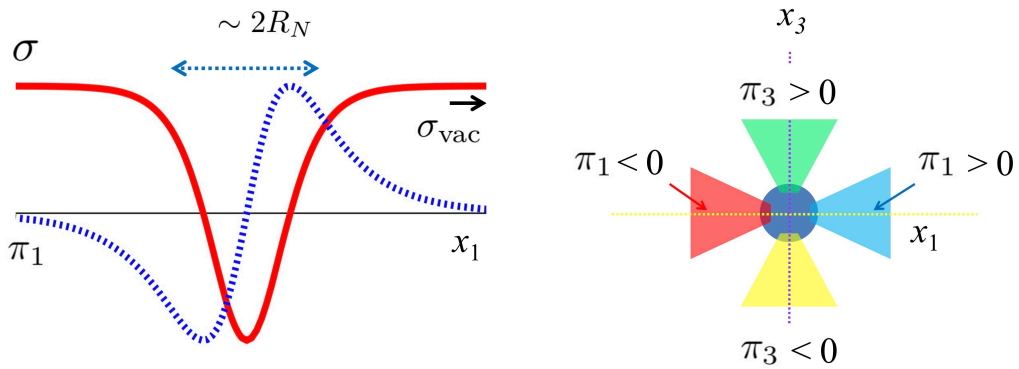


Figure 3.11: Expected behavior of chiral scalar (σ) and pseudo scalar fields ($\vec{\pi}$) near a nucleon (one dimensional slice). The chiral invariant combination of these fields are $\sigma^2 + \vec{\pi}^2 \simeq \text{const}$. The right is the hedgehog profile.

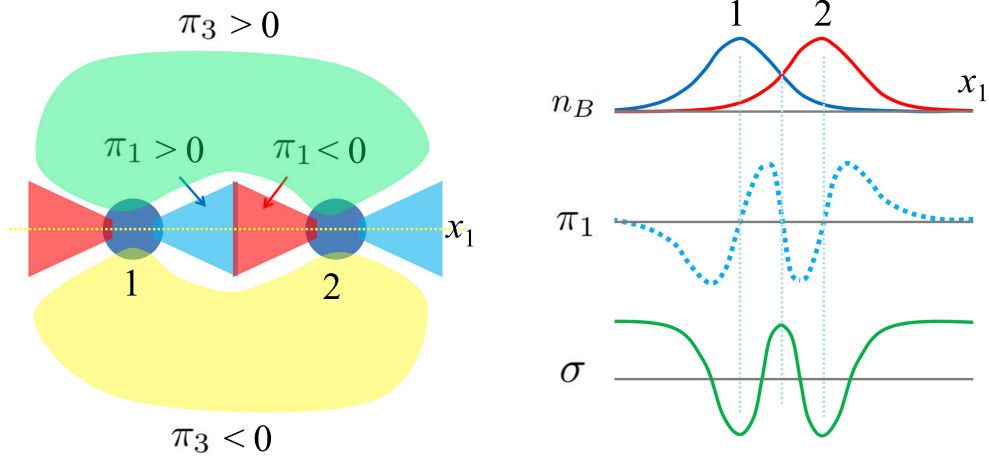


Figure 3.12: Two nucleons at close distance, with the hedgehog pion configurations, where the vectors $\vec{\pi}$ and \mathbf{x} are parallel. The rightmost part shows the baryon density, π_1 fields, and σ fields along the x_1 axis. The negative σ fields are accumulated at the center of baryons, while the positive σ are accumulated at the interface of two baryons.

effective Lagrangian is chiral symmetric, the effective potential is a function of ϕ^2 . At the vacuum, the potential takes a minimum at $\phi = \sigma_{\text{vac}}$. We assume that the field variation along this circle ($\phi = \text{const.}$) does not require much energy. Therefore, the σ field around a nucleon should be accompanied by π fields whose magnitudes are large near the surface of the nucleon and vanishing at the center, as depicted in Fig.3.11. The spatial average of π fields is zero. By appropriately arranging the isospin distributions for these $\vec{\pi}$ fields to generate a topological number of one in the hedgehog form, we can arrive at descriptions similar to those in chiral soliton models [111–118].

To better understand how baryons come close together, we can examine the topological numbers of pions around nucleons. Consider two nucleons that are close in distance, as shown in Fig.3.12. In a naive description, two domains of positive scalar density simply merge to form one large domain with the positive scalar density (negative σ), as shown in Fig.3.10. However, this picture is corrected by considering the topological constraint, as illustrated in Fig.3.12. For two nucleon problems, the configuration of $(\sigma, \vec{\pi})$ must have nodes to generate topological numbers two⁴, rather than zero.

⁴In (1+1)-dimensional models such statements become exact by applying the bosoniza-

Hence, $(\sigma, \vec{\pi})$ should have spatial modulations with positive and negative scalar densities, instead of forming a single large domain with the positive scalar charge. As more and more nucleons are packed, the spatial modulations of $(\sigma, \vec{\pi})$ fields become finer. The positive and negative σ fields tend to cancel only in the spatial average. The magnitudes of the modulations are controlled by the size of ϕ , not by the value of σ . While the nucleon and constituent quark masses are substantial as long as ϕ is nonzero, we can still describe the chiral restoration in the sense of $\int_{\mathbf{x}} \sigma(x) = 0$. This picture fits with the concept of the chiral invariant mass in the PDM, which can be nonzero even for $\sigma = 0$, as discussed in Refs. [127, 128].

In the previous argument, we discussed the possibility that each nucleon has a topological configuration with spatial modulations in σ and $\vec{\pi}$. This idea is similar to the concept of chiral density waves in the PDM, as discussed in Refs. [36, 46, 47]. As nuclear matter is compressed, these modulations do not cancel but are squeezed together, as long as ϕ remains finite. This viewpoint is in line with scenarios of soliton crystals [129–133] or chiral spirals [134–144]. If compressed nucleons prefer a periodic structure, they can also lead to a lattice in $(\sigma, \vec{\pi})$. Inhomogeneous chiral condensates have been discussed in both nucleonic and quark models, and it is an interesting question whether they can be connected through the quark-hadron continuity (see Ref. [145] and references therein).

3.4.3 Diquarks

Finally, we will explore the evolution of diquark condensates from nuclear to quark matter. Given our assumption that nucleon fields, before diagonalizing the mass matrix, transform as $(1/2, 0)_L \oplus (0, 1/2)_R$ under the chiral multiplet, a straightforward approach for combining three quarks is to first consider diquarks in the color antitriplet representation, followed by attaching a leftover quark. The diquarks $[u_L d_L]_{I=0}$ and $[u_R d_R]_{I=0}$ are singlets under $SU(2)_L \times SU(2)_R$ chiral transformations, thus invariant. When we attach the leftover quark to these diquarks, the resulting nucleon will follow the chiral transformation of the leftover quark. Additionally, we assume that the diquark has $J^P = 0^+$ and is in a spatial S-wave, where the attractive correlations are strongest. Consequently, the nucleon already contains the diquark

tion method [119–122]; $n_B \sim \partial_1 \varphi$, $\sigma \sim \cos \varphi$, and $\pi \sim \sin \varphi$ (for $U(1)$). Studies of dense systems can be found, e.g. in Refs. [123–126].

condensate source for high-density matter.

When the density is low, diquark correlations exist, but diquarks are bound tightly to leftover quarks to form nucleons. Thus, the diquarks are not observable as condensates that spread over the system, and the properties of the system are described in terms of nucleons. However, when quark exchanges between nucleons become frequent, diquarks are no longer limited to being constituents of nucleons but also participate in the bulk properties of the system. As the diquark fields begin to overlap, they become coherent, and the phase of condensates, φ in $\Delta = |\Delta|e^{i\varphi}$, correlates over long distances. The development of diquark condensates starts when nuclear many-body forces become significant (at $n_B \gtrsim 2n_0$), progresses gradually towards quark matter, and becomes established at high densities ($n_B \gtrsim 5n_0$)⁵.

According to the same conceptual framework, we anticipate the introduction of diquark fields with strangeness into the system as constituents of hyperons. Subsequently, as hyperons dissociate via quark exchanges, the diquark fields are expected to gradually develop.

3.5 Summary of Ch.3

In this thesis, we have presented a methodology for computing a range of condensates in the intermediate region between nuclear and quark matter, based on the concept of quark-hadron continuity. By examining the properties of these condensates, we have subsequently proposed potential qualitative scenarios for bridging the gap between descriptions of nuclear and quark matter.

In Chapter 2, we have observed that the PDM with a substantial chiral invariant mass, $m_0 \gtrsim 500$ MeV, exhibits several favorable characteristics in terms of describing the EOS and various condensates. Notably, the significant reduction in σ at low densities (due to the positive scalar charge in nucleons) has a negligible effect on nucleon properties, which is in line with our decision to neglect the nucleon Dirac sea and assume fixed nucleon-meson couplings for $n_B \lesssim 2n_0$. We believe that the intrinsic properties of nucleons begin to

⁵The development of diquark pair condensations could be limited by the cooling of neutron stars. In particular, certain cooling patterns disfavor significant CFL cores that would cause excessively rapid cooling [146, 147]. One possible explanation is that these observed neutron stars are not heavy enough and do not possess high-density cores. However, if these neutron stars are massive and have large core densities, they impose strict restrictions on the CFL phase. For information on the cooling of accreting neutron stars, refer to Ref. [148].

undergo significant changes at $n_B \gtrsim 2n_0$, where quark exchanges between baryons occur more frequently; given that baryons consist of quarks, such exchanges are expected to modify the structure of baryons. Additionally, the quarks that are partially released are also impacted by the surrounding medium, which can alter their effective mass and other properties. Although directly characterizing these changes is challenging, we can at least place constraints on them based on quark matter behaviors at high densities. Our interpolation method provides a practical approach to implementing these concepts.

This study has only touched on a few aspects of chiral symmetry in dense matter, and there are numerous issues that remain to be addressed. Here, we outline several:

(i) The PDM model can be expanded to incorporate hyperons [34, 149–153]. For neutron star matter, the charge chemical potential μ_Q ranges from -100 MeV to -200 MeV around $n_B \sim 1-2n_0$, and hyperons may emerge for $2-3n_0$, not far from our selected hadronic boundary $n_B = 2n_0$ (see, for instance, Sec. III in Ref. [154]). Incorporating hyperons and extending our treatment to higher densities would provide more concrete descriptions of strangeness than what is presented in this work.

(ii) A thorough understanding of a nucleon and its meson cloud should provide insight into chiral symmetry in dense matter. A crucial question regarding the PDM is how a $(\sigma, \vec{\pi})$ cloud differs for nucleons of positive ($N(939)$) and negative parity ($N(1535)$). According to constituent quark models, $N(1535)$ contains a quark’s P-wave excitation and is more spatially extended than $N(939)$. Understanding the relationship between this size-scale estimate and σ in the PDM is critical for comprehending the medium effects in the PDM. In general, medium effects should impact hadrons with larger sizes, as they are closer in proximity to other hadrons.

(iii) Ultimately, our patchwork of nuclear and quark matter descriptions should be superseded by a model based on a single framework. Baryons should be explicitly constructed in terms of quarks. Several recent studies [155–158], although schematic, have provided concrete descriptions of quarks from nuclear to quark matter domains. One important outcome is the peak in the speed of sound [156–158], which has been a puzzling feature inferred from neutron star observations [159]. However, detailed questions, such as the fate of chiral symmetry breaking or diquark correlations, have not been addressed in these models. Our descriptions in this thesis may offer some insight into fully understanding nuclear-quark matter phase transitions.

Chapter 4

Conclusion

In this thesis, we studied the chiral condensate and the chiral invariant mass constructing a unified EOS for neutron stars based on quark-hadron crossover. What we obtained in our researches are as the following.

In Ch.2, we constructed unified EOSs by interpolating the EOS of the PDM at lower density and that of the NJL model at higher density. We found that the value of m_0 affects the nuclear EOSs at low density, and has strong correlations with the radii of neutron stars. The radii of the neutron star with $1.4 M_\odot$ are known to have strong correlations with the stiffness of low density EOS beyond the saturation density, $n_B = 1-2n_0$, and indeed we have obtained the nontrivial constraint, $600 \lesssim m_0 [\text{MeV}] \lesssim 900$. At low density, the density dependence of the stiffness is sensitive to the balance between the σ - and ω -exchanges, where the strength of the former strongly depends on the fraction of the chiral variant component in the nucleon mass.

In Ch.3, we studied the chiral condensate in the domain between nuclear and quark matter, assuming the quark-hadron continuity picture. We found that the chiral condensate decreases mildly at lower density and smoothly approaches the NJL predictions at higher density using the value of the substantial chiral invariant mass, which is favored by the neutron star observations. In our descriptions the chiral restoration in the interpolated domain proceeds with two conceptually distinct chiral restoration effects; the first is associated with the positive scalar density in a nucleon, relevant in dilute regime, and the other primarily arises from the modification of the quark Dirac sea, which is triggered by the growth of the quark Fermi sea.

In the future, when it becomes possible to observe the radius with higher precision by the gravitational observations of such as LIGO-Virgo, or by the

X-ray observations of such as NICER, we can obtain more precise constraint to the hadronic model, and it will be strong guidelines to construct hadronic effective models. Moreover, if we apply our models to other physics of neutron stars, such as neutrino emissions, binary merger dynamics, or cooling process, we will be able to know more about the hadron physics and the microscopic understanding for neutron stars. In our result, the typical neutron stars with $\sim 1.4M_{\odot}$ have cores in crossover domain, and the heaviest neutron stars with $\sim 2.0M_{\odot}$ may have the quark matter cores. Comparing the neutrino emission rate of the hadronic matter and the one of the quark matter, we may discuss it with the observational data of neutron stars.

Acknowledgments

I would like to deeply thank Professor Masayasu Harada for his helpful discussions and the patient encouragement. I would also like to thank Professor Toru Kojo. I have been extremely lucky to have such a research collaborator who cared very much about my research.

I am also very grateful to Gao Bikai and the other H laboratory members for invaluable discussions. Moreover, EHQG members gave me the fruitful environment to study.

This work of T. M. was supported by JST SPRING, Grant No. JPMJSP2125.

Appendix A

Chiral condensate and pion-nucleon sigma-term in hadron effective models

A.1 Some definitions

First, we list some definitions for convenience below.

The scalar charge of nucleons is defined as

$$N_\sigma := \int_{\mathbf{x}} \langle N | \bar{q}q | N \rangle = \left. \frac{\partial m_N}{\partial m_q} \right|_{\text{vac}}, \quad (\text{A.1})$$

and the pion-nucleon sigma-term (or simply sigma-term) is also defined as

$$\Sigma_N := \int_{\mathbf{x}} \langle N | m_q \bar{q}q | N \rangle = m_q \left. \frac{\partial m_N}{\partial m_q} \right|_{\text{vac}} \equiv m_q \left. \frac{\partial \langle \bar{q}q \rangle}{\partial n_B} \right|_{\text{vac}}, \quad (\text{A.2})$$

where $\bar{q}q = \bar{u}u + \bar{d}d$ is the scalar operator of the up and down quark fields, and $m_q = \bar{m} = (m_u + m_d)/2$ is the average current quark mass for up and down quarks.

A.2 Linear density approximation (LDA) for chiral condensate

The linear density approximation (LDA) for the chiral condensate is the low-density expansion of the chiral condensate, which can be calculated as

$$\langle \bar{q}q \rangle = \frac{\partial \Omega}{\partial m_q} \quad (\text{A.3})$$

$$= \frac{\partial \Omega_{\text{vac}}}{\partial m_q} + \frac{\partial(\Omega - \Omega_{\text{vac}})}{\partial m_q} \quad (\text{A.4})$$

$$= \langle \bar{q}q \rangle_{\text{vac}} - \frac{\partial P}{\partial m_q} \quad (\text{A.5})$$

$$= \langle \bar{q}q \rangle_{\text{vac}} - \frac{\partial m_N}{\partial m_q} \frac{\partial P}{\partial m_N} \quad (\text{A.6})$$

$$= \langle \bar{q}q \rangle_{\text{vac}} + \frac{\sum_N n_\sigma}{m_q} \quad (\text{A.7})$$

$$\approx \langle \bar{q}q \rangle_{\text{vac}} + \frac{\sum_N n_B}{m_q} \quad (\text{as } n_B/n_0 \ll 1), \quad (\text{A.8})$$

where n_σ is the scalar charge density for nucleons as the following

$$n_\sigma := -\frac{\partial P}{\partial m_N} \quad (\text{A.9})$$

$$= -\frac{\partial}{\partial m_N} 2 \sum_{\alpha: \text{isospin}} \int_{\mathbf{p}}^{k_F} (\mu_\alpha^* - E_{\mathbf{p}}) \quad (\text{A.10})$$

$$= 2 \sum_{\alpha} \int_{\mathbf{p}}^{k_F} \frac{m_N}{E_{\mathbf{p}}} \quad (E_{\mathbf{p}} := \sqrt{m_N^2 + \mathbf{p}^2}) \quad (\text{A.11})$$

$$= 2 \sum_{\alpha} \int_{\mathbf{p}}^{k_F} \left[1 - \frac{1}{2} \left(\frac{\mathbf{p}}{m_N} \right)^2 + \mathcal{O} \left(\frac{\mathbf{p}}{m_N} \right)^4 \right] \quad (\text{A.12})$$

$$= 2 \sum_{\alpha} \frac{1}{2\pi^2} \left[\frac{k_F^3}{3} - \frac{1}{10} \frac{k_F^5}{m_N^2} + \mathcal{O}(k_F^7) \right] \quad (\text{A.13})$$

$$= n_B - \frac{3^{5/3} \pi^{4/3}}{10 \cdot 2^{2/3}} \frac{n_B^{5/3}}{m_N^2} + \mathcal{O}(n_B^{7/3}) \quad (\text{A.14})$$

where $n_B = \frac{2k_F^3}{3\pi^2}$ assuming symmetric matter in the last step. As see Eq.(A.14), the scalar density can be equal to the baryon number density n_B approxi-

mately in low density regime:

$$n_\sigma \approx n_B \quad \text{as} \quad n_B/n_0 \ll 1. \quad (\text{A.15})$$

Note that, Eq.(A.14) is not Taylor expansion in terms of n_B , because this is expansion around $n_B = 0$, which is the branch point of the coordinate transformation $k_F \propto n_B^{1/3}$. When we expand around $n_B \neq 0$, the series must be Taylor expansion.

A.3 Chiral condensate in the PDM

As we see in Eq.(1.21) in Subsec.1.2.2, the chiral condensate (quark condensate) in the PDM can be calculated from the scalar meson mean field σ as

$$\langle \bar{q}q \rangle^{\text{PDM}} (= \langle \bar{u}u + \bar{d}d \rangle^{\text{PDM}}) = -\epsilon\sigma. \quad (\text{A.16})$$

There are the relation $\epsilon\bar{m} = m_\pi^2 f_\pi$, which corresponds to the Gell-Mann–Oakes–Renner relation. $\bar{m} = (m_u + m_d)/2 \approx 5.5$ MeV is the mean value of the up and down current quark masses, and $m_\pi \approx 140$ MeV is the pion mass. In vacuum (zero temperature and zero density), using $\sigma_{\text{vac}} = f_\pi \approx 93$ MeV,

$$\langle \bar{q}q \rangle_0^{\text{PDM}} = -m_\pi^2 f_\pi^2 / \bar{m} \approx -(249 \text{ MeV})^3 \times 2 \quad (\text{A.17})$$

Under mean field approximation, since the mean fields $\vec{\phi} := \{\sigma, \omega, \dots; \mu_Q, \dots\}$ are determined by the gap equations (and charge neutralities) as functions of the chemical potential μ_B , the chiral condensate is calculated as the following

$$\langle \bar{q}q \rangle^{\text{PDM}} = \langle \bar{u}u + \bar{d}d \rangle^{\text{PDM}} \quad (\text{A.18})$$

$$= \left(\frac{\partial \Omega_{\text{PDM}}}{\partial m_u} \right)_{\mu_B} + \left(\frac{\partial \Omega_{\text{PDM}}}{\partial m_d} \right)_{\mu_B} \quad (\text{A.19})$$

$$= \left(\frac{\partial \Omega_{\text{PDM}}}{\partial \bar{m}} \right)_{\mu_B} \quad (\text{A.20})$$

$$= \left[\left(\frac{\partial}{\partial \bar{m}} \right)_{\mu_B, \vec{\phi}} + \frac{\partial \vec{\phi}}{\partial \bar{m}} \cdot \left(\frac{\partial}{\partial \vec{\phi}} \right)_{\mu_B, \bar{m}} \right] \Omega_{\text{PDM}} \quad (\text{A.21})$$

$$= \left(\frac{\partial}{\partial \bar{m}} \right)_{\mu_B, \vec{\phi}} \Omega_{\text{PDM}}. \quad (\text{A.22})$$

In the last line, we use the gap equations $(\partial\Omega/\partial\vec{\phi})_{\mu_B, \bar{m}} = 0$, and therefore the chiral condensate can be obtained by partial differentiating the potential with respect to the quark mass.

The chiral condensate can be divided to the two parts: the vacuum part and the matter depended part as

$$\langle \bar{q}q \rangle = -\epsilon\sigma \quad (\text{A.23})$$

$$= -\epsilon f_\pi + \epsilon(f_\pi - \sigma) \quad (\text{A.24})$$

$$= \langle \bar{q}q \rangle_0 + \frac{m_\pi^2 f_\pi}{\bar{m}} (f_\pi - \sigma) \quad (\text{A.25})$$

Expanding σ at $n_B = 0$, and comparing it with Eq.(A.8), the sigma-term for PDM can be calculated as

$$\Sigma_N = \frac{m_\pi^2 f_\pi}{\chi_B} \frac{\partial\sigma}{\partial\mu_B}, \quad (\text{A.26})$$

where $\chi_B = \frac{\partial^2 P}{\partial\mu_B^2}$ is the baryon number susceptibility.

Fig. A.1 is the ratio of the chiral condensate for the pure neutron matter. For comparison, we also plot the two black dotted lines which are corresponding to the linear density approximation with two values of the sigma-term $\Sigma_N = 45 \text{ MeV}, 90 \text{ MeV}$.

A.4 Tilt of the chiral condensate in the PDM

In the PDM, the chiral condensate is given as in Eq. (A.16) and its graph is shown in Fig. A.1. The slope of the graph is calculated as

$$\frac{\partial \langle \bar{q}q \rangle^{\text{PDM}}}{\partial n_B} = \frac{\partial\mu_B}{\partial n_B} \frac{\partial(-\epsilon\sigma)}{\partial\mu_B} \quad (\text{A.27})$$

$$= -\frac{\epsilon}{\chi_B} \frac{\partial\sigma}{\partial\mu_B} \quad (\text{A.28})$$

where $\chi_B = \frac{\partial^2 P}{\partial\mu_B^2}$ is the baryon number susceptibility and $\frac{\partial\sigma}{\partial\mu_B}$ can be calculated analytically from gap equations (See Eq.(B.14) in Ch.B). Therefore, the linear density approximation of the chiral condensate at each density n^*

$$\langle \bar{q}q \rangle^{\text{PDM}} = \langle \bar{q}q \rangle_0^{\text{PDM}} + \left(\frac{\partial \langle \bar{q}q \rangle^{\text{PDM}}}{\partial n_B} \right)_{n_B=n^*} (n_B - n^*) + \mathcal{O}(n_B - n^*)^2 \quad (\text{A.29})$$

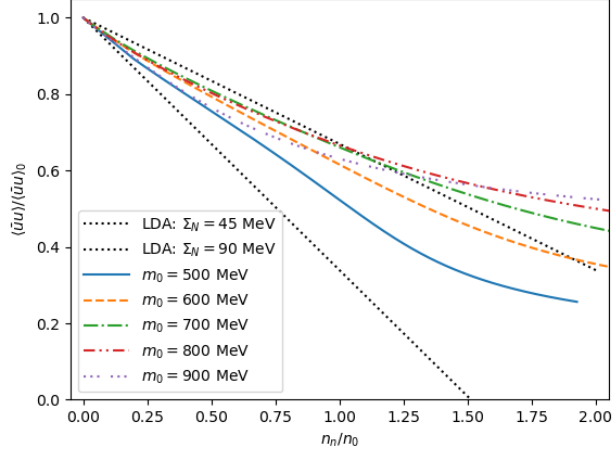


Figure A.1: The ratio of the chiral condensate in the PDM $\langle \bar{u}u \rangle / \langle \bar{u}u \rangle_0 = \langle \bar{q}q \rangle / \langle \bar{q}q \rangle_0 = \sigma / f_\pi$ versus the baryon (neutron) number density n_n for the pure neutron matter.

From this, we can define a sigma-term-like quantity at each density as the following

$$\Sigma_N(n_B) = \bar{m} \frac{\partial \langle \bar{q}q \rangle}{\partial n_B} \quad (\text{A.30})$$

$$= \frac{\bar{m}}{\chi_B} \frac{\partial \langle \bar{q}q \rangle}{\partial \mu_B} \quad (\text{A.31})$$

$$= -\epsilon \bar{m} \frac{1}{\chi_B} \frac{\partial \sigma}{\partial \mu_B} \quad (\text{A.32})$$

Fig. A.2 is the graph of the Σ_N -like quantity in Eq. (A.32). In the case of $m_0 = 500$ MeV, there is a first order phase transition in vacuum so the graph jumps. Also, χ_B and $\partial \sigma / \partial \mu_B$ are equal to zero in vacuum so Eq. (A.32) becomes indeterminate form as zero density limit. We can evaluate the value with using a relation between σ and density in the next section.

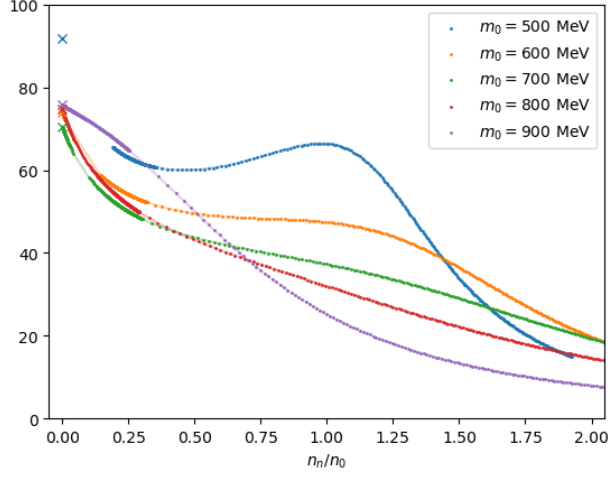


Figure A.2: The slope of the graph shown in Fig. A.1. The cross symbols are the values calculated in Sec. A.5 (Eq. (A.47)).

A.5 Relation between a scalar meson and a scalar density and estimation of the value of sigma-term in vacuum

For the potential of the scalar meson $V_s(\sigma)$, its Taylor expansion w.r.t. $\tilde{\sigma} := f_\pi - \sigma$ is

$$V_s(\sigma) = V_s(f_\pi - \tilde{\sigma}) \quad (\text{A.33})$$

$$= V_s(f_\pi) - V'_s(f_\pi)\tilde{\sigma} + \frac{1}{2}V''_s(f_\pi)\tilde{\sigma}^2 + \mathcal{O}(\tilde{\sigma}^3) \quad (\text{A.34})$$

$$= V_s(f_\pi) + \frac{1}{2}m_\sigma^2\tilde{\sigma}^2 + \mathcal{O}(\tilde{\sigma}^3) \quad (\text{A.35})$$

where $V'_s(f_\pi) = 0$ (stationary condition in vacuum) and $m_\sigma^2 := V''_s(f_\pi)$ is the mass of σ in vacuum. Using this, the stationary condition for σ can be written as

$$0 = \frac{\partial \Omega_{\text{PDM}}}{\partial \sigma} \quad (\text{A.36})$$

$$= \frac{\partial}{\partial \sigma}(V(\sigma) + \Omega_b) \quad (\text{A.37})$$

$$= V'(\sigma) + \sum_{i=\pm} \frac{\partial m_i}{\partial \sigma} n_s^i \quad (n_s^i = \frac{\partial \Omega_b}{\partial m_i} \text{ is the scalar density of a nucleon } N_i)$$
(A.38)

$$= V'(f_\pi - \tilde{\sigma}) + \sum_{i=\pm} \frac{\partial m_i}{\partial \sigma} n_s^i$$
(A.39)

$$= V'(f_\pi) - V''(f_\pi)\tilde{\sigma} + \mathcal{O}(\tilde{\sigma}^2) + \sum_{i=\pm} \frac{\partial m_i}{\partial \sigma} n_s^i$$
(A.40)

$$= -m_\sigma^2 \tilde{\sigma} + \mathcal{O}(\tilde{\sigma}^2) + \sum_{i=\pm} \frac{\partial m_i}{\partial \sigma} n_s^i$$
(A.41)

Therefore, we get

$$m_\sigma^2 \tilde{\sigma} \approx \sum_{i=\pm} \frac{\partial m_i}{\partial \sigma} n_s^i \quad (\text{PDM})$$
(A.42)

which is similar as that of Walecka model. For Walecka model, when we write its grand potential as $\Omega_{\text{Walecka}} := \frac{1}{2}m_\sigma^2 \tilde{\sigma}^2 - \frac{1}{2}m_\omega^2 \omega^2 + \Omega_b$, its stationary condition for $\tilde{\sigma}$ is

$$0 = \frac{\partial \Omega_{\text{Walecka}}}{\partial \tilde{\sigma}} = m_\sigma^2 \tilde{\sigma} + \frac{\partial M_N}{\partial \tilde{\sigma}} \frac{\partial \Omega_b}{\partial M_N} = m_\sigma^2 \tilde{\sigma} - g_{\sigma NN} n_s \quad (\text{Walecka})$$
(A.43)

where $M_N = M_{N0} - g_{\sigma NN} \tilde{\sigma}$ is the effective nucleon mass of a nucleon, so we get $m_\sigma^2 \tilde{\sigma} = g_{\sigma NN} n_s$.

We consider Eq. (A.16) again with using Eq. (A.42) to obtain a relation between σ and density. Here, we assume the baryon number density is sufficiently less than the saturation density: $n_B \ll n_0$. It means that the negative parity nucleons do not appear and the scalar density of the positive parity nucleons equals the baryon number density approximately. Then, Eq. (A.42) becomes $m_\sigma^2 \tilde{\sigma} \approx (\partial m_+ / \partial \sigma)_{\text{vac.}} n_B$ as $n_B \ll n_0$. Using this, the chiral condensate is

$$\langle \bar{q}q \rangle = -\epsilon \sigma$$
(A.44)

$$= -\epsilon f_\pi + \epsilon \tilde{\sigma}$$
(A.45)

$$\approx \langle \bar{q}q \rangle_0 + \epsilon \frac{1}{m_\sigma^2} \left(\frac{\partial m_+}{\partial \sigma} \right)_{\text{vac.}} n_B$$
(A.46)

Table A.1: Values of PDM in vacuum

m_0 [MeV]	500	600	700	800	900
$(\partial m_+ / \partial \sigma)_{\text{vac.}}$	7.97	7.01	5.87	4.56	3.07
m_σ [MeV]	396	414	388	332	271
Σ_N [MeV]	91.9	74.0	70.5	74.6	75.7

Therefore, to compare with LDA $\langle \bar{q}q \rangle = \langle \bar{q}q \rangle_0 + n_B \Sigma_N / \bar{m}$, the sigma-term is

$$\Sigma_N = \frac{\epsilon \bar{m}}{m_\sigma^2} \left(\frac{\partial m_+}{\partial \sigma} \right)_{\text{vac.}} = \frac{f_\pi m_\pi^2}{m_\sigma^2} \left(\frac{\partial m_+}{\partial \sigma} \right)_{\text{vac.}} \quad (\text{A.47})$$

Eq. (A.47) is the value of what we want which is plotted as cross symbols in Figs. A.2-A.3. Table A.1 is the table of the values of sigma-term Eq. (A.47).

A.6 Sigma-term from the nucleon mass

In PDM, a (positive-parity) nucleon mass is defined as

$$m_+ := \sqrt{m_0 + \left(\frac{g_1 + g_2}{2} \right) \sigma^2} - \frac{|g_1 - g_2|}{2} \sigma \quad (\text{A.48})$$

where m_0 is a chiral invariant mass and $g_{1,2}$ are Yukawa couplings of N_\pm and scalar mesons. In general, the sigma-term Σ_N is defined as $m_q \partial m_N / \partial m_q$. With using this expression, the sigma-term in PDM may be calculated as the following

$$\Sigma_N = \bar{m} \frac{\partial m_+}{\partial \bar{m}} = \bar{m} \frac{\partial \sigma}{\partial \bar{m}} \frac{\partial m_+}{\partial \sigma} \quad (\text{A.49})$$

which is depends on the density through σ .

$$\Sigma_N = \bar{m} \left(\frac{\partial m_+}{\partial \bar{m}} \right)_{n_B} \quad (\text{A.50})$$

$$= \bar{m} \left(\frac{\partial \sigma}{\partial \bar{m}} - \frac{\epsilon}{\chi_B} \left(\frac{\partial \sigma}{\partial \mu_B} \right)^2 \right) \frac{\partial m_+}{\partial \sigma} \quad (\text{A.51})$$

$\frac{\partial\sigma}{\partial\bar{m}}$ can be calculated from the stationary conditions as the following

$$0 = \left(\frac{\partial}{\partial\bar{m}}\right)_{\mu_B} \frac{\partial\Omega_{\text{PDM}}}{\partial\phi_i}(\vec{\phi}; \mu_B, \bar{m}) \quad (\text{A.52})$$

$$= \left[\left(\frac{\partial}{\partial\bar{m}}\right)_{\vec{\phi}, \mu_B} + \left(\frac{\partial\phi_j}{\partial\bar{m}}\right)_{\mu_B} \left(\frac{\partial}{\partial\phi_j}\right)_{\mu_B, \bar{m}} \right] \frac{\partial\Omega_{\text{PDM}}}{\partial\phi_i} \quad (\text{A.53})$$

$$= \frac{\partial^2\Omega_{\text{PDM}}}{\partial\bar{m}\partial\phi_i} + \left(\frac{\partial\phi_j}{\partial\bar{m}}\right)_{\mu_B} \frac{\partial^2\Omega_{\text{PDM}}}{\partial\phi_i\partial\phi_j} \quad (\text{A.54})$$

$$= \frac{\partial^2\Omega_{\text{PDM}}}{\partial\bar{m}\partial\vec{\phi}} + \frac{\partial^2\Omega_{\text{PDM}}}{\partial\vec{\phi}\partial\vec{\phi}} \left(\frac{\partial\vec{\phi}}{\partial\bar{m}}\right)_{\mu_B} \quad (\text{A.55})$$

$$\left(\frac{\partial\vec{\phi}}{\partial\bar{m}}\right)_{\mu_B} = - \left[\frac{\partial^2\Omega_{\text{PDM}}}{\partial\vec{\phi}\partial\vec{\phi}} \right]^{-1} \frac{\partial^2\Omega_{\text{PDM}}}{\partial\bar{m}\partial\vec{\phi}} \quad (\text{A.56})$$

In vacuum, the chiral susceptibility $\partial\sigma/\partial\bar{m}$ is calculated ¹ as

$$\left(\frac{\partial\sigma}{\partial\bar{m}}\right)_{\mu_B}^{\text{vac.}} = -\frac{1}{m_\sigma^2} \times (-\epsilon) \quad (\text{A.57})$$

Then, the sigma-term Eq. (A.49) in vacuum is

$$\Sigma_N = \frac{\epsilon\bar{m}}{m_\sigma^2} \left(\frac{\partial m_+}{\partial\sigma}\right)_{\text{vac.}} = \frac{f_\pi m_\pi^2}{m_\sigma^2} \left(\frac{\partial m_+}{\partial\sigma}\right)_{\text{vac.}} \quad (\text{A.58})$$

which is equivalent to Eq. (A.47).

A.7 Sigma-term from the energy density per nucleon

In general, the energy density is defined as the Legendre transformation of the pressure P as

$$\varepsilon := \mu_B n_B - P \quad (\text{A.59})$$

¹susceptibility \sim correlator $\sim \frac{1}{\mathbf{p}^2 + m^2} \sim \frac{1}{m^2}$

and the energy density per nucleon is expanded around $x = (n_B - n_0)/(3n_0) = 0$ and $\delta = 2n_I/n_B = 0$ as

$$\frac{\varepsilon}{n_B} = m_N - B_0 + \frac{1}{2}K_0x^2 + \delta^2(S_0 + L_0x + \mathcal{O}(x^2)) + \mathcal{O}(\delta^4) \quad (\text{A.60})$$

where $B_0 = 16$ MeV is the binding energy of a nucleon, $K_0 = 240$ MeV is the incompressibility of a nucleon, S_0 is the symmetric energy and L_0 is the slope parameter. If we regard the energy density per nucleon as the effective mass of a nucleon, the sigma-term can be calculated as

$$\Sigma_N = \bar{m} \left(\frac{\partial}{\partial \bar{m}} \right)_{n_B} \frac{\varepsilon}{n_B} \quad (\text{A.61})$$

$$= \frac{\bar{m}}{n_B} \left(\frac{\partial}{\partial \bar{m}} \right)_{n_B} (\mu_B n_B - P) \quad (\text{A.62})$$

$$= \frac{\bar{m}}{n_B} \left[\left(\frac{\partial \mu_B}{\partial \bar{m}} \right)_{n_B} n_B - \left(\frac{\partial \mu_B}{\partial \bar{m}} \right)_{n_B} \left(\frac{\partial P}{\partial \mu_B} \right)_{\bar{m}} - \left(\frac{\partial P}{\partial \bar{m}} \right)_{\mu_B} \right] \quad (\text{A.63})$$

$$= \frac{\bar{m}}{n_B} \left[- \left(\frac{\partial P}{\partial \bar{m}} \right)_{\mu_B} \right] \quad (\text{A.64})$$

$$= \frac{\bar{m}}{n_B} \epsilon (f_\pi - \sigma) \quad (\text{A.65})$$

$$= \epsilon \bar{m} \frac{f_\pi - \sigma}{n_B} \quad (\text{A.66})$$

Then we get

$$\Sigma_N = \epsilon \bar{m} \frac{f_\pi - \sigma}{n_B} = f_\pi m_\pi^2 \frac{f_\pi - \sigma}{n_B} \quad (\text{A.67})$$

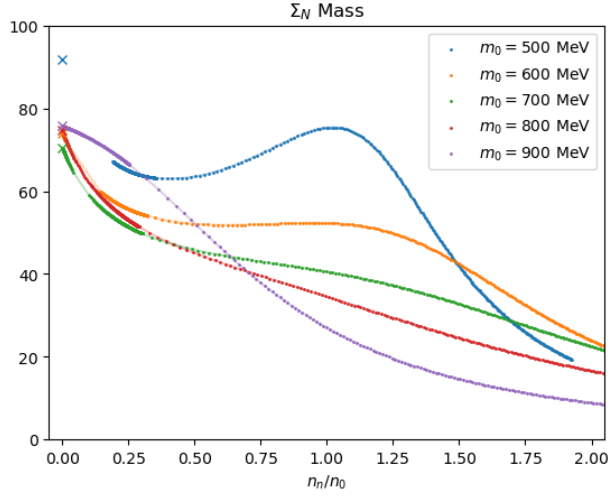
This is just equivalent to $\langle \bar{q}q \rangle^{\text{PDM}} = \langle \bar{q}q \rangle_0^{\text{PDM}} + n_B \Sigma_N / \bar{m}$. In vacuum, we can use the expression $m_\sigma^2 \tilde{\sigma} \approx (\partial m_+ / \partial \sigma)_{\text{vac.}} n_B$ as $n_B \ll n_0$. Then the sigma-term in vacuum is

$$\Sigma_N = \frac{\epsilon \bar{m}}{m_\sigma^2} \left(\frac{\partial m_+}{\partial \sigma} \right)_{\text{vac.}} = \frac{f_\pi m_\pi^2}{m_\sigma^2} \left(\frac{\partial m_+}{\partial \sigma} \right)_{\text{vac.}} \quad (\text{A.68})$$

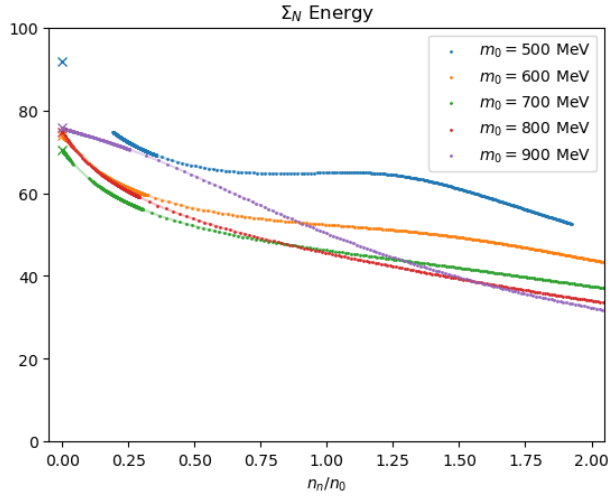
This is equivalent to Eq. (A.47).

A.8 Comparison

Fig. A.3 is comparison between two sigma-term Eq. (A.49) and Eq. (A.67).



(a) $\Sigma_N = \bar{m} \partial m_+ / \partial \bar{m}$ in Eq. (A.49).



(b) $\Sigma_N = \epsilon \bar{m} (f_\pi - \sigma) / n_B$ in Eq. (A.67).

Figure A.3: Density dependence of the sigma-term Σ_N calculated in two ways (Eq. (A.49) and Eq. (A.67)). The cross symbols are also the values calculated in Eq. (A.47).

Appendix B

Calculation of $\partial a_n / \partial J$ in Eq.(3.20)

Here, P_{H} denotes pressure for hadronic matter as a function of μ_B calculated from PDM, and P_{Q} for quark matter from NJL model. We define \vec{P} as the set of the six boundary condition values, $\partial^k P / (\partial \mu_B)^k$ ($k = 0, 1, 2$), at the boundaries $\mu_B = \mu_B^L, \mu_B^U$, as

$$\vec{P} = \left(P_{\text{H}} \Big|_{\mu_B^L}, P_{\text{Q}} \Big|_{\mu_B^U}, \frac{\partial P_{\text{H}}}{\partial \mu_B} \Big|_{\mu_B^L}, \frac{\partial P_{\text{Q}}}{\partial \mu_B} \Big|_{\mu_B^U}, \frac{\partial^2 P_{\text{H}}}{\partial \mu_B^2} \Big|_{\mu_B^L}, \frac{\partial^2 P_{\text{Q}}}{\partial \mu_B^2} \Big|_{\mu_B^U} \right)^T \quad (\text{B.1})$$

$$= (P_{\text{H}}(\mu_B^L), P_{\text{Q}}(\mu_B^U), 2n_0, 5n_0, \chi_B^{\text{H}}(\mu_B^L), \chi_B^{\text{Q}}(\mu_B^U))^T, \quad (\text{B.2})$$

which is given by the PDM and the NJL model. Since P_1 is a polynomial of μ_B , as

$$P_1 = \sum_{n=0}^5 a_n(J) \mu_B^n, \quad (\text{B.3})$$

the vector of the values of $\partial^k P_1 / (\partial \mu_B)^k$ ($k = 0, 1, 2$) at the boundaries is represented as $M\vec{a}$, where

$$\vec{a} := (a_0(J), a_1(J), a_2(J), a_3(J), a_4(J), a_5(J))^T \quad (\text{B.4})$$

and M is a matrix of μ_B^L, μ_B^U as

$$M := \begin{pmatrix} 1 & \mu_B^L & (\mu_B^L)^2 & (\mu_B^L)^3 & (\mu_B^L)^4 & (\mu_B^L)^5 \\ 1 & \mu_B^U & (\mu_B^U)^2 & (\mu_B^U)^3 & (\mu_B^U)^4 & (\mu_B^U)^5 \\ 0 & 1 & 2\mu_B^L & 3(\mu_B^L)^2 & 4(\mu_B^L)^3 & 5(\mu_B^L)^4 \\ 0 & 1 & 2\mu_B^U & 3(\mu_B^U)^2 & 4(\mu_B^U)^3 & 5(\mu_B^U)^4 \\ 0 & 0 & 2 & 6\mu_B^L & 12(\mu_B^L)^2 & 20(\mu_B^L)^3 \\ 0 & 0 & 2 & 6\mu_B^U & 12(\mu_B^U)^2 & 20(\mu_B^U)^3 \end{pmatrix}. \quad (\text{B.5})$$

Therefore, the six boundary conditions can be represented as the following one equation for matrices,

$$\vec{P} = M\vec{a} \quad \left(\Leftrightarrow \frac{\partial^k P_{\text{H(Q)}}}{(\partial\mu_B)^k} \Big|_{\mu_B^L(\mu_B^U)} = \frac{\partial^k P_1}{(\partial\mu_B)^k} \Big|_{\mu_B^L(\mu_B^U)} \right). \quad (\text{B.6})$$

Since this condition Eq.(B.6) is satisfied for arbitrary J , the derivative of a_n with respect to J can be obtained by differentiating Eq.(B.6) as

$$\frac{\partial a_n}{\partial J} = -M^{-1} \frac{\partial M}{\partial J} M^{-1} \vec{P} + M^{-1} \frac{\partial \vec{P}}{\partial J}, \quad (\text{B.7})$$

where we use an identity for matrices as

$$\frac{\partial M^{-1}}{\partial J} = -M^{-1} \frac{\partial M}{\partial J} M^{-1}, \quad (\text{B.8})$$

which can be easily shown by using: $M^{-1}M = 1$ and hence $\partial(M^{-1})M + M^{-1}\partial M = 0$.

The derivatives $\partial\vec{P}/\partial J$ and $\partial\mu_B^{L,U}/\partial J$ can be calculated as the following. Since \vec{P} is evaluated at the boundaries for arbitrary J , for example,

$$\frac{\partial}{\partial J} \left(P \Big|_{\mu_B^L} \right) = \frac{\partial\mu_B^L}{\partial J} \frac{\partial P}{\partial\mu_B} \Big|_{\mu_B^L} + \frac{\partial P}{\partial J} \Big|_{\mu_B^L}, \quad (\text{B.9})$$

$$\frac{\partial}{\partial J} \left(\frac{\partial P}{\partial\mu_B} \Big|_{\mu_B^L} \right) = \frac{\partial\mu_B^L}{\partial J} \frac{\partial^2 P}{\partial\mu_B^2} \Big|_{\mu_B^L} + \frac{\partial^2 P}{\partial J \partial\mu_B} \Big|_{\mu_B^L}, \quad (\text{B.10})$$

$$\frac{\partial}{\partial J} \left(\frac{\partial^2 P}{\partial\mu_B^2} \Big|_{\mu_B^L} \right) = \frac{\partial\mu_B^L}{\partial J} \frac{\partial^3 P}{\partial\mu_B^3} \Big|_{\mu_B^L} + \frac{\partial^3 P}{\partial J \partial\mu_B^2} \Big|_{\mu_B^L}. \quad (\text{B.11})$$

Eq.(B.10) equals zero, since the values of density at the boundaries are fixed for any J , and therefore,

$$\frac{\partial \mu_B^L}{\partial J} = - \frac{\partial^2 P}{\partial J \partial \mu_B} \Big|_{\mu_B^L} / \frac{\partial^2 P}{\partial \mu_B^2} \Big|_{\mu_B^L}. \quad (\text{B.12})$$

Moreover, $\partial^{k+1} P / \partial J (\partial \mu_B)^k = -\partial^k \phi / (\partial \mu_B)^k$ is determined from the derivation of the gap equation, for example,

$$0 = \frac{\partial}{\partial J} \left(\frac{\partial \Omega}{\partial \phi} \Big|_{\phi_*} \right) = \frac{\partial^2 \Omega}{\partial \phi^2} \Big|_{\phi_*} \frac{\partial \phi_*}{\partial J} + \frac{\partial^2 \Omega}{\partial J \partial \phi} \Big|_{\phi_*} \quad (\text{B.13})$$

and then,

$$\frac{\partial \phi_*}{\partial J} = - \left(\frac{\partial^2 \Omega}{\partial \phi^2} \Big|_{\phi_*} \right)^{-1} \frac{\partial^2 \Omega}{\partial J \partial \phi} \Big|_{\phi_*} \quad (\text{B.14})$$

where ϕ_* is the solution of the gap equation. Note that, the mean field variables ϕ may be a vector, hence $\partial^2 \Omega / \partial J \partial \phi$ may be a vector and $\partial^2 \Omega / \partial \phi \partial \phi$ may be a matrix.

Appendix C

Hellmann–Feynman Theorem

We show the theorem for perturbation of an operator, called Hellmann–Feynman theorem, and its relation to the pseudo-inverse notation.

C.1 Perturbation of Hamiltonian

Let $H = H(\lambda)$ be a Hamiltonian with a parameter λ , and $|n\rangle = |n; \lambda\rangle$ be an eigenstate with an energy eigenvalue $E_n = E_n(\lambda)$. Especially, the expansion with respect to λ is defined as

$$H(\lambda) = H_0 + \lambda H_1 + \frac{1}{2}\lambda^2 H_2 + \dots \quad (\text{C.1})$$

$$|n; \lambda\rangle = |n^{(0)}\rangle + \lambda |n^{(1)}\rangle + \dots \quad (\text{C.2})$$

$$E_n(\lambda) = E_n^{(0)} + \lambda E_n^{(1)} + \dots . \quad (\text{C.3})$$

By definition, the following equation is valid for any λ ,

$$H |n\rangle = E_n |n\rangle . \quad (\text{C.4})$$

Differentiating the both side, multiplying $\langle m|$ from left, and using $\langle m| H = \langle m| E_m$, we obtain

$$\langle m| \frac{\partial H}{\partial \lambda} |n\rangle = \frac{\partial E_n}{\partial \lambda} \delta_{m,n} + \langle m| (E_n - E_m) \frac{\partial |n\rangle}{\partial \lambda} . \quad (\text{C.5})$$

When $m = n$, taking $\lambda \rightarrow 0$, it is just the Hellmann-Feynman theorem,

$$\frac{\partial E_n}{\partial \lambda} = \langle n| \frac{\partial H}{\partial \lambda} |n\rangle \quad \rightarrow \quad E_n^{(1)} = \langle n^{(0)}| H_1 |n^{(0)}\rangle , \quad (\text{C.6})$$

which means that we can get the derivative of an eigenvalue by just differentiating the operator.

If $m \neq n$ in Eq.(C.5), the following equation is obtained,

$$\langle m | \frac{\partial |n\rangle}{\partial \lambda} = \frac{\langle m | \frac{\partial H}{\partial \lambda} |n\rangle}{E_n - E_m}, \quad (\text{C.7})$$

which is the first order perturbation of the eigenstate. Differentiating the orthonormal condition $\langle m | n \rangle = \delta_{m,n}$, we also get the following identity as

$$\frac{\partial \langle m |}{\partial \lambda} |n\rangle + \langle m | \frac{\partial |n\rangle}{\partial \lambda} = 0. \quad (\text{C.8})$$

Using Eqs.(C.7) and (C.8), we obtain the second-order derivative as the following. Here, the Hamiltonian has two parameters λ_1 and λ_2 .

$$\frac{\partial^2 E_n}{\partial \lambda_1 \partial \lambda_2} = \frac{\partial}{\partial \lambda_1} \left(\langle n | \frac{\partial H}{\partial \lambda_2} |n\rangle \right) \quad (\text{C.9})$$

$$= \frac{\partial \langle n |}{\partial \lambda_1} \frac{\partial H}{\partial \lambda_2} |n\rangle + \langle n | \frac{\partial H}{\partial \lambda_2} \frac{\partial |n\rangle}{\partial \lambda_1} + \langle n | \frac{\partial^2 H}{\partial \lambda_1 \partial \lambda_2} |n\rangle \quad (\text{C.10})$$

$$= \sum_l \left(\frac{\partial \langle n |}{\partial \lambda_1} |l\rangle \langle l | \frac{\partial H}{\partial \lambda_2} |n\rangle + \langle n | \frac{\partial H}{\partial \lambda_2} |l\rangle \langle l | \frac{\partial |n\rangle}{\partial \lambda_1} \right) + \langle n | \frac{\partial^2 H}{\partial \lambda_1 \partial \lambda_2} |n\rangle \quad (\text{C.11})$$

$$= \sum_l \left(\frac{\langle n | \frac{\partial H}{\partial \lambda_1} |l\rangle}{E_n - E_l} \langle l | \frac{\partial H}{\partial \lambda_2} |n\rangle + \langle n | \frac{\partial H}{\partial \lambda_2} |l\rangle \frac{\langle l | \frac{\partial H}{\partial \lambda_1} |n\rangle}{E_n - E_l} \right) + \langle n | \frac{\partial^2 H}{\partial \lambda_1 \partial \lambda_2} |n\rangle \quad (\text{C.12})$$

$$= \sum_l \frac{\langle n | \frac{\partial H}{\partial \lambda_1} |l\rangle \langle l | \frac{\partial H}{\partial \lambda_2} |n\rangle + \langle n | \frac{\partial H}{\partial \lambda_2} |l\rangle \langle l | \frac{\partial H}{\partial \lambda_1} |n\rangle}{E_n - E_l} + \langle n | \frac{\partial^2 H}{\partial \lambda_1 \partial \lambda_2} |n\rangle. \quad (\text{C.13})$$

C.2 Pseudoinverse

Next, we explain the relation to the pseudoinverse expression. A Moore–Penrose pseudoinverse A^+ for an arbitrary matrix A is defined with the following conditions:

$$(i) AA^+A = A, \quad (\text{C.14})$$

$$(ii) A^+ A A^+ = A^+, \quad (C.15)$$

$$(iii) (A A^+)^{\dagger} = A A^+, \quad (C.16)$$

$$(iv) (A^+ A)^{\dagger} = A^+ A. \quad (C.17)$$

Briefly speaking, when A has a nonzero eigenvalue, A^+ has an eigenvalue of its reciprocal, and when A has an eigenvalue of zero, A^+ has also zero, i.e. when $A = \text{diag}(a_1, a_2, 0)$ with $a_1 \neq 0 \neq a_2$, then $A^+ = \text{diag}(1/a_1, 1/a_2, 0)$. Note that, when A is hermitian, then A and A^+ are commutable, $A A^+ = A^+ A$.

Let $H = H(\lambda)$ is an hermitian matrix with a parameter λ , and $U = (\cdots, \vec{u}_n, \cdots)$ is its diagonalizing unitary matrix with a diagonal matrix $D = \text{diag}(\cdots, E_n, \cdots)$ as

$$H U = U D. \quad (C.18)$$

Differentiating the both side, and multiplying U^{\dagger} from left, we obtain

$$U^{\dagger} \frac{\partial H}{\partial \lambda} U = \frac{\partial D}{\partial \lambda} + [U^{\dagger} \frac{\partial U}{\partial \lambda}, D], \quad (C.19)$$

where $[A, B] = AB - BA$ is the commutation bracket. Because the term $[U^{\dagger} \frac{\partial U}{\partial \lambda}, D]$ has no diagonal part, this equation Eq.(C.19) clearly corresponds to Eq.(C.5). Therefore, the Hellmann-Feynman theorem reads

$$\frac{\partial D_{i,i}}{\partial \lambda} = \left(U^{\dagger} \frac{\partial H}{\partial \lambda} U \right)_{i,i}. \quad (C.20)$$

Starting the eigenvalue equation

$$H \vec{u}_n = E_n \vec{u}_n, \quad (C.21)$$

we obtain

$$\frac{\partial H}{\partial \lambda} \vec{u}_n + (H - E_n) \frac{\partial \vec{u}_n}{\partial \lambda} = \frac{\partial E_n}{\partial \lambda} \vec{u}_n, \quad (C.22)$$

and therefore we obtain the derivative of the eigenvector as

$$\frac{\partial \vec{u}_n}{\partial \lambda} = -(H - E_n)^+ \frac{\partial H}{\partial \lambda} \vec{u}_n, \quad \xrightarrow{\lambda \rightarrow 0} \quad \vec{u}_n^{(1)} = -(H_0 - E_n^{(0)})^+ H_1 \vec{u}_n^{(0)}. \quad (C.23)$$

Here, we use the following two relations: $(H - E_n)^+ \vec{u}_n = 0$ and $(H - E_n)^+ (H - E_n) \frac{\partial \vec{u}_n}{\partial \lambda} = \frac{\partial \vec{u}_n}{\partial \lambda}$. First one can be shown by definition,

$$(H - E_n)^+ \vec{u}_n = (H - E_n)^+ (H - E_n) (H - E_n)^+ \vec{u}_n \quad (C.24)$$

$$= (H - E_n)^+(H - E_n)^+(H - E_n)\vec{u}_n \quad (\text{C.25})$$

$$= 0, \quad (\text{C.26})$$

or briefly, we can say that the pseudoinverse of the eigenvalue 0 is just 0. Second one can be shown as follow, assuming \vec{u}_n is a real vector for simplicity. Two vectors \vec{u}_n and $\frac{\partial \vec{u}_n}{\partial \lambda}$ are linearly independent since the vector is normalized. Because $(H - E_n)\vec{u}_n = 0$, all of the column vectors in $H - E_n$ are linearly independent of \vec{u} . Therefore, there exists a coefficient vector \vec{c} such that $\frac{\partial \vec{u}_n}{\partial \lambda} = (H - E_n)\vec{c}$ and

$$\frac{\partial \vec{u}_n}{\partial \lambda} = (H - E_n)\vec{c} \quad (\text{C.27})$$

$$= (H - E_n)(H - E_n)^+(H - E_n)\vec{c} \quad (\text{C.28})$$

$$= (H - E_n)(H - E_n)^+\frac{\partial \vec{u}_n}{\partial \lambda}. \quad (\text{C.29})$$

Then, $(H - E_n)(H - E_n)^+\frac{\partial \vec{u}_n}{\partial \lambda} = \frac{\partial \vec{u}_n}{\partial \lambda}$ is shown. Similarly, $(H - E_n)^+(H - E_n)\frac{\partial \vec{u}_n}{\partial \lambda} = \frac{\partial \vec{u}_n}{\partial \lambda}$ can be shown.

Using Eq.(C.23), we can calculate the higher-order derivative of the eigenvalues in matrix notation.

Bibliography

- [1] Takuya Minamikawa, Toru Kojo, and Masayasu Harada. Quark-hadron crossover equations of state for neutron stars: constraining the chiral invariant mass in a parity doublet model. Phys. Rev. C, 103(4):045205, 2021.
- [2] Takuya Minamikawa, Toru Kojo, and Masayasu Harada. Chiral condensates for neutron stars in hadron-quark crossover: From a parity doublet nucleon model to a Nambu–Jona-Lasinio quark model. Phys. Rev. C, 104(6):065201, 2021.
- [3] Yoichiro Nambu and G. Jona-Lasinio. Dynamical Model of Elementary Particles Based on an Analogy with Superconductivity. 1. Phys. Rev., 122:345–358, 1961.
- [4] Yoichiro Nambu and G. Jona-Lasinio. DYNAMICAL MODEL OF ELEMENTARY PARTICLES BASED ON AN ANALOGY WITH SUPERCONDUCTIVITY. II. Phys. Rev., 124:246–254, 1961.
- [5] Carleton E. Detar and Teiji Kunihiro. Linear σ Model With Parity Doubling. Phys. Rev. D, 39:2805, 1989.
- [6] Gert Aarts, Chris Allton, Simon Hands, Benjamin Jäger, Chrisanthi Praki, and Jon-Ivar Skullerud. Nucleons and parity doubling across the deconfinement transition. Phys. Rev. D, 92(1):014503, 2015.
- [7] Gert Aarts, Chris Allton, Davide De Boni, Simon Hands, Benjamin Jäger, Chrisanthi Praki, and Jon-Ivar Skullerud. Light baryons below and above the deconfinement transition: medium effects and parity doubling. JHEP, 06:034, 2017.

- [8] Gert Aarts, Chris Allton, Davide de Boni, Simon Hands, Benjamin Jäger, Chrisanthi Praki, and Jon-Ivar Skullerud. Baryons in the plasma: in-medium effects and parity doubling. EPJ Web Conf., 171:14005, 2018.
- [9] Gert Aarts, Chris Allton, Davide De Boni, and Benjamin Jäger. Hyperons in thermal QCD: A lattice view. Phys. Rev. D, 99(7):074503, 2019.
- [10] Gert Aarts, Chris Allton, Davide de Boni, Jonas Glesaaen, Simon Hands, Benjamin Jäger, and Jon-Ivar Skullerud. Hyperons in thermal QCD from the lattice. Springer Proc. Phys., 250:29–35, 2020.
- [11] D. Jido, Y. Nemoto, M. Oka, and A. Hosaka. Chiral symmetry for positive and negative parity nucleons. Nucl. Phys. A, 671:471–480, 2000.
- [12] D. Jido, T. Hatsuda, and T. Kunihiro. Chiral symmetry realization for even parity and odd parity baryon resonances. Phys. Rev. Lett., 84:3252, 2000.
- [13] Daisuke Jido, Makoto Oka, and Atsushi Hosaka. Chiral symmetry of baryons. Prog. Theor. Phys., 106:873–908, 2001.
- [14] K. Nagata, A. Hosaka, and V. Dmitrasinovic. πN and $\pi \pi N$ Couplings of the $\Delta(1232)$ and its Chiral Partners. Phys. Rev. Lett., 101:092001, 2008.
- [15] Susanna Gallas, Francesco Giacosa, and Dirk H. Rischke. Vacuum phenomenology of the chiral partner of the nucleon in a linear sigma model with vector mesons. Phys. Rev. D, 82:014004, 2010.
- [16] Susanna Gallas and Francesco Giacosa. Mirror versus naive assignment in chiral models for the nucleon. Int. J. Mod. Phys. A, 29(17):1450098, 2014.
- [17] P. B. Demorest, T. Pennucci, S. M. Ransom, M. S. E. Roberts, and J. W. T. Hessels. A two-solar-mass neutron star measured using Shapiro delay. Nature, 467(7319):1081–1083, Oct 2010.

- [18] B. P. Abbott et al. GW170817: Observation of Gravitational Waves from a Binary Neutron Star Inspiral. Phys. Rev. Lett., 119(16):161101, 2017.
- [19] B. P. Abbott et al. GW170817: Measurements of neutron star radii and equation of state. Phys. Rev. Lett., 121(16):161101, 2018.
- [20] B. P. Abbott et al. Multi-messenger Observations of a Binary Neutron Star Merger. Astrophys. J. Lett., 848(2):L12, 2017.
- [21] M. C. Miller et al. PSR J0030+0451 Mass and Radius from *NICER* Data and Implications for the Properties of Neutron Star Matter. Astrophys. J. Lett., 887(1):L24, 2019.
- [22] Thomas E. Riley et al. A *NICER* View of PSR J0030+0451: Millisecond Pulsar Parameter Estimation. Astrophys. J. Lett., 887(1):L21, 2019.
- [23] Thomas E. Riley et al. A *NICER* View of the Massive Pulsar PSR J0740+6620 Informed by Radio Timing and XMM-Newton Spectroscopy. Astrophys. J. Lett., 918(2):L27, 2021.
- [24] M. C. Miller et al. The Radius of PSR J0740+6620 from *NICER* and XMM-Newton Data. Astrophys. J. Lett., 918(2):L28, 2021.
- [25] T. Hatsuda and M. Prakash. Parity Doubling of the Nucleon and First Order Chiral Transition in Dense Matter. Phys. Lett. B, 224:11–15, 1989.
- [26] D. Zschiesche, L. Tolos, Jurgen Schaffner-Bielich, and Robert D. Pisarski. Cold, dense nuclear matter in a SU(2) parity doublet model. Phys. Rev. C, 75:055202, 2007.
- [27] V. Dexheimer, S. Schramm, and D. Zschiesche. Nuclear matter and neutron stars in a parity doublet model. Phys. Rev. C, 77:025803, 2008.
- [28] V. Dexheimer, G. Pagliara, L. Tolos, J. Schaffner-Bielich, and S. Schramm. Neutron stars within the SU(2) parity doublet model. Eur. Phys. J. A, 38:105–113, 2008.

- [29] Chihiro Sasaki and Igor Mishustin. Thermodynamics of dense hadronic matter in a parity doublet model. Phys. Rev. C, 82:035204, 2010.
- [30] Chihiro Sasaki, Hyun Kyu Lee, Won-Gi Paeng, and Mannque Rho. Conformal anomaly and the vector coupling in dense matter. Phys. Rev. D, 84:034011, 2011.
- [31] Susanna Gallas, Francesco Giacosa, and Giuseppe Pagliara. Nuclear matter within a dilatation-invariant parity doublet model: the role of the tetraquark at nonzero density. Nucl. Phys. A, 872:13–24, 2011.
- [32] Won-Gi Paeng, Hyun Kyu Lee, Mannque Rho, and Chihiro Sasaki. Dilaton-Limit Fixed Point in Hidden Local Symmetric Parity Doublet Model. Phys. Rev. D, 85:054022, 2012.
- [33] J. Steinheimer, S. Schramm, and H. Stocker. The hadronic SU(3) Parity Doublet Model for Dense Matter, its extension to quarks and the strange equation of state. Phys. Rev. C, 84:045208, 2011.
- [34] V. Dexheimer, J. Steinheimer, R. Negreiros, and S. Schramm. Hybrid Stars in an SU(3) parity doublet model. Phys. Rev. C, 87(1):015804, 2013.
- [35] Won-Gi Paeng, Hyun Kyu Lee, Mannque Rho, and Chihiro Sasaki. Interplay between ω -nucleon interaction and nucleon mass in dense baryonic matter. Phys. Rev. D, 88:105019, 2013.
- [36] Achim Heinz, Francesco Giacosa, and Dirk H. Rischke. Chiral density wave in nuclear matter. Nucl. Phys. A, 933:34–42, 2015.
- [37] Yuichi Motohiro, Youngman Kim, and Masayasu Harada. Asymmetric nuclear matter in a parity doublet model with hidden local symmetry. Phys. Rev. C, 92(2):025201, 2015. [Erratum: Phys.Rev.C 95, 059903 (2017)].
- [38] Sanjin Benic, Igor Mishustin, and Chihiro Sasaki. Effective model for the QCD phase transitions at finite baryon density. Phys. Rev. D, 91(12):125034, 2015.
- [39] A. Mukherjee, J. Steinheimer, and S. Schramm. Higher-order baryon number susceptibilities: interplay between the chiral and the nuclear liquid-gas transitions. Phys. Rev. C, 96(2):025205, 2017.

- [40] A. Mukherjee, S. Schramm, J. Steinheimer, and V. Dexheimer. The application of the Quark-Hadron Chiral Parity-Doublet Model to neutron star matter. Astron. Astrophys., 608:A110, 2017.
- [41] Daiki Suenaga. Examination of $N^*(1535)$ as a probe to observe the partial restoration of chiral symmetry in nuclear matter. Phys. Rev. C, 97(4):045203, 2018.
- [42] Yusuke Takeda, Youngman Kim, and Masayasu Harada. Catalysis of partial chiral symmetry restoration by Δ matter. Phys. Rev. C, 97(6):065202, 2018.
- [43] Michał Marczenko and Chihiro Sasaki. Net-baryon number fluctuations in the Hybrid Quark-Meson-Nucleon model at finite density. Phys. Rev. D, 97(3):036011, 2018.
- [44] Won-Gi Paeng, Thomas T. S. Kuo, Hyun Kyu Lee, Yong-Liang Ma, and Mannque Rho. Scale-invariant hidden local symmetry, topology change, and dense baryonic matter. II. Phys. Rev. D, 96(1):014031, 2017.
- [45] Michał Marczenko, David Blaschke, Krzysztof Redlich, and Chihiro Sasaki. Chiral symmetry restoration by parity doubling and the structure of neutron stars. Phys. Rev. D, 98(10):103021, 2018.
- [46] Hiroaki Abuki, Yusuke Takeda, and Masayasu Harada. Dual chiral density waves in nuclear matter. EPJ Web Conf., 192:00020, 2018.
- [47] Yusuke Takeda, Hiroaki Abuki, and Masayasu Harada. Novel dual chiral density wave in nuclear matter based on a parity doublet structure. Phys. Rev. D, 97(9):094032, 2018.
- [48] Takahiro Yamazaki and Masayasu Harada. Constraint to chiral invariant masses of nucleons from GW170817 in an extended parity doublet model. Phys. Rev. C, 100(2):025205, 2019.
- [49] Masayasu Harada and Takahiro Yamazaki. Charmed Mesons in Nuclear Matter Based on Chiral Effective Models. JPS Conf. Proc., 26:024001, 2019.

- [50] Michał Marczenko, David Blaschke, Krzysztof Redlich, and Chihiro Sasaki. Parity Doubling and the Dense Matter Phase Diagram under Constraints from Multi-Messenger Astronomy. Universe, 5(8):180, 2019.
- [51] Masayasu Harada. Dense nuclear matter based on a chiral model with parity doublet structure. In 18th International Conference on Hadron Spectroscopy and Structure, pages 661–666, 2020.
- [52] Michał Marczenko, David Blaschke, Krzysztof Redlich, and Chihiro Sasaki. Toward a unified equation of state for multi-messenger astronomy. Astron. Astrophys., 643:A82, 2020.
- [53] Michał Marczenko. Speed of sound and quark confinement inside neutron stars. Eur. Phys. J. ST, 229(22-23):3651–3661, 2020.
- [54] Michał Marczenko. Hybrid quark-hadron equation of state for multi-messenger astronomy. In Criticality in QCD and the Hadron Resonance Gas, 10 2020.
- [55] Michał Marczenko, Krzysztof Redlich, and Chihiro Sasaki. Interplay between chiral dynamics and repulsive interactions in hot hadronic matter. Phys. Rev. D, 103(5):054035, 2021.
- [56] Michał Marczenko, Krzysztof Redlich, and Chihiro Sasaki. Reconciling Multi-messenger Constraints with Chiral Symmetry Restoration. Astrophys. J. Lett., 925(2):L23, 2022.
- [57] Michał Marczenko, Krzysztof Redlich, and Chihiro Sasaki. Chiral symmetry restoration and Δ matter formation in neutron stars. Phys. Rev. D, 105(10):103009, 2022.
- [58] Kota Masuda, Tetsuo Hatsuda, and Tatsuyuki Takatsuka. Hadron-Quark Crossover and Massive Hybrid Stars with Strangeness. Astrophys. J., 764:12, 2013.
- [59] Kota Masuda, Tetsuo Hatsuda, and Tatsuyuki Takatsuka. Hadron-quark crossover and massive hybrid stars. PTEP, 2013(7):073D01, 2013.

- [60] Gordon Baym, Tetsuo Hatsuda, Toru Kojo, Philip D. Powell, Yifan Song, and Tatsuyuki Takatsuka. From hadrons to quarks in neutron stars: a review. Rept. Prog. Phys., 81(5):056902, 2018.
- [61] Gordon Baym, Shun Furusawa, Tetsuo Hatsuda, Toru Kojo, and Hajime Togashi. New Neutron Star Equation of State with Quark-Hadron Crossover. Astrophys. J., 885:42, 2019.
- [62] Tetsuo Hatsuda and Teiji Kunihiro. QCD phenomenology based on a chiral effective Lagrangian. Phys. Rept., 247:221–367, 1994.
- [63] Szabolcs Borsanyi, Zoltan Fodor, Christian Hoelbling, Sandor D. Katz, Stefan Krieg, and Kalman K. Szabo. Full result for the QCD equation of state with 2+1 flavors. Phys. Lett. B, 730:99–104, 2014.
- [64] A. Bazavov et al. Equation of state in (2+1)-flavor QCD. Phys. Rev. D, 90:094503, 2014.
- [65] V. Vovchenko, D. V. Anchishkin, and M. I. Gorenstein. Hadron Resonance Gas Equation of State from Lattice QCD. Phys. Rev. C, 91(2):024905, 2015.
- [66] E. E. Kolomeitsev, K. A. Maslov, and D. N. Voskresensky. Hyperon puzzle and the RMF model with scaled hadron masses and coupling constants. J. Phys. Conf. Ser., 668(1):012064, 2016.
- [67] Ingo Tews, James M. Lattimer, Akira Ohnishi, and Evgeni E. Kolomeitsev. Symmetry Parameter Constraints from a Lower Bound on Neutron-matter Energy. Astrophys. J., 848(2):105, 2017.
- [68] C. Drischler, R. J. Furnstahl, J. A. Melendez, and D. R. Phillips. How Well Do We Know the Neutron-Matter Equation of State at the Densities Inside Neutron Stars? A Bayesian Approach with Correlated Uncertainties. Phys. Rev. Lett., 125(20):202702, 2020.
- [69] Bao-An Li, Bao-Jun Cai, Wen-Jie Xie, and Nai-Bo Zhang. Progress in Constraining Nuclear Symmetry Energy Using Neutron Star Observables Since GW170817. Universe, 7(6):182, 2021.
- [70] H. T. Cromartie et al. Relativistic Shapiro delay measurements of an extremely massive millisecond pulsar. Nature Astron., 4(1):72–76, 2019.

- [71] Toru Kojo. QCD equations of state and speed of sound in neutron stars. AAPPS Bull., 31(1):11, 2021.
- [72] Zaven Arzoumanian et al. The NANOGrav 11-year Data Set: High-precision timing of 45 Millisecond Pulsars. Astrophys. J. Suppl., 235(2):37, 2018.
- [73] Emmanuel Fonseca et al. The NANOGrav Nine-year Data Set: Mass and Geometric Measurements of Binary Millisecond Pulsars. Astrophys. J., 832(2):167, 2016.
- [74] Paul Demorest, Tim Pennucci, Scott Ransom, Mallory Roberts, and Jason Hessels. Shapiro Delay Measurement of A Two Solar Mass Neutron Star. Nature, 467:1081–1083, 2010.
- [75] John Antoniadis et al. A Massive Pulsar in a Compact Relativistic Binary. Science, 340:6131, 2013.
- [76] E. Fonseca et al. Refined Mass and Geometric Measurements of the High-mass PSR J0740+6620. Astrophys. J. Lett., 915(1):L12, 2021.
- [77] G. Raaijmakers, S. K. Greif, K. Hebeler, T. Hinderer, S. Nisanke, A. Schwenk, T. E. Riley, A. L. Watts, J. M. Lattimer, and W. C. G. Ho. Constraints on the Dense Matter Equation of State and Neutron Star Properties from NICER’s Mass–Radius Estimate of PSR J0740+6620 and Multimessenger Observations. Astrophys. J. Lett., 918(2):L29, 2021.
- [78] J. D. Walecka. A Theory of highly condensed matter. Annals Phys., 83:491–529, 1974.
- [79] Brian D. Serot and John Dirk Walecka. The Relativistic Nuclear Many Body Problem. Adv. Nucl. Phys., 16:1–327, 1986.
- [80] Brian D. Serot and John Dirk Walecka. Recent progress in quantum hydrodynamics. Int. J. Mod. Phys. E, 6:515–631, 1997.
- [81] Takahiro Yamazaki and Masayasu Harada. Chiral partner structure of light nucleons in an extended parity doublet model. Phys. Rev. D, 99(3):034012, 2019.

- [82] Toru Kojo, Philip D. Powell, Yifan Song, and Gordon Baym. Phenomenological QCD equation of state for massive neutron stars. Phys. Rev. D, 91(4):045003, 2015.
- [83] Masakiyo Kitazawa, Tomoi Koide, Teiji Kunihiro, and Yukio Nemoto. Chiral and color superconducting phase transitions with vector interaction in a simple model. Prog. Theor. Phys., 108(5):929–951, 2002. [Erratum: Prog.Theor.Phys. 110, 185–186 (2003)].
- [84] Nino M. Bratovic, Tetsuo Hatsuda, and Wolfram Weise. Role of Vector Interaction and Axial Anomaly in the PNJL Modeling of the QCD Phase Diagram. Phys. Lett. B, 719:131–135, 2013.
- [85] Mark G. Alford, Andreas Schmitt, Krishna Rajagopal, and Thomas Schäfer. Color superconductivity in dense quark matter. Rev. Mod. Phys., 80:1455–1515, 2008.
- [86] Kota Masuda, Tetsuo Hatsuda, and Tatsuyuki Takatsuka. Hyperon Puzzle, Hadron-Quark Crossover and Massive Neutron Stars. Eur. Phys. J. A, 52(3):65, 2016.
- [87] Kenji Fukushima and Toru Kojo. The Quarkyonic Star. Astrophys. J., 817(2):180, 2016.
- [88] Masako Bando, Taichiro Kugo, and Koichi Yamawaki. Nonlinear Realization and Hidden Local Symmetries. Phys. Rept., 164:217–314, 1988.
- [89] Masayasu Harada and Koichi Yamawaki. Hidden local symmetry at loop: A New perspective of composite gauge boson and chiral phase transition. Phys. Rept., 381:1–233, 2003.
- [90] Michael Buballa. NJL model analysis of quark matter at large density. Phys. Rept., 407:205–376, 2005.
- [91] Richard C. Tolman. Static solutions of Einstein’s field equations for spheres of fluid. Phys. Rev., 55:364–373, 1939.
- [92] J. R. Oppenheimer and G. M. Volkoff. On massive neutron cores. Phys. Rev., 55:374–381, 1939.

- [93] Gordon Baym, Christopher Pethick, and Peter Sutherland. The Ground state of matter at high densities: Equation of state and stellar models. *Astrophys. J.*, 170:299–317, 1971.
- [94] Soumi De, Daniel Finstad, James M. Lattimer, Duncan A. Brown, Edo Berger, and Christopher M. Biwer. Tidal Deformabilities and Radii of Neutron Stars from the Observation of GW170817. *Phys. Rev. Lett.*, 121(9):091102, 2018. [Erratum: *Phys.Rev.Lett.* 121, 259902 (2018)].
- [95] David Radice, Albino Perego, Francesco Zappa, and Sebastiano Bernuzzi. GW170817: Joint Constraint on the Neutron Star Equation of State from Multimessenger Observations. *Astrophys. J. Lett.*, 852(2):L29, 2018.
- [96] Yifan Song, Gordon Baym, Tetsuo Hatsuda, and Toru Kojo. Effective repulsion in dense quark matter from nonperturbative gluon exchange. *Phys. Rev. D*, 100(3):034018, 2019.
- [97] Philipp Gubler and Daisuke Satow. Recent Progress in QCD Condensate Evaluations and Sum Rules. *Prog. Part. Nucl. Phys.*, 106:1–67, 2019.
- [98] J. Gasser, H. Leutwyler, and M. E. Sainio. Sigma term update. *Phys. Lett. B*, 253:252–259, 1991.
- [99] N. Kaiser, P. de Homont, and W. Weise. In-medium chiral condensate beyond linear density approximation. *Phys. Rev. C*, 77:025204, 2008.
- [100] N. Kaiser and W. Weise. Chiral condensate in neutron matter. *Phys. Lett. B*, 671:25–29, 2009.
- [101] Matthias Drews and Wolfram Weise. Functional renormalization group studies of nuclear and neutron matter. *Prog. Part. Nucl. Phys.*, 93:69–107, 2017.
- [102] F. Karsch, K. Redlich, and A. Tawfik. Thermodynamics at nonzero baryon number density: A Comparison of lattice and hadron resonance gas model calculations. *Phys. Lett. B*, 571:67–74, 2003.
- [103] Anton Andronic, Peter Braun-Munzinger, Krzysztof Redlich, and Johanna Stachel. Decoding the phase structure of QCD via particle production at high energy. *Nature*, 561(7723):321–330, 2018.

- [104] Edward V. Shuryak. Two Scales and Phase Transitions in Quantum Chromodynamics. Phys. Lett. B, 107:103–105, 1981.
- [105] Aneesh Manohar and Howard Georgi. Chiral Quarks and the Nonrelativistic Quark Model. Nucl. Phys. B, 234:189–212, 1984.
- [106] Daiki Suenaga and Toru Kojo. Gluon propagator in two-color dense QCD: Massive Yang-Mills approach at one-loop. Phys. Rev. D, 100(7):076017, 2019.
- [107] A. De Rujula, Howard Georgi, and S. L. Glashow. Hadron Masses in a Gauge Theory. Phys. Rev. D, 12:147–162, 1975.
- [108] Aaron Park, Woosung Park, and Su Hounng Lee. Tribaryon configurations and the inevitable three nucleon repulsions at short distance. Phys. Rev. D, 98(3):034001, 2018.
- [109] Aaron Park, Su Hounng Lee, Takashi Inoue, and Tetsuo Hatsuda. Baryon–baryon interactions at short distances: constituent quark model meets lattice QCD. Eur. Phys. J. A, 56(3):93, 2020.
- [110] Thomas Schäfer and Edward V. Shuryak. Instantons in QCD. Rev. Mod. Phys., 70:323–426, 1998.
- [111] T. H. R. Skyrme. A Nonlinear field theory. Proc. Roy. Soc. Lond. A, 260:127–138, 1961.
- [112] Gregory S. Adkins, Chiara R. Nappi, and Edward Witten. Static Properties of Nucleons in the Skyrme Model. Nucl. Phys. B, 228:552, 1983.
- [113] Aneesh V. Manohar. Equivalence of the Chiral Soliton and Quark Models in Large N. Nucl. Phys. B, 248:19, 1984.
- [114] S. Kahana, G. Ripka, and V. Soni. Soliton with Valence Quarks in the Chiral Invariant Sigma Model. Nucl. Phys. A, 415:351–364, 1984.
- [115] I. Zahed and G. E. Brown. The Skyrme Model. Phys. Rept., 142:1–102, 1986.
- [116] Dmitri Diakonov, V. Yu. Petrov, and P. V. Pobylitsa. A Chiral Theory of Nucleons. Nucl. Phys. B, 306:809, 1988.

- [117] Hiroyuki Hata, Tadakatsu Sakai, Shigeki Sugimoto, and Shinichiro Yamato. Baryons from instantons in holographic QCD. Prog. Theor. Phys., 117:1157, 2007.
- [118] Kanabu Nawa, Hideo Suganuma, and Toru Kojo. Baryons in holographic QCD. Phys. Rev. D, 75:086003, 2007.
- [119] Edward Witten. Nonabelian Bosonization in Two-Dimensions. Commun. Math. Phys., 92:455–472, 1984.
- [120] Edward Witten. Chiral Symmetry, the $1/n$ Expansion, and the $SU(N)$ Thirring Model. Nucl. Phys. B, 145:110–118, 1978.
- [121] Ian Affleck. On the Realization of Chiral Symmetry in $(1+1)$ -dimensions. Nucl. Phys. B, 265:448–468, 1986.
- [122] Ian Affleck. Exact Critical Exponents for Quantum Spin Chains, Non-linear Sigma Models at $\Theta = \pi$ and the Quantum Hall Effect. Nucl. Phys. B, 265:409–447, 1986.
- [123] Verena Schon and Michael Thies. Emergence of Skyrme crystal in Gross-Neveu and 't Hooft models at finite density. Phys. Rev. D, 62:096002, 2000.
- [124] Barak Bringoltz. Chiral crystals in strong-coupling lattice QCD at nonzero chemical potential. JHEP, 03:016, 2007.
- [125] Toru Kojo. Chiral Spirals from Noncontinuous Chiral Symmetry: The Gross-Neveu model results. Phys. Rev. D, 90(6):065030, 2014.
- [126] Toru Kojo. A $(1+1)$ dimensional example of Quarkyonic matter. Nucl. Phys. A, 877:70–94, 2012.
- [127] Yong-Liang Ma, Masayasu Harada, Hyun Kyu Lee, Yongseok Oh, Byung-Yoon Park, and Mannque Rho. Dense baryonic matter in the hidden local symmetry approach: Half-skyrmions and nucleon mass. Phys. Rev. D, 88(1):014016, 2013. [Erratum: Phys.Rev.D 88, 079904 (2013)].
- [128] Masayasu Harada, Hyun Kyu Lee, Yong-Liang Ma, and Mannque Rho. Inhomogeneous quark condensate in compressed Skyrme matter. Phys. Rev. D, 91(9):096011, 2015.

- [129] Igor R. Klebanov. Nuclear Matter in the Skyrme Model. Nucl. Phys. B, 262:133–143, 1985.
- [130] Mannque Rho, Sang-Jin Sin, and Ismail Zahed. Dense QCD: A Holographic Dyonic Salt. Phys. Lett. B, 689:23–27, 2010.
- [131] Keun-Young Kim, Sang-Jin Sin, and Ismail Zahed. Dense holographic QCD in the Wigner-Seitz approximation. JHEP, 09:001, 2008.
- [132] H. Forkel, A. D. Jackson, Mannque Rho, C. Weiss, A. Wirzba, and H. Bang. Chiral Symmetry Restoration and the Skyrme Model. Nucl. Phys. A, 504:818–828, 1989.
- [133] Kanabu Nawa, Hideo Suganuma, and Toru Kojo. Brane-induced Skyrmion on S^{*3} : Baryonic matter in holographic QCD. Phys. Rev. D, 79:026005, 2009.
- [134] Michael Buballa and Stefano Carignano. Inhomogeneous chiral condensates. Prog. Part. Nucl. Phys., 81:39–96, 2015.
- [135] D. V. Deryagin, Dmitri Yu. Grigoriev, and V. A. Rubakov. Standing wave ground state in high density, zero temperature QCD at large $N(c)$. Int. J. Mod. Phys. A, 7:659–681, 1992.
- [136] Dominik Nickel. Inhomogeneous phases in the Nambu-Jona-Lasino and quark-meson model. Phys. Rev. D, 80:074025, 2009.
- [137] Stefano Carignano, Dominik Nickel, and Michael Buballa. Influence of vector interaction and Polyakov loop dynamics on inhomogeneous chiral symmetry breaking phases. Phys. Rev. D, 82:054009, 2010.
- [138] Ralf Rapp, Edward V. Shuryak, and Ismail Zahed. A Chiral crystal in cold QCD matter at intermediate densities? Phys. Rev. D, 63:034008, 2001.
- [139] E. Nakano and T. Tatsumi. Chiral symmetry and density wave in quark matter. Phys. Rev. D, 71:114006, 2005.
- [140] Toru Kojo, Yoshimasa Hidaka, Larry McLerran, and Robert D. Pisarski. Quarkyonic Chiral Spirals. Nucl. Phys. A, 843:37–58, 2010.

- [141] Toru Kojo, Robert D. Pisarski, and A. M. Tsvetik. Covering the Fermi Surface with Patches of Quarkyonic Chiral Spirals. Phys. Rev. D, 82:074015, 2010.
- [142] Toru Kojo, Yoshimasa Hidaka, Kenji Fukushima, Larry D. McLerran, and Robert D. Pisarski. Interweaving Chiral Spirals. Nucl. Phys. A, 875:94–138, 2012.
- [143] Robert D. Pisarski, Vladimir V. Skokov, and Alexei M. Tsvetik. Fluctuations in cool quark matter and the phase diagram of Quantum Chromodynamics. Phys. Rev. D, 99(7):074025, 2019.
- [144] Robert D. Pisarski, Alexei M. Tsvetik, and Semeon Valgushev. How transverse thermal fluctuations disorder a condensate of chiral spirals into a quantum spin liquid. Phys. Rev. D, 102(1):016015, 2020.
- [145] Yong-Liang Ma and Mannque Rho. Recent progress on dense nuclear matter in skyrmion approaches. Sci. China Phys. Mech. Astron., 60(3):032001, 2017.
- [146] D. Blaschke, T. Klahn, and D. N. Voskresensky. Diquark condensates and compact star cooling. Astrophys. J., 533:406–412, 2000.
- [147] Hovik Grigorian, David Blaschke, and Dmitri Voskresensky. Cooling of neutron stars with color superconducting quark cores. Phys. Rev. C, 71:045801, 2005.
- [148] Andrew Cumming, Edward F. Brown, Farrukh J. Fattoyev, C. J. Horowitz, Dany Page, and Sanjay Reddy. A lower limit on the heat capacity of the neutron star core. Phys. Rev. C, 95(2):025806, 2017.
- [149] Hua-Xing Chen, V. Dmitrasinovic, and Atsushi Hosaka. Baryon fields with $U(L)(3) \times U(R)(3)$ chiral symmetry II: Axial currents of nucleons and hyperons. Phys. Rev. D, 81:054002, 2010.
- [150] Hua-Xing Chen, V. Dmitrasinovic, and Atsushi Hosaka. Baryon Fields with $U_L(3) \times U_R(3)$ Chiral Symmetry III: Interactions with Chiral $(3, \bar{3}) + (\bar{3}, 3)$ Spinless Mesons. Phys. Rev. D, 83:014015, 2011.

- [151] Hua-Xing Chen, V. Dmitrasinovic, and Atsushi Hosaka. *mathrmBaryons with $U_L(3) \times U_R(3)$ Chiral Symmetry IV: Interactions with Chiral $(8,1) \oplus (1,8)$ Vector and Axial-vector Mesons and Anomalous Magnetic Moments.* Phys. Rev. C, 85:055205, 2012.
- [152] Hiroki Nishihara and Masayasu Harada. Extended Goldberger-Treiman relation in a three-flavor parity doublet model. Phys. Rev. D, 92(5):054022, 2015.
- [153] Anton Motornenko, Jan Steinheimer, Volodymyr Vovchenko, Stefan Schramm, and Horst Stoecker. Equation of state for hot QCD and compact stars from a mean field approach. Phys. Rev. C, 101(3):034904, 2020.
- [154] Toru Kojo, Defu Hou, Jude Okafor, and Hajime Togashi. Phenomenological QCD equations of state for neutron star dynamics: Nuclear-2SC continuity and evolving effective couplings. Phys. Rev. D, 104(6):063036, 2021.
- [155] Kenji Fukushima, Toru Kojo, and Wolfram Weise. Hard-core deconfinement and soft-surface delocalization from nuclear to quark matter. Phys. Rev. D, 102(9):096017, 2020.
- [156] Larry McLerran and Sanjay Reddy. Quarkyonic Matter and Neutron Stars. Phys. Rev. Lett., 122(12):122701, 2019.
- [157] Kie Sang Jeong, Larry McLerran, and Srimoyee Sen. Dynamically generated momentum space shell structure of quarkyonic matter via an excluded volume model. Phys. Rev. C, 101(3):035201, 2020.
- [158] Toru Kojo. Stiffening of matter in quark-hadron continuity. Phys. Rev. D, 104(7):074005, 2021.
- [159] Ingo Tews, Joseph Carlson, Stefano Gandolfi, and Sanjay Reddy. Constraining the speed of sound inside neutron stars with chiral effective field theory interactions and observations. Astrophys. J., 860(2):149, 2018.